



Delft University of Technology

Purifying Radionuclides with Microfluidic Technology for Medical Purpose

Simulating multiphase flows inside a microfluidic channel with the phase field method

Liu, Z.

DOI

[10.4233/uuid:e1bebcdd-185a-4515-b352-76d68f65ace8](https://doi.org/10.4233/uuid:e1bebcdd-185a-4515-b352-76d68f65ace8)

Publication date

2022

Document Version

Final published version

Citation (APA)

Liu, Z. (2022). *Purifying Radionuclides with Microfluidic Technology for Medical Purpose: Simulating multiphase flows inside a microfluidic channel with the phase field method*.
<https://doi.org/10.4233/uuid:e1bebcdd-185a-4515-b352-76d68f65ace8>

Important note

To cite this publication, please use the final published version (if applicable).

Please check the document version above.

Copyright

Other than for strictly personal use, it is not permitted to download, forward or distribute the text or part of it, without the consent of the author(s) and/or copyright holder(s), unless the work is under an open content license such as Creative Commons.

Takedown policy

Please contact us and provide details if you believe this document breaches copyrights.

We will remove access to the work immediately and investigate your claim.

PURIFYING RADIONUCLIDES WITH MICROFLUIDIC TECHNOLOGY FOR MEDICAL PURPOSE

SIMULATING MULTIPHASE FLOWS INSIDE A MICROFLUIDIC CHANNEL WITH THE PHASE FIELD METHOD

Dissertation

for the purpose of obtaining the degree of doctor
at Delft University of Technology
by the authority of the Rector Magnificus Prof. dr. ir. T. H. J. J. van der Hagen,
chair of the Board for Doctorates
to be defended publicly on
Monday 14 March 2022 at 12:30 o'clock

by

Zheng LIU

Master of Science in Particle Physics and Nuclear Physics,
Northeast Normal University, China,
born in Yanji, China.

This dissertation has been approved by

Promotor: Dr. ir. M. Rohde

Promotor: Prof. dr. ir. J. L. Kloosterman

Composition of the doctoral committee:

Rector Magnificus,

chairperson

Dr. ir. M. Rohde,

Delft University of Technology, promotor

Prof. dr. ir. J. L. Kloosterman,

Delft University of Technology, promotor

Independent members:

Prof. dr. T. Ross,

Hannover Medical School

Prof. dr. C. J. M. van Rijn,

University of Amsterdam

Prof. dr. ir. J. R. van Ommen,

Delft University of Technology

Dr. D. C. Visser,

Nuclear Research and Consultancy Group

Dr. ir. V. van Steijn,

Delft University of Technology

Prof. dr. H. TH. Wolterbeek,

Delft University of Technology, reserve member



Delft
University of
Technology



This research was performed in the Reactor Physics and Nuclear Materials (RPNM), Department of Radiation, Science and Technology (RST), Faculty of Applied Sciences (AS), Delft University of Technology (The Netherlands).

This project was financially supported by the China Scholarship Council.

Keywords: Microfluidic solvent extraction, Radionuclide, Phase field method, Multiphase flow, Moving contact line, Apparent contact angle

Printed by: ProefschriftMaken

Copyright © 2022 by Zheng Liu.

An electronic version of this dissertation is available at:

<http://repository.tudelft.nl/>.

CONTENTS

Summary	vii
Samenvatting	xi
1 Introduction	1
1.1 Molybdenum-99 for medical purpose	2
1.1.1 Molybdenum-99 and Technetium-99m for medical imaging	2
1.1.2 Conventional way of producing Molybdenum-99	2
1.1.3 Potential disruption of the Molybdenum-99 supply chain	2
1.1.4 Possible Molybdenum-99 production routes	3
1.2 Producing Molybdenum-99 from a loop system in the Hoger Onderwijs Reactor	3
1.2.1 Setup of the Molybdenum-99 production loop system	3
1.2.2 Hoger Onderwijs Reactor	5
1.2.3 Yields and advantages of the Molybdenum-99 production loop system	5
1.3 Microfluidic liquid-liquid solvent extraction	6
1.3.1 Microfluidic liquid-liquid solvent extraction in general	6
1.3.2 Microfluidic liquid-liquid solvent extraction for radionuclides	8
1.4 Problem description	9
1.5 Research Objectives and Thesis outline	13
1.6 Nomenclature	15
References	16
2 Theory	23
2.1 Basic concepts of microfluidics	24
2.1.1 The continuity equation	24
2.1.2 Navier-Stokes equations for incompressible fluids	24
2.1.3 Multiphase flows in microfluidic channels	25
2.2 The physics of wetting	26
2.2.1 Static wetting	27
2.2.2 Dynamic wetting	28
2.2.3 Contact angle hysteresis	29
2.3 Theory of moving contact line	30
2.3.1 Hydrodynamic theory	31
2.3.2 Molecular-kinetic theory	31

2.4	Numerical modelling of microfluidic multiphase flow	32
2.5	Phase Field Method	33
2.5.1	Phase Field Method and Cahn–Hilliard Equation.	33
2.5.2	Coupling Cahn–Hilliard equation with Navier–Stokes equations.	37
2.5.3	Boundary conditions for the Phase Field Method	39
2.5.4	Dimensionless formulation of the governing equations	41
2.6	COMSOL Multiphysics and Finite Element Method	42
	References	45
3	Influence of the numerical parameters of the Phase Field method on the slug length of dry slug flow inside a microfluidic channel	49
3.1	Introduction	50
3.2	Materials and Methods	51
3.2.1	Microfluidic chip and experimental procedure	51
3.2.2	Fluid properties and measurement of the equilibrium contact angle	52
3.2.3	Slug length of dry slug flow.	54
3.2.4	Governing equations and model description.	54
3.2.5	Mesh dependency study	57
3.3	Results and Discussion	59
3.3.1	Study of the initial interface in the Phase Field method	61
3.3.2	The Pe number versus slug length	64
3.3.3	The Cn number versus slug length	66
3.3.4	Comparing slug length in the simulations with that in the experiments	69
3.4	Conclusions.	70
	References	72
4	Investigating the apparent contact angle of slugs within a double Y-shaped microfluidic channel	75
4.1	Introduction	76
4.2	Materials and Methods	77
4.2.1	Microfluidic chip and experimental procedure	77
4.2.2	Governing equations and boundary conditions	77
4.2.3	Derivation of the equilibrium contact angle and apparent contact angle	78
4.3	Results and Discussion	79
4.3.1	Influence of the Ca number on the apparent contact angles in the simulations	79
4.3.2	Influence of the Ca_f number on the apparent contact angles	83
4.3.3	Influence of the value of the equilibrium contact angle on the apparent contact angles	84
4.3.4	Influence of the Pe number and the Cn number on the apparent contact angles	86
4.3.5	Comparing simulation results of the apparent contact angle with the experimental results	88

4.3.6	Influence of the numerical parameters on the velocity of the slugs.	89
4.4	Conclusions.	92
	References	94
5	Investigating flow patterns inside a double Y-shaped microfluidic channel with Phase Field method	95
5.1	Introduction	96
5.2	Materials and Methods	97
5.2.1	Measurement of physical property of fluids	98
5.2.2	Experimental procedure	101
5.2.3	Model description and simulation setup	101
5.3	Results and Discussion	102
5.3.1	Influence of the mobility parameter and capillary width on flow patterns	103
5.3.2	Flow pattern versus the Ca number	108
5.3.3	Flow pattern versus the We number	111
5.3.4	Equilibrium contact angle versus flow patterns	113
5.4	Conclusions.	116
	References	117
6	Leakage at the outlet of the double Y-shaped microfluidic channel	121
6.1	Introduction	122
6.2	Materials and Methods	123
6.3	Results and Discussion	124
6.3.1	Leakage direction at the outlet of the microfluidic channel in the experiments	124
6.3.2	Leakage phenomenon by changing the equilibrium angle	126
6.3.3	Leakage phenomena by using the non-equilibrium contact angle boundary condition	129
6.3.4	Influence of the mobility parameter on the leakage	131
6.4	Conclusions.	133
	References	134
7	Conclusions and recommendations	137
7.1	Conclusions.	138
7.2	Practice guidelines	141
7.3	Recommendations	143
	References	144
	Acknowledgements	147
	Curriculum Vitæ	149
	List of Publications	151

SUMMARY

Molybdenum-99 (^{99}Mo) is important in the medical field because its daughter nuclide Technetium-99m ($^{99\text{m}}\text{Tc}$) is the most widely used radionuclide for medical imaging. Nearly 95 % of the worldwide ^{99}Mo demand is produced in only a few nuclear reactors, amongst which the largest one is situated in Petten, the Netherlands. To this purpose, solid targets containing ^{235}U are irradiated for around one week and unloaded for further processing. At the Delft University of Technology, it has been proposed to produce ^{99}Mo by irradiating a uranyl salt solution with neutrons in a continuous loop system at the Hoger Onderwijs Reactor. A weekly production of 289 6-day Ci can be achieved, which is about 3 % of the global ^{99}Mo demand. One major advantage of this production method is that the solution target supports online extraction. Compared with the conventional way of producing ^{99}Mo by irradiating solid uranium targets, online extraction can separate the produced ^{99}Mo faster from the production loop, thereby reducing the decay loss of ^{99}Mo .

This research focuses on utilizing the parallel multiphase flow microfluidic liquid-liquid solvent extraction inside a double Y-shaped microfluidic channel to extract ^{99}Mo from the production loop. In the parallel flow pattern, two immiscible solutions flow parallelly inside the channel while ^{99}Mo is selectively extracted from the aqueous solution to an organic solution. The small-dimension of the microfluidic device reduces the diffusion distance for the solutes and increases the surface-to-volume ratio, both of which improve the mass transport of ^{99}Mo and thus enhance the extraction efficiency. If such an approach proves feasible, then a bundle of such microfluidic channels can be parallelized, to scale up the extraction capacity. Furthermore, it is also possible to extend the method to other radionuclides which are produced based on solution targets. However, two practical problems arise in this extraction process. Firstly, there are no clear criteria about how to obtain the desired parallel flow pattern. Secondly, even in the case of parallel flow, complete phase separation is hard to achieve, because there is often a leakage from one phase to the other at the outlet of the microfluidic channel. The latter problem leads to contamination of the extracted ^{99}Mo , which conflicts with the strict requirements of radiopharmaceutical purity.

The flow pattern changing from parallel flow to other flow patterns attributes to topological changes of the interface, which is termed the *Interface Breakup Problem* in this thesis. Furthermore, the leakage at the outlet of the microfluidic channel is related to the *Moving Contact Line Problem*, *i.e.*, the movement of the interface between two immiscible fluids on a solid surface. This thesis explores the feasibility of utilizing the Phase Field method to model these phenomena inside a double Y-shaped microfluidic channel. If the Phase Field method is able to describe the *Interface Breakup Problem* and the *Moving Contact Line Problem* under one framework, then the Phase Field method

can be used as a numerical tool to provide guidelines for avoiding the above-mentioned practical problems in redesigning the microfluidic channel and controlling flow conditions. The Phase Field method introduces a diffusive interface with a finite thickness, within which the physical properties of the immiscible fluids (like density and viscosity) change smoothly and continuously. For the *Moving Contact Line Problem*, it attempts to integrate the hydrodynamic description and the molecular-kinetic description in one framework by including a diffusive transport of the order parameter (ϕ , the variable that distinguishes different physical properties of the immiscible fluids) within the interface to remove the mathematical singularity at the wall. In this approach, the capillary width (ϵ , a numerical parameter) determines the thickness of the diffusive interface and the mobility parameter (M , a numerical parameter) determines the diffusive transport of the order parameter (ϕ). The main advantage for choosing the Phase Field method occurs when dealing with the *Moving Contact Line Problem*, the diffusive driven mechanism within the interface is compatible with the no-slip boundary condition at the solid wall and no special treatment is required.

To make the calculation affordable, the thickness of the diffusive interface as used in the Phase Field method is much larger than the one of the real physical interface. In the *Interface Breakup Problem*, the simulation results vary with the capillary width (ϵ) and the mobility parameter (M). To ensure the Phase Field method simulates the same physical problem when the capillary width (ϵ) is changed, the mobility parameter (M) should be changed accordingly, to generate consistent simulation results. However, the relationship between ϵ and M is still unclear. This study investigates their relationship by monitoring the slug length of dry slug flow in a double Y-shaped microfluidic channel. It is found that the slug length calculated with the Phase Field method is linearly proportional to the Pe^{-1} number and the Cn number when the Ca number of the two phases is smaller than 1×10^{-3} . The dimensionless slug length (L_{slug}) can be described by the empirical correlation: $L_{slug} = 0.72CnPe^{-1} + 3.86$. In other words, to generate a consistent and physical slug length in the microfluidic channel, the numerical parameters ϵ and M need to be adjusted by following $CnPe^{-1} = \text{constant}$ when $Ca < 1 \times 10^{-3}$.

Concerning simulating leakage at the outlet of the microfluidic channel with an equilibrium contact angle boundary condition ($\mu_f = 0 \text{ Pa} \cdot \text{s}$ in Equation 2.39, which is often applied in the Phase Field method), leakage does not occur like in experiments. One of the reasons is that imposing the equilibrium contact angle boundary condition does not sufficiently capture the physics of the *Moving Contact Line* at the outlet. Considering this, a non-equilibrium contact angle boundary condition ($\mu_f > 0 \text{ Pa} \cdot \text{s}$ in Equation 2.39), which has been reported to generate more physical results in capturing the droplet spreading process in the Phase Field simulation, has been adopted. Nevertheless, not all mechanisms of this boundary condition are fully understood and it is not known if it is universally applicable, especially for multiphase flows in microfluidics. This study concentrates on simulating dry slug flow with the non-equilibrium contact angle boundary condition. Due to the *Moving Contact Line*, the apparent contact angles (θ_{app}) of the slugs deviate from the equilibrium contact angle (θ_e). By imposing the equilibrium contact angle boundary condition in dry slug flow of the n-heptane/water system, the ap-

parent contact angle (θ_{app}) is always equal to the equilibrium contact angle (θ_e), which indicates that there is no effect of the *Moving Contact Line* on the apparent contact angle (θ_{app}). With application of the non-equilibrium contact angle boundary condition ($\mu_f > 0 \text{ Pa} \cdot \text{s}$), the advancing contact angle (θ_A) is larger than the equilibrium contact angle (θ_e) and the receding contact angle (θ_R) is smaller than the equilibrium contact angle (θ_e), which agrees with the experimental observations. The apparent contact angles (θ_{app}) of the slug are determined by the Caf number ($Caf = \frac{\mu_f \bar{U}_{org}}{\sigma}$) of the system. To produce the same apparent contact angle (θ_{app}), the three variables (U_{org} , σ and μ_f) can be varied as long as the Caf number is kept the same. With the contact line friction parameter (μ_f) in the range between 1.0 and 2.0 $\text{Pa} \cdot \text{s}$, the apparent contact angles (θ_{app}) of the slug in the simulations reasonably agree with those in the experiments.

Currently, there are no clear criteria that are available for accurately predicting flow patterns in microfluidic channels. One of the reasons for the difficulty is that the understanding of multiphase flows in microfluidics is incomplete and there are lots of influencing factors to be taken into account, including the geometry and fabrication material of the microfluidic channel, physical properties of the working fluids as well as operating conditions. To utilize the parallel multiphase flow microfluidic liquid-liquid solvent extraction, with the help of the Phase Field method and the experiments, this study aims to provide guidelines for obtaining the parallel flow pattern in the studied double Y-shaped microfluidic channel. This research starts with investigating the influence of the mobility parameter (M) and capillary width (ϵ) of the Phase Field method on predicting the parallel flow pattern. In modelling the occurrence of parallel flow, it finds that increasing the value of the mobility parameter (M) and the capillary width (ϵ) shift the critical Re number (the first time that the parallel flow occurs by increasing volumetric flow rates) to a higher value. In this case, the Phase Field method can be utilized for predicting flow patterns by finding the specific combination of the mobility parameter (M) and the capillary width (ϵ), under which condition the simulation results agree with the experimental results. Secondly, combining the Phase Field method with experiments based on the toluene/water system and the n-heptane/water system, this study reveals the dominating force that determines the flow pattern inside the microfluidic chip in this study. When the interface is located in the centre of the microfluidic channel, the parallel flow pattern can be maintained when the Ca number of both phases is larger than 1×10^{-3} . By studying all the three variables in the Ca number, the Phase Field simulation confirms that the Ca number that determines the occurrence of parallel flow. Further research also shows that the We number plays a minor role in determining the occurrence of the parallel flow pattern in the studied microfluidic system. Thirdly, the interaction between the fluids and the microfluidic channel wall influences the occurrence of parallel flow. Based on the experimental results and the Phase Field simulation of the toluene/water system and the tol+Aliquat/water system, when one of the phases dominantly wets the wall surface (*i.e.*, θ_e is close to 0° or 180°), the parallel flow pattern can occur at a lower value of the Ca number.

When a parallel flow pattern is established, complete phase separation is hard to achieve and there is often a leakage from one phase to the other at the outlet of the double Y-

shaped microfluidic channel, which results in failure of the microfluidic solvent extraction. In this research, the leakage phenomenon is investigated with experiments and the Phase Field method, aiming to provide guidelines for achieving complete phase separation. Firstly, the volumetric flow rate ratio (Φ_{aq}/Φ_{org}) of the fluids influences the position of the interface inside the microfluidic channel, determining the leakage direction. Moreover, the leakage is unavoidable, even though the interface is located in the centre of the main channel. Under such circumstances, the fluid that preferably wets the microfluidic channel wall leaks to the other outlet. In the Phase Field simulation, applying the equilibrium contact angle boundary condition, only when one of the phases dominantly wets the microfluidic channel (θ_e is close to 0° or 180°), the leakage phenomenon occurs. In this case, leakage in the simulations does not agree with that in the experiments. With the non-equilibrium contact angle boundary condition, simulation shows clogging organic slugs, which is considered as unphysical. Further research reveals that decreasing the value of the mobility parameter (M) results in leakage; however, since the mobility parameter (M) determines flow patterns, it is not possible to use the same value of M to predict the occurrence of parallel flow and leakage at the same time.

SAMENVATTING

Molybdeen-99 (^{99}Mo) is één van de belangrijkste medische isotopen omdat de dochter-nuclide, Technetium-99m ($^{99\text{m}}\text{Tc}$), de meest gebruikte radionuclide is voor medische beeldvorming. Bijna 95 % van de wereldwijde vraag naar ^{99}Mo wordt geleverd door slechts een paar kernreactoren, waarvan de grootste zich in Petten in Nederland bevindt. In deze reactoren worden vaste targets die ^{235}U bevatten, gedurende ongeveer een week bestraald en vervolgens ontladen voor verdere verwerking. Aan de Technische Universiteit Delft is het idee ontstaan om ^{99}Mo te produceren door een oplossing van een uranylzout met neutronen te bestralen in een continu werkend loop-systeem. Op deze manier kan een wekelijkse productie van 289 6-daagse Ci worden bereikt, wat ongeveer 3 % van de wereldwijde vraag naar ^{99}Mo is. Een groot voordeel van deze productiemethode is dat het gebruik van een vloeibare target in de vorm van een oplossing van een uranylzout online extractie ondersteunt. Vergelijken met de conventionele manier om ^{99}Mo , kan online extractie de geproduceerde ^{99}Mo sneller scheiden uit het loopsysteem, waardoor het vervalverlies van ^{99}Mo wordt verminderd.

Dit onderzoek richt zich op het gebruik van een parallelle, microfluïdische vloeistof-vloeistof extractie in een dubbel Y-vormig microfluïdisch kanaal om ^{99}Mo te extraheren uit het hierboven genoemde loop-systeem. In het kanaal stromen twee niet-mengbare oplossingen parallel naast elkaar terwijl ^{99}Mo selectief wordt geëxtraheerd uit de waterige oplossing naar een organische oplossing. De kleinschaligheid van zo'n kanaal vermindert de diffusieafstand voor de opgeloste stoffen en verhoogt de oppervlakte-volumeverhouding, die beide het massatransport van ^{99}Mo verbeteren en zo de extractie-efficiëntie verhogen. Als een dergelijke aanpak haalbaar blijkt, kan een bundel van dergelijke microfluïdische kanalen worden geparallelliseerd om de extractiecapaciteit op te voeren. Bovendien is het ook mogelijk een dergelijke online extractiemethode uit te breiden tot andere radionucliden die worden geproduceerd.

Bij dit extractieproces doen zich echter twee praktische problemen voor. Ten eerste zijn er geen duidelijke criteria voor het verkrijgen het gewenste parallelle stromingspatroon. Ten tweede is zelfs bij parallelle stroming een volledige fasescheiding niet of nauwelijks haalbaar en vindt er daarom vaak lekkage plaats van de ene fase naar de andere bij de uitgang van het microfluïdisch kanaal. Dit laatste probleem leidt tot vervuiling van het geëxtraheerde ^{99}Mo , hetgeen in strijd is met de strikte eisen die aan radiofarmaceutische zuiverheid worden gesteld.

Het stromingspatroon, dat kan veranderen van parallelle stroming naar andere stromingspatronen, kan worden toegeschreven aan topologische veranderingen van het grensvlak tussen beide fasen, wat in dit proefschrift wordt aangeduid als het zogenaamde *Interface Breakup Problem*. Verder is de lekkage bij de uitgang van het microfluïdische

kanaal gerelateerd aan het zogenaamde *Moving Contact Line Problem*, i.e., de beweging van het grensvlak tussen twee niet-mengbare vloeistoffen op een vast oppervlak. Dit proefschrift gaat over de haalbaarheid van het gebruik van de Phase Field Method om beide fenomenen in een dubbel Y-vormig microfluïdisch kanaal te kunnen modelleren. Als de Phase Field Method in staat is om het *Interface Breakup Problem* en het *Moving Contact Line Problem* te beschrijven, dan kan de Phase Field Method gebruikt worden als een numeriek instrument om richtlijnen te geven voor het vermijden van de hierboven genoemde praktische problemen bij het ontwerpen van het microfluïdisch kanaal en bij het instellen van de juiste stromingscondities. De Phase Field Method introduceert een diffusus grensvlak met een eindige dikte, waarbinnen de fysieke eigenschappen van de niet-mengbare vloeistoffen (zoals dichtheid en viscositeit) soepel en continu veranderen. Voor het *Moving Contact Line Problem* probeert het de hydrodynamische beschrijving en de moleculair-kinetische beschrijving in één raamwerk te integreren door een diffusus transport van de ordeparameter (ϕ , de variabele die verschillende fysieke eigenschappen van de niet-mengbare vloeistoffen) binnen de interface om de wiskundige singulariteit aan de muur te verwijderen. In deze benadering bepaalt de capillaire breedte (ϵ , een numerieke parameter) de dikte van de diffusieve interface en de mobiliteitsparameter (M , een numerieke parameter) bepaalt het diffuse transport van de orderparameter (ϕ). De belangrijkste reden dat gekozen wordt voor Phase Field Method is dat bij het beschrijven van de *Moving Contact Line* het diffusieve mechanisme binnen de interface compatibel is met de no-slip randvoorwaarde aan de wand.

Om de berekening qua rekentijd binnen de perken te houden, is de dikte van het diffusieve grensvlak in de Phase Field Method veel groter dan de dikte van het fysische grensvlak. In het *Interface Breakup Problem* variëren de simulatieresultaten als functie van de capillaire breedte (ϵ) en de mobiliteitsparameter (M). Om er zeker van te zijn dat de Phase Field Method nog steeds hetzelfde fysische probleem simuleert bij een wijziging in de capillaire breedte (ϵ), moet de mobiliteitsparameter (M) dienovereenkomstig worden gewijzigd. Een dergelijke relatie tussen ϵ en M is echter nog steeds niet bekend. Deze studie onderzoekt deze relatie door het monitoren van de slug-lengte in een dubbel Y-vormig microfluïdisch kanaal. Er wordt vastgesteld dat de slug-lengte lineair evenredig is met het Pe^{-1} getal en het Cn getal, op voorwaarde dat het Ca getal van beide fasen kleiner is dan 1×10^{-3} . De dimensieloze slug-lengte (L_{slug}) kan dan worden beschreven door de in dit onderzoek gevonden empirische correlatie $L_{slug} = 0.72CnPe^{-1} + 3.86$. Met andere woorden, om een consistente en fysische slug-lengte in het microfluïdisch kanaal te genereren, moeten de numerieke parameters $CnPe^{-1} = \text{constant}$ gehouden worden voor $Ca < 1 \times 10^{-3}$.

Als de evenwichtscontacthoek-randvoorwaarde wordt gebruikt in de Phase Field simulaties ($\mu_f = 0 \text{ Pa} \cdot \text{s}$, die vaak wordt toegepast), komt lekkage minder vaak voor dan in experimenten gevonden wordt. Eén van de redenen zou kunnen zijn dat het opleggen van deze evenwichtscontacthoek-randvoorwaarde de fysica van de *Moving Contact Line* bij de uitlaat niet nauwkeurig kan weergeven. Om die reden wordt in dit onderzoek ook een niet-evenwichts contacthoek randvoorwaarde ($\mu_f > 0 \text{ Pa} \cdot \text{s}$) gebruikt, waarvan bekend is dat het meer fysische resultaten genereert bij het berekenen van druppelverspreidings-

processen. Het is niet bekend of deze randvoorwaarde universeel toepasbaar is, en dus ook gebruikt kan worden voor meerfase-stroming in microkanalen. Deze studie concentreert zich daarom eerst op het simuleren van slug-stroming in een n-heptaan/water systeem, waarbij de niet-evenwichts contacthoek randvoorwaarde wordt gebruikt. Ten gevolge van de *Moving Contact Line* zullen de schijnbare contacthoeken (θ_{app}) aan de voor- en achterkant van de slugs afwijken van de evenwichtscontacthoek (θ_e). Door het opleggen van de niet-evenwichts contacthoek randvoorwaarde ($\mu_f > 0 \text{ Pa} \cdot \text{s}$), is inderdaad gevonden dat de advancing contacthoek (θ_A) groter is dan de evenwichtscontacthoek (θ_e), en dat de receding contacthoek (θ_R) kleiner is dan de evenwichtscontacthoek (θ_e). Deze resultaten komen overeen met experimentele waarnemingen. Bovendien is gevonden dat als de contactlijn-wrijvingsparameter (μ_f) valt binnen het bereik van 1.0 tot 2.0 $\text{Pa} \cdot \text{s}$, de schijnbare contacthoeken (θ_{app}) van de slugs in de simulaties redelijk goed overeen komen met die in de experimenten. Ook is gevonden dat de schijnbare contacthoeken (θ_{app}) van de slug worden bepaald door een zogenaamd Caf getal van het systeem. Om dezelfde schijnbare contacthoek (θ_{app}) te verkrijgen, kunnen de drie variabelen (U_{org} , σ en μ_f) worden gevarieerd, zolang het Caf getal maar gelijk wordt gehouden.

Momenteel zijn er geen duidelijke criteria beschikbaar voor het nauwkeurig voorspellen van stromingspatronen in microfluïdische kanalen. Eén van de redenen voor dit probleem is dat het begrip van de meerfasenstroming in microfluïdica onvolledig is en dat er veel factoren zijn waarmee rekening moet worden gehouden, waaronder de geometrie en het fabricagemateriaal van het microfluïdisch kanaal, de fysische eigenschappen van de werkende vloeistoffen en procescondities zoals volumedebieten. Deze studie beoogt daarom richtlijnen te geven voor het verkrijgen van een parallel stromingspatroon in het dubbele Y-vormige microfluïdische kanaal. Dit onderzoek begint met het onderzoeken van de invloed van de mobiliteitsparameter (M) en de capillaire breedte (ϵ) op het voorspellen van het parallelle stromingspatroon. Bij het modelleren van het optreden van de parallelle stroming wordt gevonden dat het verhogen van de waarde van de mobiliteitsparameter (M) en de capillaire breedte (ϵ) het kritieke Re getal (punt waarbij parallelle stroming optreedt bij toenemende volumedebieten) naar een hogere waarde verschuift. In dit geval kan de Phase Field Method worden gebruikt voor het voorspellen van stromingspatronen door de juiste, specifieke combinatie te vinden van de mobiliteitsparameter (M) en de capillaire breedte (ϵ), onder welke voorwaarde de simulatiresultaten overeenstemmen met de experimentele resultaten. Ten tweede, door het vergelijken van de Phase Field Method simulaties met experimenten gebaseerd op een tolueen/water systeem en een n-heptaan/water systeem, kan het dominante mechanisme worden gevonden dat het stromingspatroon in de microfluïdische chip bepaalt. Wanneer het grensvlak zich in het midden van het microfluïdische kanaal bevindt, kan het parallelle stromingspatroon worden gehandhaafd wanneer het Ca getal van beide fasen groter is dan 1×10^{-3} . Door variatie van alle drie de variabelen in het Ca getal te bestuderen, wordt bevestigd dat het Ca getal inderdaad het optreden van parallelle stroming bepaalt. Verder onderzoek toont aan dat het We getal een ondergeschikte rol speelt in het optreden van het parallelle stromingspatroon. Ten derde beïnvloedt de interactie tussen de vloeistoffen en de microfluïdische kanaalwand het optreden van de parallelle

stroming. Op basis van de experimentele resultaten en de Phase Field simulaties van een tolueen/water systeem en een een tol+Aliquat/water systeem kan een parallel stromingspatroon optreden bij een lagere waarde van het Ca getal, wanneer een van de fasen het wandoppervlak in extreme mate bevochtigt (dus θ_e ligt dicht bij 0° of 180°).

Wanneer een parallel stromingspatroon tot stand is gebracht, is volledige fasescheiding zeer moeilijk te bereiken en treedt vaak lekkage op van de ene fase naar de andere bij de uitgang van het dubbele Y-vormige microfluïdische kanaal. In dit onderzoek wordt daarom de lekkage onderzocht met behulp van experimenten en de Phase Field Method met als doel richtlijnen te geven voor het bereiken van volledige fasescheiding. Ten eerste beïnvloedt de verhouding van volumedebieten (Φ_{aq}/Φ_{org}) van de vloeistoffen de positie van de interface binnen het microfluïdische kanaal, waardoor de lekrichting wordt bepaald. Bovendien is gevonden dat lekkage onvermijdelijk is, ook al bevindt de interface zich in het midden van het hoofdkanaal. Onder dergelijke omstandigheden zal de vloeistof die bij voorkeur de wand van het microfluïdisch kanaal bevochtigt, naar de andere uitgang lekken. In de Phase Field Method, waarbij de evenwichtscontacthoekrandvoorwaarde wordt toegepast, treedt het lekverschijnsel alleen op wanneer één van de fasen het microfluïdische kanaal in extreme mate bevochtigt (θ_e ligt dicht bij 0° of 180°). In dit geval komt lekkage in de simulaties niet overeen met die in de experimenten. Met de niet-evenwichts contacthoek-randvoorwaarde laat de simulatie verstopping zien in de uitstroom van de organische vloeistof, wat niet-fysisch gedrag is. Verder onderzoek toont aan dat het verlagen van de waarde van de mobiliteitsparameter (M) resultert in lekkage; aangezien de mobiliteitsparameter (M) echter de stromingspatronen bepaalt, is het niet mogelijk om dezelfde waarde van M te gebruiken om tegelijkertijd het optreden van parallelle stroming en lekkage te kunnen voorspellen.

1

INTRODUCTION

1.1. MOLYBDENUM-99 FOR MEDICAL PURPOSE

1.1.1. MOLYBDENUM-99 AND TECHNETIUM-99M FOR MEDICAL IMAGING

Molybdenum-99 (^{99}Mo) is important in the medical field because its daughter nuclide Technetium-99m (^{99m}Tc) is the most widely used radionuclide for medical imaging [1]. Each year, there are about 30 to 40 million diagnostic procedures using ^{99m}Tc . The ^{99m}Tc is eluted from a $^{99}\text{Mo}/^{99m}\text{Tc}$ generator for further use in medical imaging.

^{99m}Tc has a half-life of 6.01 hours and emits photons with energy of 140 keV, which can be effectively detected by scintillation detectors. A variety of ligands are able to be labelled by ^{99m}Tc , incorporating into radiopharmaceuticals. Based on the different properties of the ligands, the radiopharmaceuticals can concentrate in the specific organs of the human body. Diseases can be found by detecting the photons emitted from the radiopharmaceuticals [2] [3].

1.1.2. CONVENTIONAL WAY OF PRODUCING MOLYBDENUM-99

Nearly 95 % of the worldwide ^{99}Mo demand is supplied by only a few nuclear reactors: HFR in the Netherlands, BR-2 in Belgium, SAFARI-1 in South Africa, LVR-15 in Czech Republic, Maria in Poland, and OPAL in Australia [4]. All of the above mentioned nuclear reactors produce ^{99}Mo by irradiating enriched uranium solid targets with neutrons.

Usually, the solid targets are uranium plates contained in aluminium clad [3]. Under neutron irradiation, the fission reaction of uranium-235 (^{235}U) in the solid targets leads to the production of ^{99}Mo and other fission products. The calculated fission yield of ^{99}Mo is about 6 % [1].

Typically, the irradiation time for the enriched uranium solid targets is about one week. After irradiation, the solid targets are removed from the nuclear reactor core, cooled down and transported to processing facilities. In the processing facilities, ^{99}Mo is separated and recovered [3].

1.1.3. POTENTIAL DISRUPTION OF THE MOLYBDENUM-99 SUPPLY CHAIN

After recovery by processing facilities, ^{99}Mo is put into $^{99}\text{Mo}/^{99m}\text{Tc}$ generators and distributed to hospitals all around the world. Due to the 66-hour half-life of ^{99}Mo , long time stockpile is impossible. Under such circumstances, there is a ^{99}Mo global supply chain which provides ^{99}Mo continuously [5][6].

Concerning the fact that there are only several nuclear reactors and processing facilities in the global ^{99}Mo supply chain, any interruption of these nuclear reactors and processing facilities will bring substantial pressure in the supply chain. Considering the age of

the ^{99}Mo production reactors¹, temporary shutdown for maintenance may occur more often.

Actually, the global ^{99}Mo supply chain is rather fragile. For example, it was under serious stress in November 2017 because of the unplanned outage of NTP processing facility in South Africa [7]. Considering the global demand for ^{99}Mo will increase in the future [8], alternative ^{99}Mo producing methods should be developed and added into the supply chain.

1.1.4. POSSIBLE MOLYBDENUM-99 PRODUCTION ROUTES

Based on the irradiation methods, the possible routes to produce ^{99}Mo can be categorized as: gamma-ray route (e.g., $^{100}\text{Mo}(\gamma, n)^{99}\text{Mo}$ [9] [10] and $^{235,238}\text{U}(\gamma, F)^{99}\text{Mo}$), neutron route (e.g., $^{235,238}\text{U}(n, F)^{99}\text{Mo}$ [11], $^{100}\text{Mo}(n, 2n)^{99}\text{Mo}$ [12] and $^{98}\text{Mo}(n, \gamma)^{99}\text{Mo}$ [13]) as well as accelerated charged-particle route (e.g., $^{96}\text{Zr}(\alpha, n)^{99}\text{Mo}$ [14] and $^{100}\text{Mo}(p, x)^{99}\text{Mo}$ [15]). Based on the yield and specific activity of ^{99}Mo , Wolterbeek *et al.* have reviewed all upsides and downsides of these routes [1].

The majority of these above-mentioned routes produce ^{99}Mo by irradiating solid targets². The solid targets need to be irradiated for several hours to a few days before the produced ^{99}Mo can be separated from the irradiated targets. Considering ^{99}Mo undergoes natural decay, it is important to separate it from the irradiated targets as fast as possible. Based on this idea, we have proposed a different approach, *i.e.*, producing ^{99}Mo by irradiating a solution target with neutrons. One major advantage of this method is that the solution target supports online extraction, which has the advantage of separating the produced ^{99}Mo faster from the production facility, to reduce the decay loss of ^{99}Mo . Section 1.2 introduces the newly proposed production method and the corresponding extraction method. The solution target can be chosen from the above-mentioned neutron producing route. This thesis focuses on the case when a uranyl salt solution is chosen as the irradiated target in the loop and Section 1.2.3 introduces its yield and advantages.

1.2. PRODUCING MOLYBDENUM-99 FROM A LOOP SYSTEM IN THE HOGER ONDERWIJS REACTOR

1.2.1. SETUP OF THE MOLYBDENUM-99 PRODUCTION LOOP SYSTEM

According to the conceptual design, the uranyl salt solution to be irradiated flows inside a loop. Figure 1.1 demonstrates the geometry setup of the ^{99}Mo production loop system and Figure 1.2 shows the cross section of the loop system. The loop is U-shaped and placed in an already existence beam-tube in the Hoger Onderwijs Reactor. The beam-

¹Except for the OPAL reactor in Australia, all of the above mentioned nuclear reactors were built between the 1950s and the 1970s.

²One exception is producing ^{99}Mo from aqueous homogeneous reactors. In this method, ^{235}U serves as the fuel of the reactor as well as the target being irradiated at the same time [16].

tube and the Hoger Onderwijs Reactor will be described in Section 1.2.2. The uranyl salt solution flows inside the U-shaped loop and be irradiated by neutrons generated from the reactor core. In both Figure 1.1 and Figure 1.2, the U-shaped loop is indicated in yellow and the beam-tube is in black. Between the U-shaped loop and the beam-tube, there is an additional tube which is indicated in red. The additional tube serves as the flood barrier in case of a leakage of the uranyl salt solution.

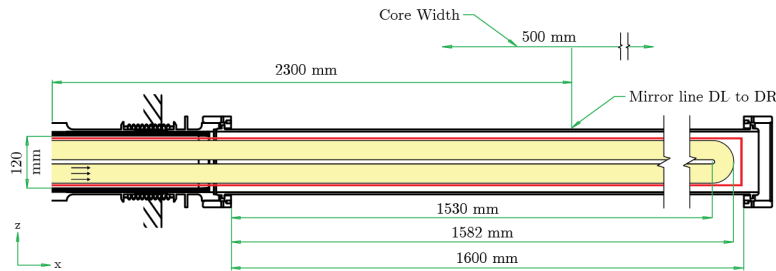


Figure 1.1: Geometry setup of the Molybdenum-99 production loop system. Figure from Bachelor Thesis of *Huisman* [17].

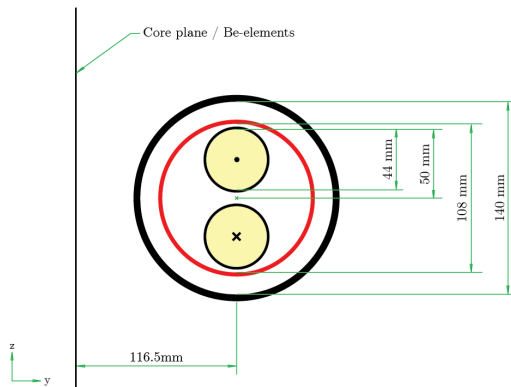


Figure 1.2: Cross section of the Molybdenum-99 production loop system. Figure from Bachelor Thesis of *Huisman* [17].

1.2.2. HOGER ONDERWIJS REACTOR

In the conceptual design of the Molybdenum-99 production loop system, the Hoger Onderwijs Reactor (HOR) functions as the source of neutrons. The HOR is an open pool-type research reactor operated by Reactor Institute Delft. Figure 1.3 shows the top view of the HOR. The water pool is indicated in blue, inside which the core is indicated in brown. There are four beam-tubes in the HOR and the beam-tube which contains the U-shaped loop is highlighted with red.

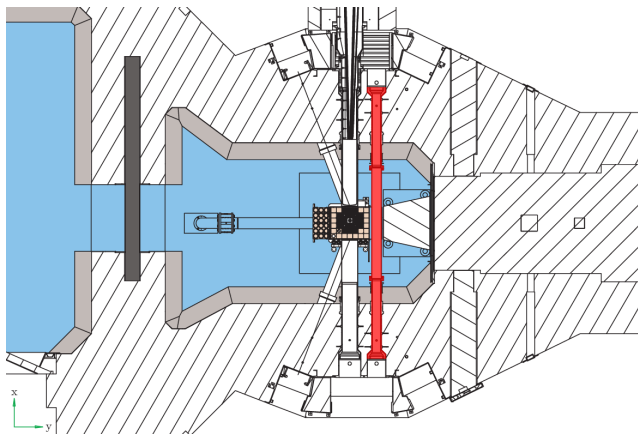


Figure 1.3: Schematic top view of the Hoger Onderwijs Reactor (HOR). Figure from Bachelor Thesis of *Huisman* [17].

1.2.3. YIELDS AND ADVANTAGES OF THE MOLYBDENUM-99 PRODUCTION LOOP SYSTEM

Currently, the global ^{99}Mo demand is about 10000 6-day Curie (Ci)³ per week [7]. In the Molybdenum-99 production loop, the uranyl salt solution has a uranium concentration of 310 g L^{-1} and ^{235}U enrichment of 19.75 %. Under such circumstances, a weekly ^{99}Mo production of 289 6-day Ci can be achieved, which is about 3 % of the global ^{99}Mo demand [18].

Besides the above-mentioned advantage that the online extraction method can reduce the activity loss of ^{99}Mo from its natural decay, the ^{235}U can be used more effectively in our conceptual design, compared with the conventional way of producing ^{99}Mo by irradiating solid ^{235}U targets. In the conventional way of irradiating solid targets, only about 3 % of the ^{235}U is consumed. After irradiation, the remaining ^{235}U is treated as waste [3]. In the ^{99}Mo production loop, the loop can run for 22 years without refilling the uranyl

³6-day Curie is the measurement of the remaining activity of ^{99}Mo six days after it leaves the processing facility.
1 Ci = 3.7×10^{10} Bq

salt solution [19]. The long-term running time ensures that ^{235}U can be consumed more effectively.

1.3. MICROFLUIDIC LIQUID-LIQUID SOLVENT EXTRACTION

Based on the idea of online extracting ^{99}Mo from the loop system, the feasibility of exploiting microfluidic liquid-liquid solvent extraction is investigated as the main topic of this thesis. This section briefly introduces and reviews microfluidic liquid-liquid solvent extraction, especially for radionuclides. Besides, this section also describes the problems that arise in utilizing the microfluidic liquid-liquid solvent extraction to purify ^{99}Mo .

1.3.1. MICROFLUIDIC LIQUID-LIQUID SOLVENT EXTRACTION IN GENERAL

Microfluidics is the science and technology of manipulating fluids at the micro-scale. It has been widely used in various fields, including colloid science, clinical chemistry, biological engineering, environmental detection and so forth. The core of the microfluidic device is the microfluidic channel which has a typical width of a few hundred micrometer. In addition, microfluidic devices usually integrate microfluidic channels with pumps, valves and detectors. Such a system is called "Micro-total-analysis-system" (μ TAS) or "Lab-on-a-Chip" (LOC) [20] [21].

Liquid-liquid solvent extraction is the technique of separating solutes by their different solubilities in immiscible fluids (usually an aqueous phase and an organic phase), for the purpose of purification. In the case of extracting metal ions from the aqueous phase to the organic phase, the extraction process depends on the reaction mechanism at the interface as well as chemical conditions of both phases. For example, in the case of selectively extracting molybdenum(VI) from a strong acid leach ore solution, *Zeng et al.* reported that the concentration of the extractant (HBL101, a commercial oxime extractant), pH value of the aqueous phase and the temperature all determined the final extraction efficiency [22].

When combining the liquid-liquid solvent extraction with microfluidics, the small-scale feature of the microfluidic device would reduce the diffusion distance for the solutes and increase the surface-to-volume ratio, both of which can improve the mass transport performance of the solutes and thus enhance the extraction efficiency [23]. When exploiting the microfluidic device for liquid-liquid solvent extraction, in general, there are two flow patterns: parallel flow and segmented flow. As demonstrated in Figure 1.4a, in the parallel flow pattern, the immiscible two phases are flowing continuously side-by-side⁴. As for the direction of flows, the immiscible two phases can flow either in the same direction (co-current flow) or in the opposite directions (counter-current flow). Theoretically,

⁴There is one flow pattern called annular flow, which is similar to parallel flow. In the annular flow pattern, one phase is present in the axis centre of the microfluidic channel, being separated from the microfluidic channel wall by the other immiscible phase, forming an annulus at the cross-section of the microfluidic channel. However, the annular flow pattern does not support automatic phase separation at the outlets of the microfluidic channel. Thus, it is beyond the scope of this thesis.

compared with the co-current flow, the counter-current flow is able to provide better mass transfer efficiency [24]. However, the formation of counter-current flow needs the help of the selective surface modification of the microfluidic channel [25] [26] [27]. The selective surface modification method is not adaptable with the irradiation working environment. Thus, this thesis only focuses on the co-current parallel flow.

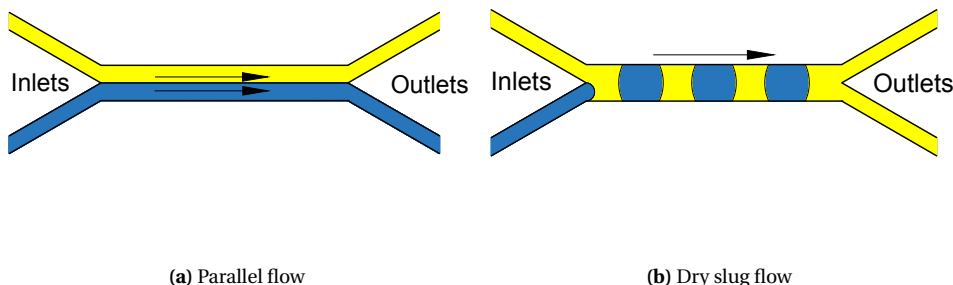


Figure 1.4: Schematic diagram of flow patterns inside a double Y-shaped microfluidic channel. Yellow indicates the aqueous phase while blue indicates the organic phase. The aqueous phase and the organic phase are immiscible. The black arrow points out the direction of the flow.

As for the segmented flow pattern, one phase is dispersed in the other. The segmented flow can be further divided into wet slug flow, dry slug flow and chaotic flow [28]. In the wet slug flow pattern, between the dispersed phase and the channel wall, there is a thin lubrication film of the continuous phase, as illustrated in Figure 1.5a. In this case, the dispersed phase is not in direct contact with the channel wall. In the dry slug flow pattern, as shown in Figure 1.5b, the thin lubrication film does not exist anymore and the dispersed phase is in direct contact with the channel wall. Figure 1.4b demonstrates dry slug flow in a microfluidic channel. In chaotic flow, the dispersed phase has a velocity component perpendicular to the direction of the main flow.

Regarding the geometry of the microfluidic channel, Figure 1.4 illustrates a so-called "double Y-shaped" microfluidic channel. The microfluidic channel has two inlets and two outlets as well as one main channel where the immiscible two phases meet. Besides the double Y-shaped microfluidic channel, there are microfluidic channels with "T-shaped", " Ψ -shaped", "Cross-shaped" and so on. Readers can refer to the following references for more information about the geometry of the microfluidic channel as well as its application in microfluidic liquid-liquid solvent extraction: *Ciceri et al.* [23], *Xu et al.* [28], *Assmann et al.* [29], *Kenig et al.* [30] and *Wang et al.* [31].

In general, the operation of microfluidic liquid-liquid solvent extraction can be divided

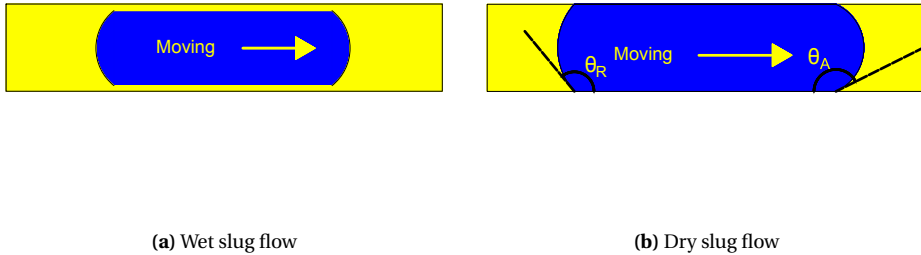


Figure 1.5: Schematic diagram of wet slug flow and dry slug flow inside a microfluidic channel. Yellow indicates the aqueous phase while blue indicates the organic phase. The aqueous phase and the organic phase are immiscible. The arrow points out the direction of the flow

into two steps: contact and separation of the immiscible two phases [29]. After entering the microfluidic channel, the two immiscible phases contact with each other at the inlets after which mass transport of the solutes occurs at the interface between the two phases. At the outlets of the microfluidic channel, the immiscible phases are separated. In the parallel flow pattern, ideally, the two phases leave the main channel separately through two outlets, achieving complete phase separation. Compared with parallel flow, phase separation for segmented flow is more complicated since the two phases do not flow out of the channel through separated outlets automatically. Thus, special treatments at the outlets are needed for the phase separation of segmented flow.

1.3.2. MICROFLUIDIC LIQUID-LIQUID SOLVENT EXTRACTION FOR RADIONUCLIDES

Besides the advantage of efficient extraction, the small-scale feature of microfluidic devices lowers the radiation exposure to researchers during the research and development stage. Such an approach fulfils the "As Low As Reasonably Achievable" standard when working with radiation [32][33]. For this reason, microfluidic liquid-liquid solvent extraction has already been utilized for the purification of radionuclides. This section briefly reviews the microfluidic liquid-liquid solvent extraction for radionuclides.

Microfluidic liquid-liquid extraction with the parallel flow pattern has been reported for the extraction of uranium. Hellé *et al.* conducted experiments of extracting U(VI) from a hydrochloric acid solution by the extractant Aliquat 336, which was dissolved in a mixture solution of n-dodecane and 1-decanol (1 %, v/v). They used a double Y-shaped glass microfluidic channel. Besides the experiments, they also performed numerical simulations to study the mass transport of U(VI) as well as the reaction at the interface

[34][35][36]. Extracting U(VI) from a nitric acid aqueous solution to an organic solution by tributylphosphate (TBP) with the parallel flow pattern were published separately by *Hotokezaka et al.* [37], *Zhang et al.* [38] and *Jasmin et al.* [39].

Besides uranium, microfluidic solvent extraction with the parallel flow pattern was also utilized for extracting other radionuclides. *Yasutoshi et al.* extracted americium (Am(III)) from a nitric acid solution to the solution of n-dodecane with octyl(phenyl)-N,N-diisobutyl-carbamoylmethylphosphineoxide [40]. *Yamamoto et al.* extracted plutonium (Pu(IV)) from a nitric acid solution to a solution of n-dodecane with tributylphosphate (TBP) [41]. *Ooe et al.* investigated extracting heavy element of dysprosium (^{150}Dy and ^{151}Dy) from an acetic acid-sodium acetate buffer solution to a 2-thenoyltrifluoroacetone-toluene solution [42].

Concerning work of purification radioisotopes for medical purpose, *Goyal et al.* reported their research of microfluidic liquid-liquid solvent extraction of radioactive copper-64 (^{64}Cu) from an aqueous solution to a toluene solution. In order to extract ^{64}Cu selectively, 2-hydroxy-4-noctyloxybenzophenone oxime (HOBO) was added to the toluene solution. HOBO served as the chelator agent which selectively reacted with copper. A double Y-shaped microfluidic platform, which was fabricated with a perfluoropolyether-based material, was used in their research. By exploiting the parallel flow pattern, they found that the extraction efficiency could be as high as 95 % [43].

Segmented flows were also applied for microfluidic solvent extraction of radionuclides. Several researchers published their results of extracting uranium with segmented flows [44] [45] [46].

1.4. PROBLEM DESCRIPTION

Because the small-dimension of microfluidic channels ensure a high extraction efficiency, in the conceptual design, ^{99}Mo can be extracted from the production loop by the parallel flow microfluidic liquid-liquid solvent extraction. Its working principle is schematically shown in Figure 1.6. The uranyl salt solution containing ^{99}Mo and other fission products is fed to the microfluidic channel through the upper inlet. An immiscible organic solution containing a specific extractant⁵ that selectively extracts ^{99}Mo enters the microfluidic channel at the other inlet. The two immiscible solutions flow parallelly inside the channel where ^{99}Mo is extracted from the aqueous phase to the organic phase. The two phases leave the microfluidic channel through the two outlets separately, achieving complete phase separation. If the microfluidic liquid-liquid solvent extraction of ^{99}Mo proves feasible, then a bundle of such microfluidic channels can be parallelized, to scale up the extraction capacity.

⁵Some published articles have discussed selectively extracting molybdenum from other elements using liquid-liquid solvent extraction [22] [47] while extracting molybdenum from fission products are not found. However, investigating the chemistry of extracting molybdenum is beyond the scope of this thesis.

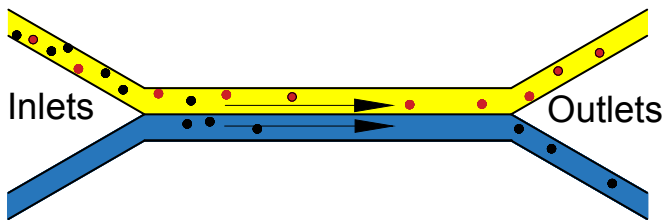


Figure 1.6: Schematic diagram of the microfluidic solvent extraction process inside a double Y-shaped channel with parallel flow pattern. Yellow indicates the aqueous phase while blue indicates the organic phase. The aqueous phase and the organic phase are immiscible. The black arrow indicates the direction of the flow. The black circles represent ^{99}Mo and the red circles represent other fission products.

Two practical problems arise when using the microfluidic solvent extraction for purifying ^{99}Mo . First, it is not clear how to establish and maintain the desired parallel flow pattern. It is important to keep the interface parallel to the main channel, as illustrated in Figure 1.6. Currently, it is still a challenge to accurately predict flow patterns inside a microfluidic channel. One of the reasons for this is that there are too many influencing factors. *Kashid et al.* have reported that both the diameter of the capillary tube and the dimension of the junction part of the microfluidic channel influence the flow pattern [48]. *Dessimoz et al.* have found that the properties (dynamic viscosity, density and interfacial tension) of the working fluids determine the flow pattern [49]. By investigating flow patterns inside microfluidic channels made of quartz or glass, *Salim et al.* have found that the construction material plays an important role by determining the wettability of the channel wall [50]. Besides, they have found that the fluid firstly injected into the microfluidic channel (*i.e.*, the initial conditions) determines the flow pattern as well. *Jovanovic et al.* have shown that increasing the length of the capillary tube can alter parallel flow into wavy annular flow [51]. Last but not least, the volumetric flow rates of both phases, as well as the volumetric flow rate ratio are all found to be influencing factors [52] [53]. Adding auxiliary accessories to the main microfluidic channel has been reported to help sustain a stable interface in the parallel flow pattern. For example, implementing partition walls [54] [55] [56] or a pillar structure [57] in the centre of the main channel might keep the interface stable⁶. In addition, a membrane has been utilized to

⁶ *Kositanon et al.* reported that the guideline structure did not improve the stability of parallel flow in their study [58].

produce a parallel flow [59] [60] [61] [62]. However, the method of adding auxiliary accessories in the centre of the main channel inevitably decreases the area of the contact surface and reduces the extraction efficiency. Besides, the membrane is not durable in the irradiation environment [63].

Another practical problem is that, even in the case of parallel flow, complete phase separation is very hard to achieve and, thus, there is often a leakage from one phase to the other, leading to contamination of the extracted ^{99}Mo , as shown in Figure 1.7. A too large contamination of the extracted ^{99}Mo is unacceptable because of the strict requirements of the chemical, radiochemical and radionuclidic purity⁷ of radiopharmaceuticals [65]. Surface modification can help to achieve better phase separation. In particular, partially changing the surface wettability of the glass microfluidic channel⁸ with organosilane makes it possible to maintain the aqueous phase in the hydrophilic side while keeping the organic phase in the hydrophobic side [66]. For instance, octadecyltrichlorosilane (OTS, one of the organosilane) can form a monolayer on the glass surface. The monolayer of OTS changes the glass surface from hydrophilic to hydrophobic. However, such kind of coating can degrade under irradiation. The monolayer of OTS deteriorates by gamma radiation from a Cobalt-60 source with a threshold value of 5 kGy [63].

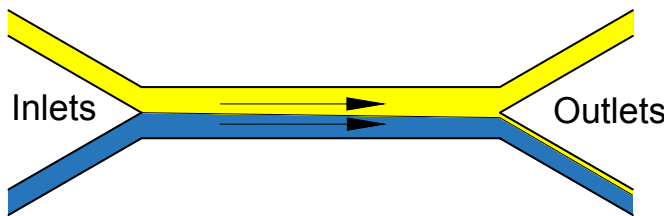


Figure 1.7: Schematic diagram of the leakage at the outlets of the microfluidic channel. The aqueous phase (yellow) is leaking to the organic phase (blue) at the outlets, resulting in contamination of the extracted ^{99}Mo .

⁷Chemical purity is defined as the desired substances present relative to the specified chemicals. Radiochemical purity is defined as the fraction of activity in the specific chemical form. Radionuclide purity is defined as the fraction of activity due to the specific radionuclides [64].

⁸Most of the polymer-based materials, including polydimethylsiloxane (PDMS), methyl methacrylate (PMMA), polycarbonate (PC) and polystyrene (PS), degrade under irradiation. Currently, glass is the ideal material for constructing microfluidic chips for solvent extraction of radionuclides.

This thesis is devoted to developing the Phase Field method in simulating multiphase flows inside a microfluidic channel, aiming to use it as a numerical tool to provide guidelines for avoiding the above-mentioned problems in designing the microfluidic channel and controlling flow conditions. Flow patterns changing from parallel flow to segmented flow attribute to topological changes of the interface. In this thesis, the topological change of the interface is termed the *Interface Breakup Problem*. The leakage at the outlet of the microfluidic channel is related to the *Moving Contact Line Problem*, *i.e.*, the movement of the interface between two immiscible phases on a solid surface [67]. Both the *Interface Breakup Problem* and the *Moving Contact Line Problem* are difficulties in modelling multiphase flows in microfluidics. In simulations of the *Interface Breakup Problem*, the thickness of the interface between the immiscible phases can be regarded as zero or finite, which requires different simulation techniques [68]. For the *Moving Contact Line*, the physics behind it is not entirely clear [69] [70] [71]. The difficulty in understanding the *Moving Contact Line Problem* originates from the fact that physical phenomena at different length scales are involved. For a multiphase flow in a microfluidic channel, the flow is governed by the hydrodynamic theory at the macroscopic scale, while the *Moving Contact Line* needs to be described at the microscopic scale with molecular-kinetic theory [72].

For the simulation of the *Interface Breakup Problem*, the Phase Field method introduces a diffusive interface with a finite thickness, within which the physical properties of the immiscible fluids (like density and viscosity) changes smoothly and continuously [73]. For the *Moving Contact Line Problem*, it attempts to integrate the hydrodynamic description and the molecular-kinetic description in one framework by including a diffusive transport of the order parameter (ϕ)⁹ within the interface to remove the mathematical singularity at the wall [74].

However, some aspects of the Phase Field method still need to be investigated. The capillary width (ϵ , a numerical parameter) determines the thickness of the diffusive interface, while the mobility parameter (M , a numerical parameter) determines the diffusive transport of the order parameter (ϕ). To make the calculation affordable, the thickness of the diffusive interface needs to be much larger than the one of the physical interface [75]. Concerning the *Interface Breakup Problem*, simulation results vary with variation of the capillary width (ϵ) and the mobility parameter (M) [76]. Thus, the exact influence of ϵ and M on the simulation results is still under debate [74] [77]. As for the *Moving Contact Line Problem*, it is found that when simulating the leakage at the outlet of the microfluidic channel with an equilibrium contact angle boundary condition (which is often applied in the Phase Field method [74] as explained in Section 2.5.1), the occurrence of leakage does not agree with experiments. One of the reasons may be that imposing the equilibrium contact angle boundary condition does not sufficiently capture the physics of the *Moving Contact Line* at the outlet.

⁹The variable that distinguishes different physical properties of the immiscible fluids in the Phase Field method.

1.5. RESEARCH OBJECTIVES AND THESIS OUTLINE

The **Research Objectives** of this work are:

1. to understand the effects of the numerical parameters of the Phase Field method (*i.e.*, capillary width (ϵ) and the mobility parameter (M)) on the predicted multiphase flow features in a double Y-shaped microfluidic channel.
2. to assess the capability of a non-equilibrium contact angle boundary condition (Equation 2.39 with $\mu_f > 0 \text{ Pa} \cdot \text{s}$) in the Phase Field method in simulating the *Moving Contact Line* between two partially wetting fluids inside a microfluidic channel, by validating simulation results with experiments.
3. to develop the Phase Field method for modelling parallel flow as well as the leakage phenomenon in a microfluidic channel, with the aim to evaluate its ability to accurately capture the physics between two immiscible fluids and predict their flow patterns.

These research objectives are addressed in the next chapters, and the **thesis outline** is as follows:

In **Chapter 2**, the theory behind multiphase flows in microfluidics and the Phase Field method is briefly introduced.

In **Chapter 3**, to ensure the Phase Field method generating consistent simulation results corresponding to the same physical phenomenon, influences of the capillary width (ϵ) and the mobility parameter (M) are investigated by modelling dry slug flow (with Ca number of both phases smaller than 1×10^{-3}) inside a double Y-shaped microfluidic channel. Focus is given to the choice of ϵ and M on the slug length, which is a quantitatively measurable feature of multiphase flows. Considering ϵ is an artificially chosen parameter that determines the thickness of the diffusive interface in the Phase Field method, this chapter reveals how M should be varied accordingly when ϵ is changed. Additionally, simulation results of the slug length are compared with experiments.

In **Chapter 4**, the influence of a non-equilibrium contact angle boundary condition on the *Moving Contact Line* is investigated by modelling dry slug flow with the Phase Field method. When simulating two partially wetting fluids in microfluidics, capturing the physics of the *Moving Contact Line* is of paramount importance. It has been noticed that the *Moving Contact Line* is not modelled correctly with the equilibrium contact angle boundary condition used in Chapter 3. Therefore, this study concentrates on the non-equilibrium contact angle boundary condition first proposed by *Jacqmin* [75]. *Carlson et al.* have found that such a boundary condition results in more physical results in capturing the droplet spreading process [78]. Nevertheless, not all mechanisms of this boundary condition are fully understood and it is not known if it is universally applicable in other multiphase flows [74], especially for dry slug flow. Due to the *Moving Contact Line*,

the apparent contact angles (θ_{app}) of the slugs deviate from the equilibrium contact angle (θ_e) measured at stationary conditions. Thus, by comparing the apparent contact angles (θ_{app}) in the simulations with those in the experiments, this chapter examines if the non-equilibrium contact angle boundary condition can reflect the effect of the *Moving Contact Line* correctly in microfluidics. Besides, impacts of the numerical parameters (ϵ and M) are also discussed.

In **Chapter 5**, parallel flow is studied with the help of the Phase Field method and validated with experiments. Currently, there are no clear criteria for accurately predicting flow patterns in microfluidic channels. This chapter simulates the parallel flow pattern in a double Y-shaped microfluidic channel with the Phase Field method, aims to utilize it as a numerical tool to understand the occurrence of parallel flow. The Phase Field method has the advantage of being compatible with the no-slip boundary condition in continuum fluid dynamics so that no special treatments are required. The work of this chapter reveals the choice of the mobility parameter (M) and the capillary width (ϵ) of the Phase Field method on modelling parallel flow. Additionally, by combining simulations with experiments based on the toluene/water system and the n-heptane/water system, this study shows the dominating force that determines the occurrence of parallel flow inside the microfluidic chip under investigation here. Lastly, the effects of the contact angle between the liquids and the wall on the flow patterns are discussed.

In **Chapter 6**, the leakage phenomenon at the outlet of the microfluidic channel is investigated by combining the Phase Field method with experiments. The leakage phenomenon is common in the parallel multiphase flow pattern, which results in failure of the microfluidic solvent extraction. In this chapter, experiments present the influence of the volumetric flow rate ratio and the equilibrium contact angle (θ_e) on the leakage direction. In the Phase Field method, the effects of the equilibrium and non-equilibrium contact angle boundary conditions on modelling the leakage are discussed.

In **Chapter 7**, the main conclusions of this thesis and recommendations for future studies are provided.

1.6. NOMENCLATURE

Symbols	Description	Units
E_{free}	Free energy of the system	J
$E_{kinetic}$	Kinetic energy of the system	J
E_{mix}	Mixing energy between two fluids	J
E_{total}	Total energy of the system	J
E_{wall}	Wall surface free energy	J
f_{mix}	Mixing energy density	J/m ³
G	Generalized chemical potential	J/m ³
L	Characteristic length of the microfluidic channel	m
L_m	Slip length	m
M	Mobility parameter	m ³ s/kg
P	Pressure	Pa
t	Time	s
\mathbf{u}	Velocity	m/s
U	Characteristic velocity of the fluid	m/s
x	x-coordinate	m
y	y-coordinate	m
z	z-coordinate	m

Greek letters	Description	Units
ϵ	Capillary width	m
θ_A	Advancing contact angle	°
θ_{app}	Apparent contact angle	°
θ_e	Equilibrium contact angle	°
θ_m	Microscopic dynamic contact angle	°
θ_R	Receding contact angle	°
λ	Mixing energy density parameter	N
μ	Dynamic viscosity	Pa·s
μ_f	Contact line friction parameter	Pa·s
ρ	Density	kg/m ³
σ	Coefficient of interfacial tension	N/m
ϕ	Order parameter to distinguish different phases	
Φ	Volumetric flow rate at the inlet	µL/min

Non-dimensional groups	Description
Bo	Bond number
Ca	Capillary number
Ca_f	A dimensionless number for the contact line friction parameter
Cn	Cahn number
Pe	Péclet number
Re	Reynolds number
We	Weber number

Subscripts	Description
aq	Aqueous phase
org	Organic phase

REFERENCES

- [1] Bert Wolterbeek, Jan Leen Kloosterman, Danny Lathouwers, Martin Rohde, August Winkelmann, Lodewijk Frima, and Frank Wols. What is wise in the production of ^{99}Mo ? A comparison of eight possible production routes. *Journal of Radioanalytical and Nuclear Chemistry*, 302(2):773–779, 2014.
- [2] Eric W. Price and Chris Orvig. Matching chelators to radiometals for radiopharmaceuticals. *Chem. Soc. Rev.*, 43:260–290, 2014.
- [3] Michael AB Naafs. The global impact of the Mo-99 shortage. *Biomedical Journal of Scientific and Technical Research*, 4(5), 2018.
- [4] Maroor. Pillai, Ashutosh Dash, and F.F. (Russ) Knapp Jr. Sustained availability of ^{99m}Tc : Possible paths forward. *Journal of Nuclear Medicine*, 54:313–323, 2013.
- [5] Luis F. Metello. ^{99m}Tc -technetium shortage: Old problems asking for new solutions. *Journal of Medical Imaging and Radiation Sciences*, 46, 2015.
- [6] Thomas J. Ruth. The medical isotope crisis: How we got here and where we are going. *J. Nucl. Med. Technol.*, 42(4):245–248, 2014.
- [7] Kevin Charlton. The supply of medical radioisotopes: 2018 medical isotope demand and capacity projection for the 2018-2023 period. *OECD Nuclear Energy Agency*, 2018.
- [8] L.P. Roobol, C.E.N.M. Rosenbaum, and I.R. de Waard. Supply security for medical radionuclides - additions 2020. *RIVM letter report*, 2020.
- [9] Valeria N. Starovoitova, Lali Tchelidze, and Douglas P. Wells. Production of medical radioisotopes with linear accelerators. *Applied Radiation and Isotopes*, 85:39 – 44, 2014.

- [10] N.P. Dikiy, A.N. Dovbnya, D.V. Fedorchenko, and M.A. Khazhmuradov. Geant 4 simulation of ^{99}Mo photonuclear production in nanoparticles. *Applied Radiation and Isotopes*, 114:7 – 13, 2016.
- [11] Ebrahim Abedi, Marzieh Ebrahimpour, Amin Davari, Seyed Mohammad Mirvahili, Mohsen Tabasi, and Mohammad Ghannadi Maragheh. Neutronic and thermal-hydraulic analysis of fission molybdenum-99 production at tehran research reactor using LEU plate targets. *Applied Radiation and Isotopes*, 118:160 – 166, 2016.
- [12] Marco Capogni, Antonino Pietropaolo, Lina Quintieri, Maurizio Angelone, Alessandra Boschi, Mauro Capone, Nadia Cherubini, Pierino De Felice, Alessandro Dodaro, Adriano Duatti, Aldo Fazio, Stefano Loreti, Petra Martini, Guglielmo Pagano, Micol Pasquali, Mario Pillon, Licia Uccelli, and Aldo Pizzutto. 14 MeV neutrons for $^{99}\text{Mo}/^{99m}\text{Tc}$ production: Experiments, simulations and perspectives. *Molecules*, 23(8), 2018.
- [13] Abdessamad Didi, Ahmed Dadouch, Otman Jai, and Fatima Bouhali. Toward for production of Molybdenum-99 by irradiation of MoO_3 target in a neutron flux. *Bangladesh Journal of Medical Science*, 17(4):567–572, 2018.
- [14] Masayuki Hagiwara, Hiroshi Yashima, Toshiya Sanami, and Shunsuke Yonai. Measurement of the excitation function of $^{96}\text{Zr}(\text{a},\text{n})^{99}\text{Mo}$ for an alternative production source of medical radioisotopes. *Journal of Radioanalytical and Nuclear Chemistry*, 318:569–573, 2018.
- [15] Gaia Pupillo, Juan Esposito, Ferid Haddad, Nathalie Michel, and Mauro Gambacini. Accelerator-based production of ^{99}Mo : a comparison between the $^{100}\text{Mo}(\text{p},\text{x})$ and $^{96}\text{Zr}(\text{a},\text{n})$ reactions. *J Radioanal Nucl Chem*, 305:73 – 78, 2015.
- [16] IAEA. Homogeneous aqueous solution nuclear reactors for the production of Mo-99 and other short-lived radioisotopes. Vienna, 2008. AEA-TECDOC-1601.
- [17] Jurriaan A. R. Huisman. Heat transfer of the Mo-99 research loop: Optimising heat transfer of the closed reactor loop aimed at the efficient production of molybdenum-99. Bachelor's thesis, Delft University of Technology, 2016.
- [18] Kenneth Elgin. A study of the feasibility of ^{99}Mo production inside the TU Delft Hoger Onderwijs Reactor. Bachelor's thesis, Delft University of Technology, 2015.
- [19] C.C. Pothoven. Recirculation of the Mo-99 research loop: predicting the long-term behaviour of the the loop content. Bachelor's thesis, Delft University of Technology, 2016.
- [20] Lingling Shui, Jan C.T. Eijkel, and Albert van den Berg. Multiphase flow in microfluidic systems – control and applications of droplets and interfaces. *Advances in Colloid and Interface Science*, 133(1):35 – 49, 2007.
- [21] Daniel Mark, Stefan Haeberle, Günter Roth, Felix von Stetten, and Roland Zengerle. Microfluidic lab-on-a-chip platforms: requirements, characteristics and applications. *Chem. Soc. Rev.*, 39:1153–1182, 2010.

- [22] Li Zeng, Xiaoli Liao, Yahui Sun, and Liansheng Xiao. Direct extraction of molybdenum from high acid leach solutions of Ni–Mo ore using an oxime extractant of HBL101. *International Journal of Refractory Metals and Hard Materials*, 51:14 – 18, 2015.
- [23] Davide Ciceri, Jilska M. Perera, and Geoffrey W. Stevens. The use of microfluidic devices in solvent extraction. *Journal of Chemical Technology & Biotechnology*, 89(6):771–786, 2014.
- [24] Benny Malengier and Subramaniam Pushpavanam. Comparison of co-current and counter-current flow fields on extraction performance in micro-channels. *Advances in Chemical Engineering and Science*, 2(2):309–320, 2012.
- [25] Arata Aota, Akihide Hibara, and Takehiko Kitamori. Pressure balance at the liquid–liquid interface of micro countercurrent flows in microchips. *Analytical Chemistry*, 79(10):3919–3924, 2007.
- [26] Arata Aota, Akihide Hibara, Kyosuke Shinohara, Yasuhiko Sugii, Koji Okamoto, and Takehiko Kitamori. Flow velocity profile of micro counter-current flows. *Analytical Sciences*, 23(2):131–133, 2007.
- [27] Arata Aota, Akihide Hibara, Yasuhiko Sugii, and Takehiko Kitamori. Shape of the liquid–liquid interface in micro counter-current flows. *Analytical Sciences*, 28(1):9–9, 2012.
- [28] Cong Xu and Tingliang Xie. Review of microfluidic liquid–liquid extractors. *Industrial & Engineering Chemistry Research*, 56(27):7593–7622, 2017.
- [29] N. Assmann, A. Ładosz, and P. Rudolf von Rohr. Continuous micro liquid-liquid extraction. *Chemical Engineering & Technology*, 36(6):921–936, 2013.
- [30] Eugeny Y. Kenig, Yuanhai Su, Anna Lautenschleger, Paris Chasanis, and Marcus Grünewald. Micro-separation of fluid systems: A state-of-the-art review. *Separation and Purification Technology*, 120:245 – 264, 2013.
- [31] Kai Wang and Guangsheng Luo. Microflow extraction: A review of recent development. *Chemical Engineering Science*, 169:18 – 33, 2017.
- [32] Hein Heidbuchel, Fred H.M. Wittkampf, Eliseo Vano, Sabine Ernst, Richard Schilling, Eugenio Picano, Lluis Mont, and ESC Scientific Document Group. Practical ways to reduce radiation dose for patients and staff during device implantations and electrophysiological procedures. *EP Europace*, 16(7):946–964, 05 2014.
- [33] Clarisse Mariet, Axel Vansteene, Marion Losno, Julien Pellé, Jean-Philippe Jasmin, Anthony Bruchet, and Gwendolyne Hellé. Microfluidics devices applied to radionuclides separation in acidic media for the nuclear fuel cycle. *Micro and Nano Engineering*, 3:7 – 14, 2019.

- [34] Gwendolyne Hellé, Clarisse Mariet, and Gérard Cote. Liquid–liquid microflow patterns and mass transfer of radionuclides in the systems Eu(III)/HNO₃/DMDBT DMA and U(VI)/HCl/Aliquat® 336. *Microfluidics and Nanofluidics*, 17(6):1113–1128, Dec 2014.
- [35] Gwendolyne Hellé, Sean Roberston, Siméon Cavadias, Clarisse Mariet, and Gérard Cote. Toward numerical prototyping of labs-on-chip: modeling for liquid–liquid microfluidic devices for radionuclide extraction. *Microfluidics and Nanofluidics*, 19(5):1245–1257, Nov 2015.
- [36] Gwendolyne Hellé, Clarisse Mariet, and Gérard Cote. Liquid–liquid extraction of uranium(VI) with Aliquat® 336 from HCl media in microfluidic devices: Combination of micro-unit operations and online ICP-MS determination. *Talanta*, 139:123 – 131, 2015.
- [37] Hiroyasu Hotokezaka, Manabu Tokeshi, Masayuki Harada, Takehiko Kitamori, and Yasuhisa Ikeda. System for high-level radioactive waste using microchannel chip — extraction behavior of metal ions from aqueous phase to organic phase in microchannel. *Progress in Nuclear Energy*, 47(1):439 – 447, 2005.
- [38] Jing Zhang, Zhen Qin, Dachao Deng, Junsheng Liao, Xingjian Wei, and Ning Zhang. A novel method for the online measurement of impurities in uranium by coupling microfluidics with ICP-MS. *J. Anal. At. Spectrom.*, 31:934–939, 2016.
- [39] Jean-Philippe Jasmin, Axel Vansteene, Thomas Vercouter, and Clarisse Mariet. A simple and adaptive methodology to use a commercial solvent extraction microsystem as screening tool: Validation with the U-TBP chemical system. *Solvent Extraction and Ion Exchange*, 35(3):174–186, 2017.
- [40] Yasutoshi Ban, Yoshikuni Kikutani, Manabu Tokeshi, and Yasuji Morita. Extraction of Am(III) at the interface of organic-aqueous two-layer flow in a microchannel. *Journal of Nuclear Science and Technology*, 48(10):1313–1318, 2011.
- [41] Masahiko Yamamoto, Shigeo Taguchi, Soichi Sato, and Naoki Surugaya. Evaluation of plutonium(IV) extraction rate between nitric acid and tri-n-butylphosphate solution using a glass chip microchannel. *Journal of Separation Science*, 38(10):1807–1812, 2015.
- [42] K. Ooe and A. Shinohara. Development of on-line solvent extraction system with microchips for heavy element chemistry. *Journal of Nuclear and Radiochemical Sciences*, 8:59–62, 2007.
- [43] Sachit Goyal, Amit V. Desai, Robert W. Lewis, David R. Ranganathan, Hairong Li, Dexing Zeng, David E. Reichert, and Paul J.A. Kenis. Thiolene and sifel-based microfluidic platforms for liquid–liquid extraction. *Sensors and Actuators B: Chemical*, 190:634 – 644, 2014.
- [44] Mayur Darekar, K.K. Singh, S. Mukhopadhyay, K.T. Shenoy, and S.K. Ghosh. Solvent extraction in microbore tubes with UNPS–TBP in dodecane system. *Separation and Purification Technology*, 128:96 – 105, 2014.

- [45] Dimitrios Tsiaoulidis, Valentina Dore, Panagiota Angelis, Natalia V. Plechkova, and Kenneth R. Seddon. Extraction of dioxouranium(VI) in small channels using ionic liquids. *Chemical Engineering Research and Design*, 91(4):681 – 687, 2013.
- [46] Dimitrios Tsiaoulidis, Valentina Dore, Panagiota Angelis, Natalia V. Plechkova, and Kenneth R. Seddon. Dioxouranium(VI) extraction in microchannels using ionic liquids. *Chemical Engineering Journal*, 227:151 – 157, 2013.
- [47] Peter Tkac, M. Alex Brown, Abdul Momen, Kent E. Wardle, Jacqueline M. Copple, and George F. Vandegrift. MOEX: Solvent extraction approach for recycling enriched $^{98}\text{Mo}/^{100}\text{Mo}$ material. *Separation Science and Technology*, 53(12):1856–1863, 2018.
- [48] Madhvanand N. Kashid and David W. Agar. Hydrodynamics of liquid–liquid slug flow capillary microreactor: Flow regimes, slug size and pressure drop. *Chemical Engineering Journal*, 131(1):1 – 13, 2007.
- [49] Anne-Laure Dessimoz, Laurent Cavin, Albert Renken, and Lioubov Kiwi-Minsker. Liquid–liquid two-phase flow patterns and mass transfer characteristics in rectangular glass microreactors. *Chemical Engineering Science*, 63(16):4035 – 4044, 2008.
- [50] Abdelkader Salim, Mostafa Fourar, Jacques Pironon, and Judith Sausse. Oil–water two-phase flow in microchannels: Flow patterns and pressure drop measurements. *The Canadian Journal of Chemical Engineering*, 86(6):978–988, 2008.
- [51] Jovan Jovanović, Evgeny V. Rebrov, T. A. (Xander) Nijhuis, M. T. Kreutzer, Volker Hessel, and Jaap C. Schouten. Liquid–liquid flow in a capillary microreactor: Hydrodynamic flow patterns and extraction performance. *Industrial & Engineering Chemistry Research*, 51(2):1015–1026, 2012.
- [52] P. S. Sarkar, K. K. Singh, K. T. Shenoy, A. Sinha, H. Rao, and S. K. Ghosh. Liquid–liquid two-phase flow patterns in a serpentine microchannel. *Industrial & Engineering Chemistry Research*, 51(13):5056–5066, 2012.
- [53] Hooman Foroughi and Masahiro Kawaji. Viscous oil–water flows in a microchannel initially saturated with oil: Flow patterns and pressure drop characteristics. *International Journal of Multiphase Flow*, 37(9):1147 – 1155, 2011.
- [54] Tatsuo Maruyama, Tomoaki Kaji, Tomohiro Ohkawa, Ken-ichiro Sotowa, Hironari Matsushita, Fukiko Kubota, Noriho Kamiya, Katsuki Kusakabe, and Masahiro Goto. Intermittent partition walls promote solvent extraction of metal ions in a microfluidic device. *Analyst*, 129:1008–1013, 2004.
- [55] Tomohiko Tagawa, Salah Aljbour, Mohammed Matouq, and Hiroshi Yamada. Micro-channel reactor with guideline structure for organic–aqueous binary system. *Chemical Engineering Science*, 62(18):5123 – 5126, 2007.
- [56] Chayanoont Kositanont, Sompong Putivisutisak, Piyasan Praserthdam, Suttichai Assabumrungrat, Hiroshi Yamada, and Tomohiko Tagawa. Flow pattern of liquid

- multiphase flow in microreactors with different guideline structures. *Journal of Chemical Engineering of Japan*, 44(9):649–652, 2011.
- [57] J. Berthier, Van-Man Tran, F. Mittler, and N. Sarrut. The physics of a coflow micro-extractor: Interface stability and optimal extraction length. *Sensors and Actuators A: Physical*, 149(1):56 – 64, 2009.
- [58] C. Kositanont, S. Putivisutisak, T. Tagawa, H. Yamada, and S. Assabumrungrat. Multiphase parallel flow stabilization in curved microchannel. *Chemical Engineering Journal*, 253:332 – 340, 2014.
- [59] Zeng-Xuan Cai, Qun Fang, Heng-Wu Chen, and Zhao-Lun Fang. A microfluidic chip based liquid–liquid extraction system with microporous membrane. *Analytica Chimica Acta*, 556(1):151 – 156, 2006.
- [60] W. E. TeGrotenhuis, R. J. Cameron, M. G. Butcher, P. M. Martin, and R. S. Wegeng. Microchannel devices for efficient contacting of liquids in solvent extraction. *Separation Science and Technology*, 34(6-7):951–974, 1999.
- [61] Jonas Hereijgers, Manly Callewaert, Xinjian Lin, Harry Verelst, Tom Breugelmans, Heidi Ottevaere, Gert Desmet, and Wim De Malsche. A high aspect ratio membrane reactor for liquid–liquid extraction. *Journal of Membrane Science*, 436:154 – 162, 2013.
- [62] Sira Nititayanontakit, Pakorn Varanusupakul, and Manuel Miró. Hybrid flow analyzer for automatic hollow-fiber-assisted ionic liquid-based liquid-phase microextraction with in-line membrane regeneration. *Analytical and Bioanalytical Chemistry*, 405(10):3279–3288, Apr 2013.
- [63] R. Wenmaekers. The use of microfluidics for the purification of medical radioisotopes. Master's thesis, Delft University of Technology, 2018.
- [64] James A. Ponto. The AAPM/RSNA physics tutorial for residents: Radiopharmaceuticals. *Imaging and Therapeutic Technology*, 18:1395 – 1404, 1998.
- [65] Petra Martini, Andrea Adamo, Neilesh Syna, Alessandra Boschi, Licia Uccelli, Nopphon Weeranoppanant, Jack Markham, and Giancarlo Pascali. Perspectives on the use of liquid extraction for radioisotope purification. *Molecules*, 24(2), 2019.
- [66] Tatsuo Maruyama, Hironari Matsushita, Jun-ichi Uchida, Fukiko Kubota, Noriho Kamiya, and Masahiro Goto. Liquid membrane operations in a microfluidic device for selective separation of metal ions. *Analytical Chemistry*, 76(15):4495–4500, 2004.
- [67] Yi Sui, Hang Ding, and Peter D.M. Spelt. Numerical simulations of flows with moving contact lines. *Annual Review of Fluid Mechanics*, 46(1):97–119, 2014.
- [68] Martin Wörner. Numerical modeling of multiphase flows in microfluidics and micro process engineering: a review of methods and applications. *Microfluidics and Nanofluidics*, 12(6):841–886, May 2012.

- [69] Terence D. Blake. The physics of moving wetting lines. *Journal of Colloid and Interface Science*, 299(1):1 – 13, 2006.
- [70] Jinyuan Qian, Xiaojuan Li, Zan Wu, Zhijiang Jin, and Bengt Sunden. A comprehensive review on liquid–liquid two-phase flow in microchannel: flow pattern and mass transfer. *Microfluidics and Nanofluidics*, 23:116, 2019.
- [71] Daniel Bonn, Jens Eggers, Joseph Indekeu, Jacques Meunier, and Etienne Rolley. Wetting and spreading. *Rev. Mod. Phys.*, 81:739–805, May 2009.
- [72] Jacco H. Snoeijer and Bruno Andreotti. Moving contact lines: Scales, regimes, and dynamical transitions. *Annual Review of Fluid Mechanics*, 45(1):269–292, 2013.
- [73] Pengtao Yue, Chunfeng Zhou, James J. Feng, Carl F. Ollivier-Gooch, and Howard H. Hu. Phase-field simulations of interfacial dynamics in viscoelastic fluids using finite elements with adaptive meshing. *Journal of Computational Physics*, 219(1):47 – 67, 2006.
- [74] P. Yue and J. J. Feng. Can diffuse-interface models quantitatively describe moving contact lines? *The European Physical Journal Special Topics*, 197(1):37, Aug 2011.
- [75] David Jacqmin. Calculation of two-phase Navier–Stokes flows using phase-field modeling. *Journal of Computational Physics*, 155(1):96 – 127, 1999.
- [76] Pengtao Yue, James J. Feng, Chun Liu, and Jie Shen. A diffuse-interface method for simulating two-phase flows of complex fluids. *Journal of Fluid Mechanics*, 515:293–317, 2004.
- [77] F. Magaletti, F. Picano, M. Chinappi, L. Marino, and C. M. Casciola. The sharp-interface limit of the Cahn–Hilliard/Navier–Stokes model for binary fluids. *Journal of Fluid Mechanics*, 714:95–126, 2013.
- [78] A. Carlson, M. Do-quang, and G. Amberg. Dissipation in rapid dynamic wetting. *Journal of Fluid Mechanics*, 682:213–240, 2011.

2

THEORY

2.1. BASIC CONCEPTS OF MICROFLUIDICS

A fluid, either liquid or gas, can deform and move continuously under the action of external forces [1]. In microfluidics, the behaviour of fluids can still be described by fluid dynamics. Due to the small-dimension feature of the microfluidic channel, some of the common fluid behaviour, *e.g.* turbulence, is rare. This section introduces the theory related to microfluidics and multiphase flows in microfluidic channels.

2.1.1. THE CONTINUITY EQUATION

The basic constituents in fluid dynamics are fluid elements. A fluid element has a finite size and contains a large amount of molecules. In the fluid element, the macroscopic properties of the fluid, such as mass, momentum, and energy are perfectly continuous. Regarding the fluid as continuous is also called the continuum hypothesis. One thing to note is that the continuum hypothesis holds in microfluidics while it breaks down in nano-channels [1].

Based on the continuum hypothesis and the idea of mass conservation, one can derive the continuity equation:

$$\frac{\partial \rho}{\partial t} + \nabla \cdot (\rho \mathbf{u}) = 0, \quad (2.1)$$

where ρ is the density (kg/m^3) and \mathbf{u} is the velocity (m/s).

In microfluidic liquid-liquid solvent extraction, the working liquids are considered to be incompressible. For incompressible fluids, Equation 2.1 can be written as:

$$\nabla \cdot \mathbf{u} = 0. \quad (2.2)$$

2.1.2. NAVIER-STOKES EQUATIONS FOR INCOMPRESSIBLE FLUIDS

Applying Newton's second law on fluid elements, one can derive the Navier-Stokes momentum equations. The Navier-Stokes momentum equations describe the motion of Newtonian fluids. For incompressible fluids, the Navier-Stokes momentum equations are written as:

$$\rho \frac{\partial \mathbf{u}}{\partial t} + \rho (\mathbf{u} \cdot \nabla) \mathbf{u} = -\nabla P + \mu \nabla^2 \mathbf{u} + \mathbf{F}_g + \mathbf{F}_{it}, \quad (2.3)$$

where P is the pressure (Pa), μ is the dynamic viscosity ($\text{Pa} \cdot \text{s}$) of the fluid, \mathbf{F}_{it} is the interfacial tension force and \mathbf{F}_g is the gravitational force.

As mentioned above, turbulent flows are rare in microfluidic channels. The flow regime of turbulent flow or laminar flow in a tube can be characterized by the *Reynolds* (Re) number. The Re number is defined as the ratio of the inertial force to the viscous force:

$$Re = \frac{\rho UL}{\mu}, \quad (2.4)$$

where L is the characteristic length of the tube. U is the characteristic velocity of the fluid which takes the average velocity of the flow at the inlet of the tube. Typically, when the Re number exceeds 2500, turbulent flow occurs [2]. Due to the small diameter of a microfluidic channel, the Re number is usually less than 2500. As a typical example, considering water ($\rho_{water} = 1 \times 10^3 \text{ kg/m}^3$, $\mu_{water} = 1 \times 10^{-3} \text{ Pa}\cdot\text{s}$) flowing inside a microfluidic channel with volumetric flow rate of $20 \mu\text{L}/\text{min}$. The microfluidic channel has a diameter of $100 \mu\text{m}$ which is regarded as the characteristic length. It can be calculated that the Re number is 4.25. Such a small Re number ensures that the flow inside a microfluidic channel is laminar.

2

2.1.3. MULTIPHASE FLOWS IN MICROFLUIDIC CHANNELS

Section 2.1.2 has introduced water flows through a microfluidic channel under laminar flow condition, which belongs to single-phase flows. This section introduces multiphase flows in microfluidic channels. A phase is a distinct state of matter which has identical chemical composition and physical state and can be separated from other phases by the phase interface. An interface is the thin boundary layer which separates the two phases [3]. Multiphase flows in microfluidic channels indicate that there are at least two immiscible phases existing and flowing inside microfluidic channels. The immiscible two phases in microfluidics usually can be liquid-liquid or liquid-gas phases.

Compared with single-phase flows, multiphase flows inside microfluidic channels are characterized by the interfacial tension ¹ between two phases. In the bulk phase, the net cohesive force on a molecule is zero; however, for molecules at the interface, the cohesive forces from the two phases are different, which results in bending of the interface. In addition, interfacial tension can also be interpreted from an energy point of view. Based on the theory of Gibbs free energy, molecules at the interface lose chemical bonds in the normal direction of the interface. Consequently, the energy of the molecules at the interface is higher than that of the molecules in bulk. For the phase to minimize the total energy, the number of molecules at the interface should be minimized. The minimized number of molecules at the interface leads to a minimal surface area, which is smoothly bent [1]. The SI unit of the interfacial tension can be expressed as force per length (N/m) or Gibbs free energy per area (J/m^2).

As introduced in Section 1.3.1, there are various flow patterns of multiphase flows inside microfluidic channels. Besides the Re number, multiphase flow patterns can be characterized by several other dimensionless numbers which are related to interfacial tension.

The *Capillary* number (Ca) is one of the most important dimensionless numbers to describe multiphase flows. The Ca number describes the ratio of the viscous force to the

¹In this thesis, the tension between two liquid phases is called "interfacial tension" while the tension between liquid and gas is termed "surface tension".

interfacial tension.

$$Ca = \frac{\mu U}{\sigma}, \quad (2.5)$$

2

where σ (in N/m) is the coefficient of interfacial tension. It is generally accepted that parallel flow occurs at high Ca number while segmented flow occurs at low Ca number [3] [4] [5].

One other frequently used dimensionless number is the *Weber* number (We). It describes the relative importance of the fluid's inertia to the interfacial tension. *Zhao et al.* have proved that the We number can be used to predict flow patterns in a T-shaped microfluidic channel [6],

$$We = \frac{\rho U^2 L}{\sigma}. \quad (2.6)$$

The *Bond* number (Bo) describes the relative importance of the gravitational force to interfacial tension. When the Bo number is less than 0.05, the effect of the gravitational force can be neglected [7].

$$Bo = \frac{\Delta \rho L^2 g}{\sigma}, \quad (2.7)$$

where g is the magnitude of the gravitational acceleration. As a typical example, when water ($\rho_{water}=1\times 10^3$ kg/m³) and the immiscible organic solvent toluene ($\rho_{toluene}=0.87\times 10^3$ kg/m³, $\sigma_{water-toluene}=0.00361$ N/m) flow inside a microfluidic channel with a diameter of 100 μm, the Bo number is calculated to be 3.53×10^{-4} . Thus, the effect of the gravitational force is usually neglected in multiphase flows in microfluidics.

2.2. THE PHYSICS OF WETTING

Due to the small-dimension feature of microfluidic devices, wetting phenomena are crucial for predicting and investigating multiphase flows in microfluidic channels [3]. This section introduces the basic wetting phenomena.

Wetting phenomena are very common in our daily life, *e.g.*, a droplet of water is put on the surface of a table or on the leaf of a lotus. At stationary conditions, one will find that the shape of the water droplet on the table surface is different from that on the lotus leaf. Figure 2.1 schematically presents a typical wetting case: a liquid droplet wets the surface of a solid in ambient gas. In Figure 2.1, three phases are involved: the liquid phase, the gas phase and the solid phase. At the joint position where the liquid phase, the gas phase and the solid phase meet, a so-called three-phase contact line (contact line for short) can be drawn. Figure 2.1 shows a 2-dimensional, lateral view of wetting. Since Figure 2.1 is a lateral view of wetting, the contact line appears as a point. Wetting is often characterized by a contact angle, formed at the contact line. In addition, wetting can be further categorized into static wetting and dynamic wetting, which will be explained in detail in Section 2.2.1 and Section 2.2.2, respectively.

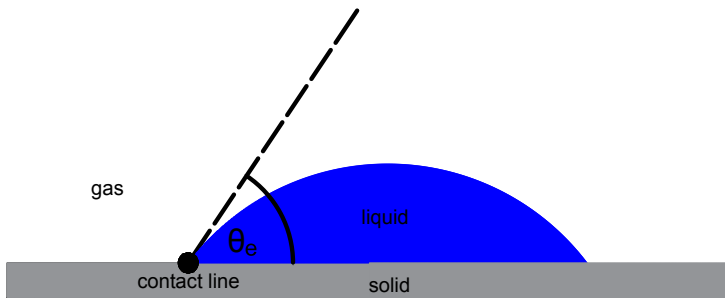


Figure 2.1: Schematic diagram of wetting. A liquid droplet in ambient gas wets the surface of a solid, forming an equilibrium contact angle (θ_e). At the joint position where the liquid, the gas and the solid meet, there is a three-phase contact line. Since this is a 2-dimensional lateral view, the contact line appears as a point.

2.2.1. STATIC WETTING

As illustrated in Figure 2.1, when the interface between a liquid phase and a gas phase touches a solid surface, there is a contact angle forming at the contact line where the three phases join. If the surface is ideal (perfectly smooth and chemically homogeneous), at stationary conditions, the contact angle is called the equilibrium contact angle (θ_e). Based on Gibbs free energy, there is surface tension between the solid-gas interface and the solid-liquid interface, denoted as σ_{sg} and σ_{sl} , respectively. The value of the contact angle can be quantified by the surface tension among the three phases by Young's law [1]:

$$\cos(\theta_e) = \frac{\sigma_{sg} - \sigma_{sl}}{\sigma}, \quad (2.8)$$

where σ is coefficient of surface tension between the gas phase and the liquid phase which has already been introduced in Section 2.1.3. The equilibrium contact angle (θ_e) can be used for measuring the wettability of a solid surface. When $\theta_e > 90^\circ$, the surface is termed hydrophobic and when $\theta_e < 90^\circ$, the surface is termed hydrophilic.

In principle, the equilibrium contact angle (θ_e) reflects molecular interactions between the solid, liquid and gas phase. In practice, the equilibrium contact angle (θ_e) is measured at the macroscopic scale, which is above the molecular scale [8]. The contact angle measured at the macroscopic scale is termed the apparent contact angle (θ_{app}). At stationary conditions, the apparent contact angle (θ_{app}) is assumed the same as the equilibrium contact angle (θ_e).

2.2.2. DYNAMIC WETTING

In the case of dynamic wetting when the three-phase contact line moves, the situation becomes complex. The complexity comes from that the contact angle differs at different length scales. Figure 2.2 schematically illustrates a liquid droplet which is moving on a solid surface. When the droplet is moving relative to the solid surface, the apparent contact angle (θ_{app}) can be measured at the macroscopic scale.

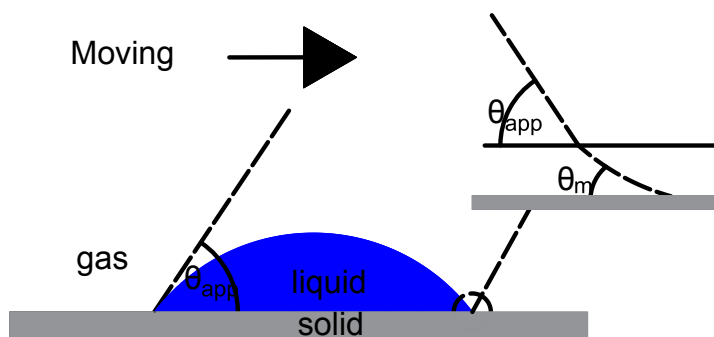


Figure 2.2: Schematic diagram of apparent contact angle (θ_{app}) and microscopic dynamic contact angle (θ_m). The droplet is moving on the surface of a solid plate. The apparent contact angle (θ_{app}) is observed at the macroscopic scale while the microscopic dynamic contact angle (θ_m) is observed at the microscopic scale.

Zooming in towards the position where θ_{app} locates in Figure 2.2, there is a microscopic dynamic contact angle (θ_m), which is different from the apparent contact angle (θ_{app}). The microscopic length scale ranges from hundreds of nanometer to tens of micrometer [11].

Keeping zooming in at the position where the microscopic dynamic contact angle (θ_m)

towards the molecular scale, there is the equilibrium contact angle (θ_e)². As mentioned in Section 2.2.1, in the case of static wetting, the equilibrium contact angle (θ_e) can be considered the same as the apparent contact angle (θ_{app}). However, in the dynamic wetting process, the equilibrium contact angle (θ_e) and the apparent contact angle (θ_{app}) are different.

Until now, there is no solid conclusion about the relationship between θ_e , θ_m and θ_{app} in dynamic wetting. Currently, their relationship depends on different theoretical models. The relationship between θ_e , θ_m and θ_{app} as well as the theoretical models will be discussed in detail in Section 2.3.

2.2.3. CONTACT ANGLE HYSTERESIS

In Section 2.2.1 and Section 2.2.2, it is assumed the solid surface is ideal, *i.e.*, perfectly smooth and chemically homogeneous. However, in practice, such an ideal surface does not exist. On the surface of non-ideal solids, contact angle hysteresis appears [12]. The contact angle hysteresis can be further categorized as the static contact angle hysteresis and the dynamic contact angle hysteresis, which occur in the case of static wetting and dynamic wetting, respectively.

Figure 2.3 schematically demonstrates the static contact angle hysteresis. A liquid droplet is originally placed on the surface of a non-ideal solid plate. Inclining one side of the solid plate slowly, because of the gravitational force, the liquid droplet has the tendency to move downwards. One can find that the contact angles at the two sides of the droplet are different. The contact angle in front of the droplet is called the advancing contact angle (θ_A) while the contact angle at the back is called the receding contact angle (θ_R). Obviously, both the advancing contact angle (θ_A) and the receding contact angle (θ_R) belong to the apparent contact angle (θ_{app}) since they are measured at the macroscopic scale. Keeping inclining the solid plate slowly, before reaching the critical slope at which the three-phase contact line starts to move, the difference between θ_A and θ_R is called the static contact angle hysteresis [8].

Besides occurring in the static wetting, the contact angle hysteresis also takes place in the dynamic case. When the slope of the inclination is large enough, the three-phase contact line moves and the droplet slips downwards. In this case, the difference between θ_A and θ_R is called the dynamic contact angle hysteresis.

Until now, there is no concrete consensus of the hysteresis phenomenon [8][13]. It is commonly accepted that the static contact angle hysteresis originates from the roughness and chemical heterogeneities of the solid surface. Besides the surface property, the dynamic contact angle hysteresis also arises from the movement of the contact line itself [14].

²The equilibrium contact angle (θ_e) is not shown in Figure 2.2.

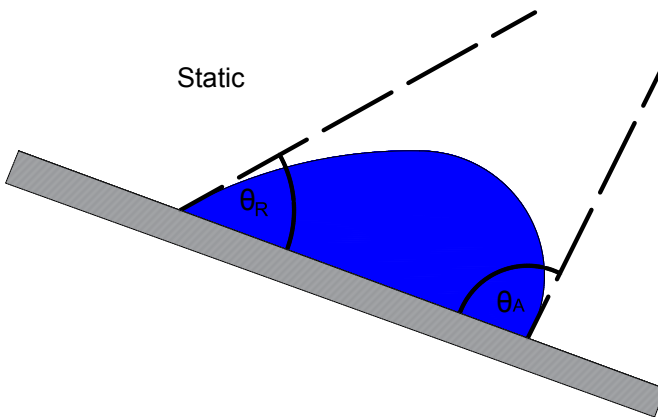


Figure 2.3: Schematic diagram of static contact angle hysteresis. A liquid droplet is originally placed on the surface of a non-ideal solid plate. Inclining one side of the solid plate slowly, because of the gravitational force, the liquid droplet has the tendency to move downwards. The contact angle in front of the droplet is called the advancing contact angle (θ_A) while the contact angle at the back is called the receding contact angle (θ_R). The difference between θ_A and θ_R is called the static contact angle hysteresis when the droplet starts to move relatively to the plate.

2.3. THEORY OF MOVING CONTACT LINE

As mentioned in Section 2.2, due to the small-dimension feature of microfluidic channels, wetting phenomena are important in microfluidic liquid-liquid solvent extraction. Different from the example of a liquid droplet in ambient gas in Section 2.2, for the liquid-liquid multiphase flow inside a microfluidic channel, the contact line is made up of two immiscible liquid phases and one solid phase. In most cases³, the theoretical basis of the moving contact line of both cases is the same.

Recalling in Section 2.2.2, due to the movement of the contact line, there is a deviation between θ_e , θ_m and θ_{app} . Finding the relationship between θ_e , θ_m and θ_{app} is challenging because the physical mechanisms behind the *Moving Contact Line* are still not completely understood. The difficulty of understanding the *Moving Contact Line* is due to the fact that it involves physical processes at different length scales [10]. This section introduces the theory of the *Moving Contact Line* from the hydrodynamic point of view as well as from the molecular-kinetic point of view.

³As an exception, the Voinov-Cox law (will be introduced later) can match the result of a gas-liquid interface while it can not match the result of a liquid-liquid interface [15].

2.3.1. HYDRODYNAMIC THEORY

Under the framework of hydrodynamic theory, the fluid is regarded as a continuum. For incompressible flows, mass conservation is described by the continuity equation (Equation 2.2) while momentum is described by the Navier-Stokes momentum equations (Equation 2.3). Usually, a no-slip boundary condition is imposed on the solid wall for the velocity of the flow, *i.e.*, the fluid velocity at the solid wall is equal to the velocity of the solid wall. *Huh & Scriven* investigated the velocity of the contact line under Stokes flow ($Re << 1$). They found that by imposing the no-slip boundary condition on the wall, the stresses and viscous dissipation became infinite at the contact line. From a mathematical point of view, the no-slip boundary condition brought a singularity to the moving contact line [16]. It is obvious that the no-slip boundary condition therefore cannot be used for moving contact lines.

The Voinov-Cox law therefore aims to use an *ad hoc* slip length at the microscopic scale where the hydrodynamic theory breaks down [17][18][19]. Based on the Voinov-Cox law, the relationship between the apparent contact angle (θ_{app}) and the microscopic dynamic contact angle (θ_m) can be expressed as:

$$C(\theta_{app}) = C(\theta_m) + Ca \ln(L/L_m), \quad (2.9)$$

where C is a complicated but known function which is related to the dynamic viscosity ratio of the fluids [9]. L is the characteristic macroscopic length of the system. L_m is the *ad hoc* slip length which is at the microscopic scale. According to the hydrodynamic theory, the deviation between the apparent contact angle (θ_{app}) and the microscopic dynamic contact angle (θ_m) is attributed to the viscous bending of the interface, which explains the appearance of the Ca number in Equation 2.9.

The Voinov-Cox law assumes that the microscopic dynamic contact angle (θ_m) equals to the equilibrium contact angle (θ_e)⁴. Thus, Equation 2.9 can be written as:

$$C(\theta_{app}) = C(\theta_e) + Ca \ln(L/L_m). \quad (2.10)$$

Even though the Voinov-Cox law can match the experimental results of a gas-liquid interface very well [8] [9], some researchers reported that the Voinov-Cox law can not match the experimental results of a liquid-liquid interface [15].

2.3.2. MOLECULAR-KINETIC THEORY

The interpretation of the moving contact line according to the molecular-kinetic theory is different from that based on the hydrodynamic theory. In the molecular-kinetic theory, the fluid is not regarded as a continuum anymore. Instead, fluids are considered as separate molecules. The movement of the contact line is because of the thermally activated molecules jumping from one fluid phase to the other when the system is out of

⁴Some research indicates that the microscopic dynamic contact angle (θ_m) cannot be taken as the equilibrium contact angle (θ_e). In that case, the microscopic dynamic contact angle (θ_m) is velocity-dependent [20].

equilibria under external driving forces (F) [9] [10] [21].

In the molecular-kinetic theory, molecules need to jump through an energy barrier to get access to one other phase. At equilibrium, the frequency of the energy barrier (E^*) is crossed can be expressed as:

$$\kappa = \kappa_0 \exp\left(\frac{-E^*}{k_B T}\right), \quad (2.11)$$

where κ_0 is the attempt frequency, k_B is the Boltzmann constant, and T is the absolute temperature.

If the equilibrium state is distorted by an external force (F), then the velocity of the three-phase contact line is:

$$U_{cl} = \zeta(\kappa_+ - \kappa_-), \quad (2.12)$$

where ζ is the average distance of each jump. $(\kappa_+ - \kappa_-)$ is the net frequency of the forward and back jumps. κ_+ and κ_- can be expressed as:

$$\kappa_{\pm} = \kappa_0 \exp\left(\frac{-E^* \pm F\zeta/2}{k_B T}\right). \quad (2.13)$$

For the moving contact line, when the apparent contact angle (θ_{app}) deviates from the equilibrium contact angle (θ_e), the driving force is the unbalanced Young's force ($F = \sigma\zeta(\theta_e - \theta_{app})$). Thus, combining Equation 2.12 and Equation 2.13, the velocity of the moving contact line can be expressed as:

$$U_{cl} = 2\zeta\kappa_0 \exp\left(\frac{-E^*}{k_B T}\right) \sinh\left[\frac{\sigma\zeta^2(\theta_e - \theta_{app})}{2k_B T}\right]. \quad (2.14)$$

The molecular-kinetic theory provides a point of view that the moving contact line can be explained by the interactions of molecules within the interface. Such a proposition has been adopted in the Phase Field method, which will be introduced in Section 2.5.

2.4. NUMERICAL MODELLING OF MICROFLUIDIC MULTIPHASE FLOW

Numerical modelling can help to understand and reveal the physical mechanism of multiphase flows. Since parallel flow or segmented flow may occur in microfluidic channels, the modelling method is required to capture the physics behind the *Interface Breakup* and the *Moving Contact Line*. For simulating multiphase flows inside a microfluidic channel, several modelling methods are available. Based on the length scale, these methods can be divided into atomistic level methods and continuum level methods [22].

Concerning the atomistic methods, fluid dynamics is investigated at the fundamental level of atoms or molecules. Different from solving the Navier-Stokes momentum equations and the continuity equation in the continuum approach, atomistic methods (e.g.,

molecular dynamics and direct Monte Carlo simulation) solve the equations of statistical mechanics numerically [23]. However, such kinds of simulations are computationally unaffordable for multiphase flows in microfluidics.

Continuum methods capture the behaviour of the moving contact line and interface breakup by solving the Navier-Stokes momentum equations and the continuity equation numerically. According to the type of meshing, these methods can be categorized into moving-mesh methods and fixed-mesh methods. Since the moving-mesh methods cannot handle the interface breakup problem very well [22], the thesis only focuses on fixed-mesh methods.

Within the category of fixed-mesh methods, Volume-of-Fluid methods [24] [25][26] [27], Level-Set methods [28] [29] [30] [31] and Front-Tracking methods [32] [33] are all reported to be used for simulating the *Moving Contact Line*. Even though these methods utilize different approaches (volume fraction or sign function or connected markers) to distinguish two phases, the interface evolution is governed by the advection equation. Furthermore, when dealing with the incompatibility of the no-slip boundary condition with the moving contact line, these methods all introduce a slip length at the solid surface. However, the physical slip length is at the nanometer scale, which is still much smaller than the finest mesh in microfluidics. Thus, the real physics at the boundary is not solved and the results would be mesh-dependent, unless special treatments are involved [22].

2.5. PHASE FIELD METHOD

The Phase Field method belongs to the fixed-mesh methods and it describes multiphase flows by introducing a diffusive interface with a finite thickness. Within the diffusive interface, the physical properties of the fluids can change continuously. Concerning the *Moving Contact Line*, the Phase Field method is compatible with the no-slip boundary condition in continuum fluid dynamics and no special treatments are required. The mathematical singularity at the wall is removed by the diffusive transport within the finite interface. Furthermore, the diffusive interface is not only a numerical treatment but also has physical meanings. The following sections introduce the governing equations of the Phase Field method in detail as well as their physical meanings.

2.5.1. PHASE FIELD METHOD AND CAHN-HILLIARD EQUATION

In the Phase Field method, the variable that distinguishes different states of matters, like density and viscosity, is called "order parameter (ϕ)" [34]. The Phase Field method is not only limited to describe the interface evolution of fluids. It is also widely used in material science, including solidification, grain growth and crack propagation [35]. Actually, the Phase Field method was first proposed by *Cahn and Hilliard* to investigate the phase separation of alloys [36][37].

Considering a system which contains an aqueous fluid and an immiscible organic fluid,

in the Phase Field method, these two fluids can be described by the order parameter (ϕ). The bulk phase of the aqueous phase and the organic phase are represented with $\phi_{aq} = 1$ and $\phi_{org} = -1$, respectively. As for the interface, there is a smooth and steep transition of the value of ϕ .

2

The Phase Field method is based on a properly defined free energy of the system [38]. For the *Moving Contact Line*, besides the fluid-fluid interaction, it is also necessary to take the interaction between the fluids and the wall into account. Thus, the free energy (E_{free}) of the whole system can be expressed as the sum of the mixing energy between two fluids (E_{mix}) and the wall surface free energy (E_{wall}) which represents the fluid-fluid-wall interaction:

$$E_{free} = E_{mix} + E_{wall} = \int_{\Omega} f_{mix}(\phi, \nabla\phi) d\Omega + \int_{\Gamma} f_w(\phi) d\Gamma, \quad (2.15)$$

Ω is the volume of the domain to be integrated and Γ represents the wall surface to be integrated. This section mainly discusses the mixing energy (E_{mix}). The wall surface free energy (E_{wall}) is related to boundary conditions, which will be discussed in Section 2.5.3.

Even though called "immiscible", the fluids still mix to some extent at the interface. Under the diffusive-interface framework in the Phase Field method, the two fluids mix at the interface and store the mixing energy (E_{mix}). f_{mix} is the mixing energy density (SI unit: J/m³) which is a function of the order parameter and its gradient [35]. Applying the Ginzburg–Landau free energy form for the mixing energy density, the mathematical expression for the mixing energy density is illustrated in Equation 2.16:

$$f_{mix}(\phi, \nabla\phi) = \frac{1}{2} \lambda |\nabla\phi|^2 + \frac{\lambda}{4\epsilon^2} (\phi^2 - 1)^2, \quad \lambda = \frac{3\sigma\epsilon}{2\sqrt{2}}, \quad (2.16)$$

λ (SI unit: N) is the mixing energy density parameter, ϵ (SI unit: m) is the capillary width which determines the interfacial thickness [38].

The mixing energy density (f_{mix}) can be divided into two parts: the first term on the right-hand side of Equation 2.16 represents the mixing energy in the bulk and the second term represents the mixing energy resided at the interface. Van der Waals hypothesized that equilibrium interfaces minimize the integral of f_{mix} [39]. For the purpose of reaching the equilibrium state, both terms try to approach their minimum by changing the distribution of the order parameter (ϕ) [40]. The minimum of the first term represents a complete mix of these two phases. It can be regarded as the "attractive effect" between these two phases. On the other hand, the second term is a double-well potential function. The minimum of the second term represents separation of these two phases ($\phi = 1$ or $\phi = -1$). This term is considered as the "repulsive effect" between these two phases. Figure 2.4 illustrates the profile of the double-well potential function of $f(\phi) = \frac{1}{4} (\phi^2 - 1)^2$ (leaving out λ and ϵ of the second term in Equation 2.16.).

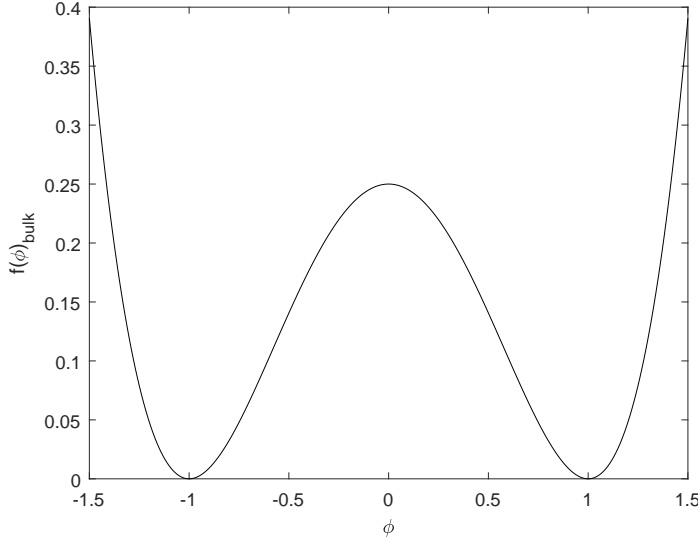


Figure 2.4: The double-well potential function $f(\phi) = \frac{1}{4}(\phi^2 - 1)^2$.

According to *Cahn and Hilliard* [36][37], a generalized chemical potential (G) of the system quantifies how much the free energy changes when the distribution of the order parameter (ϕ) changes. The generalized chemical potential (G) can be obtained by taking the variation of the mixing energy (E_{mix}) with respect to the order parameter (ϕ):

$$G = \frac{\delta \int_{\Omega} f_{mix} d\Omega}{\delta \phi} = \frac{\int_{\Omega} (\frac{\partial f_{mix}}{\partial \phi} - \nabla \frac{\partial f_{mix}}{\partial (\nabla \phi)}) \delta \phi d\Omega}{\delta \phi} = \lambda \left[\frac{\phi(\phi^2 - 1)}{\epsilon^2} - \nabla^2 \phi \right]. \quad (2.17)$$

At equilibrium, the distribution of the order parameter (ϕ) stops changing. Thus, the generalized chemical potential (G) becomes zero:

$$G = \lambda \left[-\nabla^2 \phi + \frac{\phi(\phi^2 - 1)}{\epsilon^2} \right] = 0. \quad (2.18)$$

In the one-dimensional case:

$$G = \lambda \left[-\frac{d^2 \phi}{dx^2} + \frac{\phi(\phi^2 - 1)}{\epsilon^2} \right] = 0. \quad (2.19)$$

Imposing the boundary condition of $\phi_{(x=0)} = 0$, Equation 2.19 can be solved [38]:

$$\phi_{(x)} = \tanh\left(\frac{x}{\sqrt{2}\epsilon}\right). \quad (2.20)$$

Equation 2.20 shows that for the one-dimensional case, at equilibrium, the profile of ϕ is a hyperbolic tangent function. The capillary width (ϵ) controls the thickness of the in-

terface.

To further demonstrate the relationship between the capillary width (ϵ) and the interfacial thickness (Equation 2.20), Figure 2.5 presents the hyperbolic tangent function with different capillary width (ϵ) with a one-dimensional domain with characteristic length of $100 \mu m$. In the profile, $\phi = 1$ and $\phi = -1$ indicate the two bulk phases while $-1 < \phi < 1$ indicates the interface. As ϵ increases, the interface becomes "thicker".

Two things to note in Figure 2.5: first, the value of ϵ does not equal the interfacial thickness in the Phase Field method. According to *Yue et al.*, 90 percent of the variation in ϕ occurs over a thickness of 4.1641ϵ , while 99 percent of the variation corresponds to a thickness of 7.4859ϵ [38]. Second, the interfacial thickness in the Phase Field method is usually much larger than the actual physical thickness. The typical interfacial thickness of a liquid–liquid interface is a few nanometers [41]. Enlarging the interfacial thickness in the Phase Field method is for the sake of saving computational effort when solving it numerically.

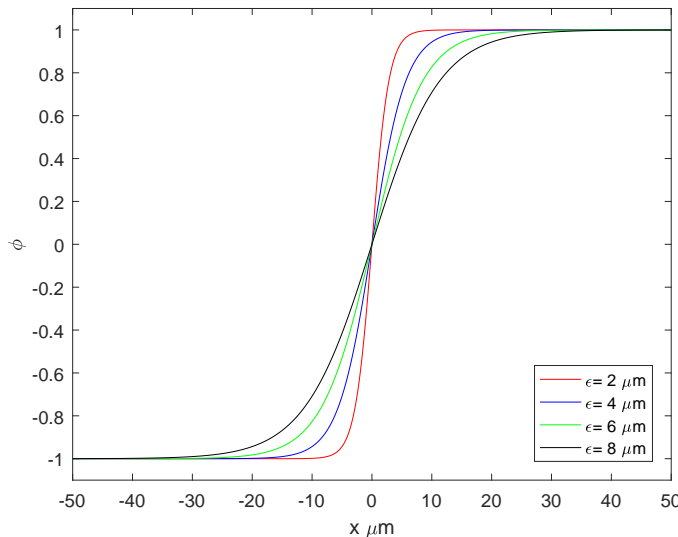


Figure 2.5: The profile of ϕ at equilibrium in a one dimensional domain. The characteristic length of the domain is $100 \mu m$. The capillary width (ϵ) are $2 \mu m$, $4 \mu m$, $6 \mu m$ and $8 \mu m$. $\phi = 1$ and $\phi = -1$ indicate the two bulk phases while $-1 < \phi < 1$ indicates the interface.

In the dynamic process, similar to Fick's Law, the interfacial diffusive flux (\mathbf{j}) of the order parameter (ϕ) is proportional to the gradient of the chemical potential [36][37]:

$$\mathbf{j} = -M \nabla G. \quad (2.21)$$

In Equation 2.21, M (SI unit: $\text{m}^3\text{s}/\text{kg}$) is called the mobility parameter which is analogous to the diffusion coefficient in mass transfer by diffusion.

Because of the conservation of the order parameter (ϕ), the continuity equation of ϕ is:

$$\frac{\partial \phi}{\partial t} + \nabla \cdot \mathbf{j} = 0, \quad (2.22)$$

where t denotes time.

The governing equation for the total transport of ϕ can be derived by combining Equation 2.21 with Equation 2.22 and adding a convective term. This is the Cahn–Hilliard equation⁵:

$$\frac{\partial \phi}{\partial t} + \mathbf{u} \cdot \nabla \phi = M \nabla^2 G, \quad (2.23)$$

where \mathbf{u} represents the velocity field.

The diffusive interface in the Phase Field method is physically meaningful. The theory of the Phase Field method originates from Van der Waals's insight of interfaces. He proposed that there was a diffusive interface with finite thickness between phases, rather than a sharp interface where there was a discontinuity of the properties of phases [43]. Moreover, the physical meaning of the Phase Field method not only locates in the diffusive interface but also in bulk phases. The "attractive effect" and "repulsive effect" account for long range van der Walls forces between atoms and molecules [44].

The Phase Field method also tries to integrate the explanation of multiphase flows under one framework. On one hand, fluid particles interaction within the diffusive interface represents the explanation based on the molecular-kinetic theory. On the other hand, the macroscopic flow can be described by hydrodynamic equations, which agrees with the continuum theory [44]. Section 2.5.2 introduces how the macroscopic flow is described in the Phase Field method.

2.5.2. COUPLING CAHN–HILLIARD EQUATION WITH NAVIER–STOKES EQUATIONS

When describing multiphase flows in microfluidic channels, the Cahn–Hilliard equation needs to be coupled with the Navier–Stokes momentum equations:

$$\rho_{(\phi)} \frac{\partial \mathbf{u}}{\partial t} + \rho_{(\phi)} (\mathbf{u} \cdot \nabla) \mathbf{u} = -\nabla P + \mu_{(\phi)} \nabla^2 \mathbf{u} + \mathbf{F}_{it}, \quad (2.24)$$

where \mathbf{F}_{it} is the interfacial tension force. The gravitational force term is left out due to the low Bo number of the microfluidic system, as discussed in Section 2.1.3.

⁵In the Phase Field method, there is an other equation called "Allen–Cahn equation", which can be regarded as a simplified version of the Cahn–Hilliard equation [42]. Deriving the Allen–Cahn equation is out of the scope of this thesis.

In Equation 2.24, both the density $\rho_{(\phi)}$ and the dynamic viscosity $\mu_{(\phi)}$ are functions of the order parameter ϕ ($\phi \in [-1, 1]$):

$$\rho_{(\phi)} = \frac{\rho_{aq}(1+\phi)}{2} + \frac{\rho_{org}(1-\phi)}{2}, \mu_{(\phi)} = \frac{\mu_{aq}(1+\phi)}{2} + \frac{\mu_{org}(1-\phi)}{2}, \quad (2.25)$$

2

where the notation *aq* and *org* represent the aqueous phase and the organic phase, respectively.

In Equation 2.25, physical properties of bulk phases are expressed with $\phi = 1$ and $\phi = -1$, respectively. As demonstrated in Figure 2.5, the value of ϕ changes steeply and continuously inside the diffusive interface. Since both the density and the dynamic viscosity are related to the order parameter ϕ , the physical properties change within the interface with respect to ϕ as well.

In order to describe two-phase flows at the micro-scale, the interfacial tension force plays an important role [22]. When coupling the Phase Field Method with the Navier-Stokes equations, more than one expression for the interfacial tension force can be found in literature [45]. In this research, the model for the interfacial tension force is adopted from the expression proposed by *Jacqmin* [39][46][47]. The model derives from an energy approach. To derive the interfacial tension force from the energy approach, according to *Jacqmin*, there are three key ideas: (1) convection can change the amount of free energy by either lengthening or thickening/ thinning interfaces, (2) there must be a diffuse-interface force exerted by the fluid such that the change in kinetic energy is always opposite to the change in free energy, (3) this must be true for arbitrary interface configurations and (compressible) velocity fields [46].

Based on *Jacqmin's* work, the total energy includes the kinetic energy ($E_{kinetic}$) and the free energy (E_{free}). The rate of change of the total energy can be expressed as:

$$\frac{\partial E_{total}}{\partial t} = \int_{\Omega} \left(\frac{\partial^2 \frac{1}{2} \phi |\mathbf{u}|^2}{\partial t} + \sum_{i=1}^3 \lambda \frac{\partial \phi}{\partial x_i} \frac{\partial}{\partial t} \frac{\partial \phi}{\partial x_i} + \frac{\lambda \phi (\phi^2 - 1)}{\epsilon^2} \frac{\partial \phi}{\partial t} \right) d\Omega + \int_{\Gamma} f'_w(\phi) \frac{\partial \phi}{\partial t} d\Gamma, \quad (2.26)$$

where E_{total} is the total energy of the system.

Integration by parts of the term $\int_{\Omega} \left(\sum_{i=1}^3 \lambda \frac{\partial \phi}{\partial x_i} \frac{\partial}{\partial t} \frac{\partial \phi}{\partial x_i} \right) d\Omega$ and combining with Equation 2.17:

$$\frac{\partial E_{total}}{\partial t} = \int_{\Omega} \left(\frac{\partial^2 \frac{1}{2} \phi |\mathbf{u}|^2}{\partial t} + G \frac{\partial \phi}{\partial t} \right) d\Omega + \int_{\Gamma} \lambda \frac{\partial \phi}{\partial x_n} \frac{\partial \phi}{\partial t} d\Gamma + \int_{\Gamma} f'_w(\phi) \frac{\partial \phi}{\partial t} d\Gamma, \quad (2.27)$$

where x_n represents the direction normal to the wall.

The last two terms in Equation 2.27 are the wall surface integrals of the whole system, which serve as boundary conditions and are left out in Equation 2.28. The boundary

conditions for the Phase Field method will be introduced in Section 2.5.3.

Without the surface integral terms, Equation 2.27 becomes:

$$\frac{\partial E_{total}}{\partial t} = \int_{\Omega} \left(\frac{\partial^{\frac{1}{2}} \phi |\mathbf{u}|^2}{\partial t} + G \frac{\partial \phi}{\partial t} \right) d\Omega. \quad (2.28)$$

The convective transport of ϕ is:

$$\frac{\partial \phi}{\partial t} + \mathbf{u} \cdot \nabla \phi = 0. \quad (2.29)$$

Thus, replacing $\frac{\partial \phi}{\partial t}$ with $-\mathbf{u} \cdot \nabla \phi$, Equation 2.28 can be rewritten as:

$$\frac{\partial E_{total}}{\partial t} = \int_{\Omega} \left(\frac{\partial^{\frac{1}{2}} \phi |\mathbf{u}|^2}{\partial t} - G \sum_{i=1}^3 u_i \frac{\partial \phi}{\partial x_i} \right) d\Omega. \quad (2.30)$$

The rate of change of the kinetic energy ($E_{kinetic}$) due to interfacial tension forces can be expressed as: $\int_{\Omega} (\sum_{i=1}^3 u_i F_i) d\Omega$. According to Jacqmin's hypothesis that the change in kinetic energy ($E_{kinetic}$) is always opposite to the change in free energy (E_{free}) by the interfacial tension force, the rate of change of the total energy (E_{total}) should always be zero:

$$\frac{\partial E_{total}}{\partial t} = \int_{\Omega} \left(\sum_{i=1}^3 u_i F_i - G \sum_{i=1}^3 u_i \frac{\partial \phi}{\partial x_i} \right) d\Omega = 0. \quad (2.31)$$

Thus, the interfacial tension force can be expressed as:

$$\mathbf{F}_{it} = G \nabla \phi. \quad (2.32)$$

2.5.3. BOUNDARY CONDITIONS FOR THE PHASE FIELD METHOD

The continuity equation (Equation 2.2), the coupled Navier-Stokes momentum equations (Equation 2.24) and the Cahn-Hilliard equation (Equation 2.23) are the governing equations to describe multiphase flows in microfluidics. To solve these partial differential equations, it is necessary to impose proper boundary conditions.

At the inlets, the velocity of the fluids is prescribed. At the outlets, a reference pressure (Pressure = 0 Pa) is defined. At the solid walls, for the velocity field, a no-slip boundary condition is imposed since the mathematical singularity mentioned by Huh & Scriven can be removed by the diffusive movement of the order parameter within the interface. In addition, the no-flux boundary condition for the chemical potential (G) is chosen on the wall:

$$\frac{\partial G}{\partial x_n} = 0, \quad (2.33)$$

where x_n represents the direction normal to the wall.

Besides the above-mentioned boundary conditions, microfluidic multiphase flows require to impose a boundary condition on the wall to reflect the wettability property of the channel wall. The wettability property of the channel wall is characterized by the contact angle formed at the three-phase contact line. In this thesis, the boundary condition used for the contact angle was first proposed by *Jacqmin* [46]. The boundary condition proposed by *Jacqmin* is able to capture the dynamic wetting process. In the following, the derivation of this boundary condition is shown.

In Section 2.2.1, σ_{sg} and σ_{sl} were introduced to describe the free energy of the dry wall (σ_{sg}) and the wet wall (σ_{sl}), separately. The wall surface free energy (E_{wall}) of the system is written as:

$$E_{wall} = \int_{\Gamma} f_w(\phi) d\Gamma = \int_{\Gamma} (\sigma_{sg} + (\sigma_{sl} - \sigma_{sg}) g(\phi)) d\Gamma, \quad (2.34)$$

where $g(\phi) = \frac{-\phi^3 + 3\phi + 2}{4}$. $g(\phi)$ is a higher order polynomial of ϕ which acts as a switch between the immiscible two phases [48]. Notice that $g(1) = 1$ and $g(-1) = 0$, which reflects the free energy of the wet wall and the dry wall, respectively.

Substituting Young's law (Equation 2.8) into Equation 2.34, we get:

$$\int_{\Gamma} f_w(\phi) d\Gamma = \int_{\Gamma} (\sigma_{sg} - \sigma \cos(\theta_e) g(\phi)) d\Gamma. \quad (2.35)$$

According to *Jacqmin* [46][47][39], at equilibrium, the surface integral of the free energy is zero. Thus, the last two terms of Equation 2.27 can be rewritten as:

$$\int_{\Gamma} \left(\lambda \frac{\partial \phi}{\partial x_n} + f'_w(\phi) \right) \frac{\partial \phi}{\partial t} d\Gamma = 0. \quad (2.36)$$

Hence:

$$\lambda \frac{\partial \phi}{\partial x_n} + f'_w(\phi) = 0. \quad (2.37)$$

As for the dynamic process, the surface integral of the free energy is not zero anymore. *Jacqmin* introduced a new coefficient (D_w) to involve the effect of the non-equilibrium contact angle on the wall:

$$\frac{\partial \phi}{\partial t} + \mathbf{u} \cdot \nabla \phi = D_w \left(\lambda \frac{\partial \phi}{\partial x_n} + f'_w(\phi) \right). \quad (2.38)$$

During the dynamic process, Equation 2.38 allows for the apparent contact angle (θ_{app}) deviating from the equilibrium contact angle (θ_e). One thing to note here: Equation 2.38 adopts the assumption that the microscopic dynamic contact angle (θ_m) equals the equilibrium contact angle (θ_e), which has already been discussed in Section 2.3.1.

After *Jacqmin*, *Yue et al.* [44] [49] [50] and *Carlson et al.* [51] [52] further explored the boundary condition in Equation 2.38, separately. Both *Yue et al.* and *Carlson et al.* reorganized Equation 2.38 with their different insights of the non-equilibrium contact angle

boundary condition. This work adopts *Carlson et al.*'s expression of the non-equilibrium contact angle boundary condition.

In *Carlson et al.*'s work, the non-equilibrium contact angle boundary condition is written as⁶:

$$-\epsilon\mu_f \frac{\partial\phi}{\partial t} = \lambda \frac{\partial\phi}{\partial x_n} + f_w'(\phi). \quad (2.39)$$

The coefficient D_w has been moved to the left-hand side of the equation and replaced by $-\epsilon\mu_f$. ϵ is the capillary width which has been introduced in Equation 2.16. μ_f (SI unit: Pa·s) is a positive constant and *Carlson et al.* explains it as a contact line friction parameter [51].

2.5.4. DIMENSIONLESS FORMULATION OF THE GOVERNING EQUATIONS

The continuity equation (Equation 2.2), the coupled Navier-Stokes momentum equations (Equation 2.24) and the Cahn-Hilliard equation (Equation 2.23) are the governing equations to describe multiphase flows in microfluidics.

In the dimensionless formulation of the governing equations, the width of the channel L is chosen as the characteristic length. U_{aq} is the characteristic velocity of the fluid which takes the average velocity of the aqueous phase at the inlet of the microfluidic channel. The dimensionless variables (the symbols with overlines) are expressed as:

$$\bar{\mathbf{x}} = \frac{\mathbf{x}}{L}, \bar{\mathbf{u}} = \frac{\mathbf{u}}{U_{aq}}, \bar{t} = \frac{t U_{aq}}{L}, \bar{P} = \frac{PL}{\mu_{aq} U_{aq}}, \bar{\rho}_{(\phi)} = \frac{\rho_{(\phi)}}{\rho_{aq}}, \bar{\mu}_{(\phi)} = \frac{\mu_{(\phi)}}{\mu_{aq}}, \bar{\nabla} = L \nabla, \quad (2.40)$$

where ρ_{aq} is the density of the aqueous phase and μ_{aq} is the dynamic viscosity of the aqueous phase.

Then, the continuity equation (Equation 2.2), the coupled Navier-Stokes momentum equations (Equation 2.24) and the Cahn-Hilliard equation (Equation 2.23) are non-dimensionalized as follows:

The non-dimensionalized continuity equation:

$$\bar{\nabla} \cdot \bar{\mathbf{u}} = 0. \quad (2.41)$$

The non-dimensionalized Navier-Stokes momentum equations:

$$Re \bar{\rho}_{(\phi)} \left[\frac{\partial \bar{\mathbf{u}}}{\partial \bar{t}} + (\bar{\mathbf{u}} \cdot \bar{\nabla}) \bar{\mathbf{u}} \right] = -\bar{\nabla} \bar{P} + \bar{\mu}_{(\phi)} \bar{\nabla}^2 \bar{\mathbf{u}} + \bar{\mathbf{F}}_{it}. \quad (2.42)$$

⁶The $\mathbf{u} \cdot \nabla \phi$ term has been left out due to the no-slip boundary condition at the wall. There is research investigating both the slip velocity boundary condition and the diffusive interfacial transport that keeps this term [53].

$$\bar{\mathbf{F}}_{\text{it}} = \frac{3}{2\sqrt{2}} \frac{1}{CnCa} \left[-Cn^2 \bar{\nabla}^2 \phi + (\phi^2 - 1) \phi \right] \nabla \phi. \quad (2.43)$$

2

The non-dimensionalized Cahn-Hilliard equation:

$$\frac{\partial \phi}{\partial t} + \bar{\mathbf{u}} \cdot \bar{\nabla} \phi = \frac{3}{2\sqrt{2}} \frac{1}{Pe} \bar{\nabla}^2 \left[-Cn^2 \bar{\nabla}^2 \phi + (\phi^2 - 1) \phi \right]. \quad (2.44)$$

$$Re = \frac{\rho_{aq} U_{aq} L}{\mu_{aq}}, \quad Ca = \frac{\mu_{aq} U_{aq}}{\sigma}, \quad Cn = \frac{\epsilon}{L}, \quad Pe = \frac{2\sqrt{2} U_{aq} L \epsilon}{3M\sigma}. \quad (2.45)$$

These are the four dimensionless numbers appearing in the equations system after non-dimensionalization. The *Reynolds* number (*Re*) is the ratio between inertia force and viscous force. The *Capillary* number (*Ca*) describes the ratio between viscous force and interfacial tension force. The *Cahn* number (*Cn*) describes the ratio between the prescribed interfacial thickness and the characteristic length. The *Péclet* (*Pe*) number is the ratio of the convective transport to the diffusive transport of the order parameter. These dimensionless numbers can be derived for both the aqueous and organic phases, indicated by subscripts.

In addition, with the same dimensionless variables, the non-equilibrium contact angle boundary condition (Equation 2.39) can be non-dimensionalized as ($\lambda = \frac{3\sigma\epsilon}{2\sqrt{2}}$ based on Equation 2.16):

$$-\frac{\mu_f U_{aq}}{\sigma} \frac{\partial \phi}{\partial t} = \frac{3}{2\sqrt{2}} \frac{\partial \phi}{\partial \bar{x}_n} + f'_w(\phi) \frac{L}{\epsilon\sigma}. \quad (2.46)$$

The $\frac{\mu_f U_{aq}}{\sigma}$ on the left-hand side of Equation 2.46 is defined as the *Ca_f* number for the contact line friction parameter. The *Ca_f* number can be also derived based on the organic phase.

2.6. COMSOL MULTIPHYSICS AND FINITE ELEMENT METHOD

In this work, the behaviour of multiphase flows inside a microfluidic channel is governed by the continuity equation (Equation 2.2), the Cahn-Hilliard equation (Equation 2.23) and the Navier-Stokes momentum equations (Equation 2.24). All of them are partial differential equations (PDEs). Usually, only a few PDEs with simple and symmetric geometry can be solved analytically. These coupled PDEs to describe multiphase flows in microfluidic channels cannot be solved analytically. Thus, the approximate solutions of these PDEs are solved numerically by COMSOL Multiphysics (short for COMSOL) with the Finite Element Method. Even though the Finite Element Method is not the best method to solve fluid problems with turbulence, it is a good choice for microfluidics

with low Re number [1]. This section briefly introduces the Finite Element Method.

In general, a partial differential equation can be written as Equation 2.47, where $v(\mathbf{x}, t)$ is the dependent variable, like velocity, temperature or concentration. The dependent variable is a function of independent variables, like space (\mathbf{x}) and time (t). ξ is the differential operator of $v(\mathbf{x}, t)$. $f(\mathbf{x}, t)$ is the source term or forcing term.

$$\xi v(\mathbf{x}, t) = f(\mathbf{x}, t) \quad \text{in } \Omega. \quad (2.47)$$

The domain Ω is divided into finite sub-domains by meshing. Since most of the time, the function $v(\mathbf{x}, t)$ is hard to solve analytically, it is necessary to seek for an approximate solution function $v_h(\mathbf{x}, t)$ which is the sum of several basis functions η_i . The basis function η_i has a value of zero or one on each node and v_i is the coefficient to glue the basis functions.

$$v(\mathbf{x}, t) \approx v_h(\mathbf{x}, t); \quad v_h(\mathbf{x}, t) = \sum_i v_i \eta_i. \quad (2.48)$$

The Finite Element Method determines the approximate solution function by virtue of the weak formulation of the PDE. As an example, the process of finding the approximate solution function is introduced by solving a Poisson equation. Equation 2.49 is the Poisson equation where f is a known function. The domain Ω has two boundaries: Γ_1 and Γ_2 . A Dirichlet boundary condition is imposed on Γ_1 and a Neumann boundary condition is imposed on Γ_2 .

$$-\nabla^2 v = f \quad \text{in } \Omega. \quad (2.49)$$

$$v = \text{constant} \quad \text{on } \Gamma_1. \quad (2.50)$$

$$\frac{\partial v}{\partial n} = 0 \quad \text{on } \Gamma_2. \quad (2.51)$$

In Equation 2.49, both sides are multiplied with a test function η and integrated over the domain Ω .

$$\int_{\Omega} -\nabla^2 v \eta d\Omega = \int_{\Omega} f \eta d\Omega. \quad (2.52)$$

Applying Green's first identity, Equation 2.52 can be written as:

$$\int_{\Omega} \nabla v \cdot \nabla \eta d\Omega + \int_{\Gamma} (-\nabla v) \cdot \mathbf{n} \eta d\Gamma = \int_{\Omega} f \eta d\Omega. \quad (2.53)$$

The prerequisite for applying Green's first identity is that v has continuous second order derivatives. Equation 2.53 is the weak formulation of Equation 2.52. It changes the second order derivative of v into its first order derivative. In addition, the surface integral appears in the second term of the left-hand side of the equation, which is related to boundary conditions. [54]

The next step is discretization. In COMSOL, the Galerkin method is used for discretizing the mathematical problem into the numerical problem. Based on Equation 2.48, function v approximately equals to v_h which is made up of a series of basis functions η_i . In addition, the test function η is also expressed in the discretized form:

2

$$\sum_i v_i \int_{\Omega} \nabla \eta_i \cdot \nabla \eta_j d\Omega + \sum_i \int_{\Gamma} (-v_i \nabla \eta_i) \cdot \mathbf{n} \eta_j d\Gamma = \int_{\Omega} f \left(\sum_i v_i \eta_i \right) \eta_j d\Omega. \quad (2.54)$$

In Equation 2.54, v_i are the unknown coefficients. If the number of test functions η_i is n, then Equation 2.54 can be written as a matrix:

$$\mathbf{A}\mathbf{T} = \mathbf{B}, \quad (2.55)$$

where \mathbf{T} is the vector of unknowns, \mathbf{A} is the system matrix and \mathbf{B} is the load vector which is known. Thus, the problem of solving a PDE has become solving a matrix.

One other thing to mention is that, in COMSOL, the Cahn–Hilliard equation is solved by splitting the original form with a fourth-order operator into two second-order partial differential equations with introducing an auxiliary variable Ψ . The split version of the equations are [55]:

$$\frac{\partial \phi}{\partial t} + \mathbf{u} \cdot \nabla \phi = \nabla \cdot \frac{M\lambda}{\epsilon^2} \nabla \Psi. \quad (2.56)$$

$$\Psi = -\nabla \cdot \epsilon^2 \nabla \phi + (\phi^2 - 1) \phi. \quad (2.57)$$

REFERENCES

- [1] Henrik Bruus. *Theoretical microfluidics*. Oxford : Oxford Univ. Press, 2008., 2008.
- [2] R. Mudde Harrie van den Akker. *Transport Phenomena - The Art of Balancing*. Delft Academic Press, 2014.
- [3] Lingling Shui, Jan C.T. Eijkel, and Albert van den Berg. Multiphase flow in microfluidic systems – control and applications of droplets and interfaces. *Advances in Colloid and Interface Science*, 133(1):35 – 49, 2007.
- [4] Anne-Laure Dessimoz, Laurent Cavin, Albert Renken, and Lioubov Kiwi-Minsker. Liquid–liquid two-phase flow patterns and mass transfer characteristics in rectangular glass microreactors. *Chemical Engineering Science*, 63(16):4035 – 4044, 2008.
- [5] Arata Aota, Kazuma Mawatari, and Takehiko Kitamori. Parallel multiphase microflows: fundamental physics, stabilization methods and applications. *Lab Chip*, 9:2470–2476, 2009.
- [6] Yuchao Zhao, Guangwen Chen, and Quan Yuan. Liquid-liquid two-phase flow patterns in a rectangular microchannel. *AIChE Journal*, 52(12):4052–4060, 2006.
- [7] Ping Cheng, Hui-Ying Wu, and Fang-Jun Hong. Phase-change heat transfer in microsystems. *Journal of Heat Transfer*, 129:101–108, 2006.
- [8] Daniel Bonn, Jens Eggers, Joseph Indekeu, Jacques Meunier, and Etienne Rolley. Wetting and spreading. *Rev. Mod. Phys.*, 81:739–805, May 2009.
- [9] Terence D. Blake. The physics of moving wetting lines. *Journal of Colloid and Interface Science*, 299(1):1 – 13, 2006.
- [10] Jacco H. Snoeijer and Bruno Andreotti. Moving contact lines: Scales, regimes, and dynamical transitions. *Annual Review of Fluid Mechanics*, 45(1):269–292, 2013.
- [11] Xuan Cai. *Interface-Resolving Simulations of Gas-Liquid Two-Phase Flows in Solid Structures of Different Wettability*. PhD thesis, Karlsruher Institut für Technologie (KIT), 2016.
- [12] H. Yildirim Erbil. The debate on the dependence of apparent contact angles on drop contact area or three-phase contact line: A review. *Surface Science Reports*, 69(4):325 – 365, 2014.
- [13] H. B. Eral, D. J. C. M. 't Mannetje, and J. M. Oh. Contact angle hysteresis: a review of fundamentals and applications. *Colloid and Polymer Science*, 291(2):247–260, Feb 2013.
- [14] Vyas Srinivasan and Sameer Khandekar. Thermo-hydrodynamic transport phenomena in partially wetting liquid plugs moving inside micro-channels. *Sādhanā*, 42(4):607–624, Apr 2017.

- [15] Marc Fermigier and Patrice Jenffer. An experimental investigation of the dynamic contact angle in liquid-liquid systems. *Journal of Colloid and Interface Science*, 146(1):226 – 241, 1991.
- [16] Chun Huh and L.E Scriven. Hydrodynamic model of steady movement of a solid/liquid/fluid contact line. *Journal of Colloid and Interface Science*, 35(1):85 – 101, 1971.
- [17] R. G. Cox. The dynamics of the spreading of liquids on a solid surface. Part 1. viscous flow. *Journal of Fluid Mechanics*, 168:169–194, 1986.
- [18] L H Tanner. The spreading of silicone oil drops on horizontal surfaces. *Journal of Physics D: Applied Physics*, 12(9):1473, 1979.
- [19] O. V. Voinov. Hydrodynamics of wetting. *Fluid Dynamics*, 11(5):714–721, Sep 1976.
- [20] Yi Sui, Hang Ding, and Peter D.M. Spelt. Numerical simulations of flows with moving contact lines. *Annual Review of Fluid Mechanics*, 46(1):97–119, 2014.
- [21] T.D Blake and J.M Haynes. Kinetics of liquid liquid displacement. *Journal of Colloid and Interface Science*, 30(3):421 – 423, 1969.
- [22] Martin Wörner. Numerical modeling of multiphase flows in microfluidics and micro process engineering: a review of methods and applications. *Microfluidics and Nanofluidics*, 12(6):841–886, May 2012.
- [23] Kai Kadau, John L. Barber, Timothy C. Germann, Brad L. Holian, and Berni J. Alder. Atomistic methods in fluid simulation. *Philosophical Transactions of the Royal Society A: Mathematical, Physical and Engineering Sciences*, 368(1916):1547–1560, 2010.
- [24] C. Josserdan, L. Lemoyne, R. Troeger, and S. Zaleski. Droplet impact on a dry surface: triggering the splash with a small obstacle. *Journal of Fluid Mechanics*, 524:47–56, 2005.
- [25] Jean-Baptiste Dupont and Dominique Legendre. Numerical simulation of static and sliding drop with contact angle hysteresis. *J. Comput. Phys.*, 229(7):2453–2478, April 2010.
- [26] Kensuke Yokoi. Numerical studies of droplet splashing on a dry surface: triggering a splash with the dynamic contact angle. *Soft Matter*, 7:5120–5123, 2011.
- [27] Michael Renardy, Yuriko Renardy, and Jie Li. Numerical simulation of moving contact line problems using a volume-of-fluid method. *Journal of Computational Physics*, 171(1):243 – 263, 2001.
- [28] Yuming Chen, Rainer Mertz, and Rudi Kulenovic. Numerical simulation of bubble formation on orifice plates with a moving contact line. *International Journal of Multiphase Flow*, 35(1):66 – 77, 2009.

- [29] Hang Ding and Peter D. M. Spelt. Inertial effects in droplet spreading: a comparison between diffuse-interface and level-set simulations. *Journal of Fluid Mechanics*, 576:287–296, 2007.
- [30] Yi Sui and Peter D. M. Spelt. Validation and modification of asymptotic analysis of slow and rapid droplet spreading by numerical simulation. *Journal of Fluid Mechanics*, 715:283–313, 2013.
- [31] Jun Kwon Park and Kwan Hyoung Kang. Numerical analysis of moving contact line with contact angle hysteresis using feedback deceleration technique. *Physics of Fluids*, 24(4):042105, 2012.
- [32] Metin Muradoglu and Savas Tasoglu. A front-tracking method for computational modeling of impact and spreading of viscous droplets on solid walls. *Computers & Fluids*, 39(4):615 – 625, 2010.
- [33] S. Manservisi and R. Scardovelli. A variational approach to the contact angle dynamics of spreading droplets. *Computers & Fluids*, 38(2):406 – 424, 2009.
- [34] Ingo Steinbach. Phase-field models in materials science. *Modelling and Simulation in Materials Science and Engineering*, 17(7):073001, 2009.
- [35] Long-Qing Chen. Phase-field models for microstructure evolution. *Annual Review of Materials Research*, 32(1):113–140, 2002.
- [36] John W. Cahn and John E. Hilliard. Free energy of a nonuniform system. I. interfacial free energy. *The Journal of Chemical Physics*, 28(2):258–267, 1958.
- [37] John W. Cahn and John E. Hilliard. Free energy of a nonuniform system. III. nucleation in a two-component incompressible fluid. *The Journal of Chemical Physics*, 31(3):688–699, 1959.
- [38] Pengtao Yue, James J. Feng, Chun Liu, and Jie Shen. A diffuse-interface method for simulating two-phase flows of complex fluids. *Journal of Fluid Mechanics*, 515:293–317, 2004.
- [39] David Jacqmin. An energy approach to the continuum surface tension method. In *AIAA 34th Aerospace Sciences Meeting and Exhibit*, 1996.
- [40] Olga Wodo and Baskar Ganapathysubramanian. Computationally efficient solution to the Cahn–Hilliard equation: Adaptive implicit time schemes, mesh sensitivity analysis and the 3D isoperimetric problem. *Journal of Computational Physics*, 230(15):6037 – 6060, 2011.
- [41] Chun Yang and Dongqing Li. A method of determining the thickness of liquid–liquid interfaces. *Colloids and Surfaces A: Physicochemical and Engineering Aspects*, 113(1):51 – 59, 1996.
- [42] D. F. M. Vasconcelos, A. L. Rossa, and A. L. G. A. Coutinho. A residual-based allen–cahn phase field model for the mixture of incompressible fluid flows. *International Journal for Numerical Methods in Fluids*, 75(9):645–667, 2014.

- 2
- [43] J. S. Rowlinson. Translation of J. D. van der Waals' "The thermodynamik theory of capillarity under the hypothesis of a continuous variation of density". *Journal of Statistical Physics*, 20(2):197–200, Feb 1979.
 - [44] P. Yue and J. J. Feng. Can diffuse-interface models quantitatively describe moving contact lines? *The European Physical Journal Special Topics*, 197(1):37, Aug 2011.
 - [45] Junseok Kim. Phase-field models for multi-component fluid flows. *Communications in Computational Physics*, 12(3):613–661, 2012.
 - [46] David Jacqmin. Calculation of two-phase Navier–Stokes flows using phase-field modeling. *Journal of Computational Physics*, 155(1):96 – 127, 1999.
 - [47] David Jacqmin. Contact-line dynamics of a diffuse fluid interface. *J. Fluid Mech*, 402:57–88, 2000.
 - [48] Andreas Carlson. *Capillarity and dynamic wetting*. PhD thesis, Royal Institute of Technology Department of Mechanics, Stockholm, Sweden, 2012.
 - [49] Pengtao Yue and James J. Feng. Wall energy relaxation in the Cahn–Hilliard model for moving contact lines. *Physics of Fluids*, 23(1):012106, 2011.
 - [50] Pengtao Yue, Chunfeng Zhou, and James J. Feng. Sharp-interface limit of the Cahn–Hilliard model for moving contact lines. *Journal of Fluid Mechanics*, 645:279–294, 2010.
 - [51] A. Carlson, M. Do-quang, and G. Amberg. Dissipation in rapid dynamic wetting. *Journal of Fluid Mechanics*, 682:213–240, 2011.
 - [52] Andreas Carlson, Minh Do-Quang, and Gustav Amberg. Modeling of dynamic wetting far from equilibrium. *Physics of Fluids*, 21(12):121701, 2009.
 - [53] Tiezheng Qian, Xiaoping Wang, and Ping Sheng. A variational approach to moving contact line hydrodynamics. *Journal of Fluid Mechanics*, 564:333–360, 2006.
 - [54] Klaus Jirgen Bathe. *Finite Element Procedures*. Prentice Hall, Pearson Education, Inc., 2016.
 - [55] COMSOL. *COMSOL Multiphysics User's Guide*. COMSOL Multiphysics, comsol 4.3 edition, May 2012.

3

INFLUENCE OF THE NUMERICAL PARAMETERS OF THE PHASE FIELD METHOD ON THE SLUG LENGTH OF DRY SLUG FLOW INSIDE A MICROFLUIDIC CHANNEL

3.1. INTRODUCTION

As introduced in Section 1.4, two practical problems arise when utilizing parallel microfluidic solvent extraction to purify ^{99}Mo , i.e. i) it is unknown how to produce and maintain the parallel flow pattern and, ii) there is always leakage at the outlets of the microfluidic channel. These two practical problems are related to two long-standing unsolved problems in modelling: being the *Interface Breakup Problem* and the *Moving Contact Line Problem*. This thesis explores if these two physics problems can be modelled in the framework of the Phase Field method. The theory of the Phase Field method has already been introduced in Section 2.5. For the *Moving Contact Line Problem*, the Phase Field method introduces a diffusive interface to remove the mathematical singularity at the wall, which has also been introduced in Section 2.5.

In the Phase Field method, to make the calculation affordable, the thickness of the diffusive interface is much larger than that of a physical interface [1]. As discussed in Section 2.5.1, the numerical parameters (capillary width (ϵ) and mobility parameter (M)) determine the thickness of the diffusive interface and the diffusive transport of the order parameter (ϕ) in the Phase Field method. In the Phase Field method, in the dynamic situation where the interface evolves with time, the simulation results vary with the capillary width (ϵ) and the mobility parameter (M) [2].

To ensure the Phase Field method still simulates the same physical problem when the capillary width (ϵ) is changed, the mobility parameter (M) should be changed accordingly, to generate consistent simulation results. For this purpose, the relationship between ϵ and M has been studied. However, the relationship between ϵ and M is still under debate [3] [4]. *Jacqmin* proposed that the relationship should follow $M \propto \epsilon^\delta$ with $1 \leq \delta < 2$ [5]. *Khatavkar et al.* investigated the mixing of two immiscible fluids in a lid-driven cavity flow and proposed that the relationship should be $M \propto \epsilon^{-1}$ [6]. In addition, by virtue of asymptotic expansion of the governing equations, *Magaletti et al.* proposed the relationship of $M \propto \epsilon^2$ [4]. Besides, in simulating the *Moving Contact Line Problem*, *Yue et al.* proposed to keep M constant while reducing ϵ [7].

The Phase Field method has also been reported used for simulating multiphase flows in microfluidics. *De Menech et al.* studied the droplet breakup and transition from squeezing to dripping in a T-shaped microfluidic channel with the Phase Field method [8][9]. *Ganapathy et al.* investigated the bubble formation process of gas-liquid multiphase flow in a T-shaped microfluidic channel [10] [11]. *Bai et al.* modelled the droplet formation process in a flow-focusing micro-channel with the Phase Field method [12]. However, none of them focuses on the relationship between ϵ and M in microfluidics.

The aim of this chapter is to reveal the relationship between ϵ and M in modelling microfluidic multiphase flows where the *Interface Breakup Problem* is involved. For this purpose, dry slug flow (with Ca number of both phases smaller than 1×10^{-3}) in a double Y-shaped microfluidic channel is investigated¹. In dry slug flow, by examining the

¹ *Moving Contact Line* also exists in dry slug flow [13], which is the research topic of Chapter 4.

slug length, is a direct way to verify if the *Interface Breakup Problem* is correctly modelled. In the first sets of simulation tests, it is found that prescribing the initial interface at different positions affects the simulation results. Thus, firstly, this study deals with the influence of the position of the initial interface on modelling dry slug flow. Secondly, this study reveals the influence of the capillary width (ϵ) and the mobility parameter (M) on the slug length in microfluidics. Lastly, the slug length calculated with the Phase Field method will be compared with that in the experiments, to validate the simulation results.

3.2. MATERIALS AND METHODS

3.2.1. MICROFLUIDIC CHIP AND EXPERIMENTAL PROCEDURE

The microfluidic chip (IMT ICC-DY05, Material: borosilicate glass) was purchased from the Institute of Microchemical Technology Company. The channel was double Y-shaped with two inlets and two outlets, see Figure 3.1. The detailed information of the geometry of the microfluidic channel is illustrated in Table 3.1. Its two inlets were connected to two syringes (1mL, Inkjet-F, BD) separately by capillary tubings (PEEK, Length: 25 cm, ID: 0.26mm). The syringes were driven by two Aladdin single-syringe pumps (WPI). The flow rate accuracy of the syringe pump was $\pm 1.5\%$ when carrying the 1mL syringe. The two outlets were connected to two glass vials to collect the samples.

Table 3.1: Geometry of IMT ICC-DY05 microfluidic chip

Material	Length (cm)	Width (μm)	Depth (μm)	Guide
Borosilicate glass	2	100 ± 0.2	40 ± 0.1	No

Before the experiment, the microfluidic chip was rinsed with ethanol for around ten minutes. The ethanol was introduced into the microfluidic channel through the connecting tubings by single-syringe pumps. After rinsing with the ethanol, the whole system was flushed with Milli-Q water (water that has been purified using resin filters and deionized to a high degree) for around ten minutes. During the measurement, at each flow rate, the whole microfluidic system was first pumped with the aqueous solution. After making sure that there was no gas bubble in the microfluidic system, the organic solution was pumped into the microfluidic channel. In the experiment, Milli-Q water served as the aqueous solution and n-heptane served as the organic solution.

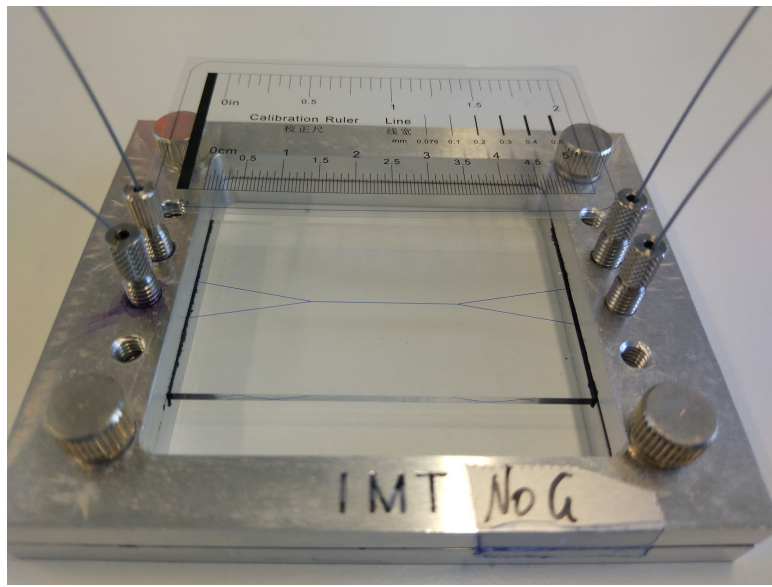


Figure 3.1: The microfluidic channel is double Y-shaped with two inlets and two outlets. The chip is fixated with an aluminium holder. A methylene blue solution ($0.1\%, w/w$) is flowing through the microfluidic chip, for the purpose of highlighting the microfluidic channel.

3.2.2. FLUID PROPERTIES AND MEASUREMENT OF THE EQUILIBRIUM CONTACT ANGLE

The n-heptane used in this research was purchased from Sigma-Aldrich. The water was supplied from the Milli-Q system. The physical properties of the fluids are listed in Table 3.2.

Table 3.2: Physical properties of fluids in the simulations

Fluids	Viscosity (Pa · s)	Density (g/cm ³)	Coefficient of interfacial tension (mN/m)
Water	1×10^{-3}	1	
n-heptane	3.86×10^{-4}	0.68	50.2

The equilibrium contact angle (θ_e) was measured with a computer controlled instrument: CAM 200 (KSV Instruments Ltd). In Figure 3.2a, the pipette tip of the CAM 200 instrument is placing one droplet of water on the surface of one piece of glass. The tip is lowered just until the droplet touches the glass surface and the tip is raised again, leaving the droplet on the glass surface. Then, a picture is taken and the equilibrium contact

angle (θ_e) is derived by analyzing the droplet shape with the built-in image analysis software based on Young-Laplace fit [14].



(a) The pipette tip of the CAM 200 instrument is placing one droplet of water on the surface of one piece of glass.

(b) The macro cuvette

Figure 3.2: The pipette tip of the CAM 200 instrument and the macro cuvette.

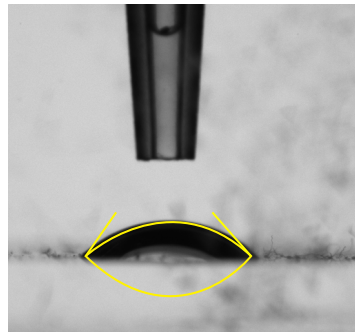


Figure 3.3: Schematic diagram of measurement of the equilibrium contact angle (θ_e). One droplet of water was supplied to the bulk n-heptane solution contained by the macro cuvette.

In the case of measuring the equilibrium contact angle (θ_e) between water and n-heptane, a container was needed for the bulk solution. For this, a macro cuvette with a glass surface (Dimension: 40 mm × 23.6 mm × 25 mm, Hellma Macro-cuvette, Material: glass) was chosen, see Figure 3.2b. Before the measurement, the macro cuvette was cleaned with ethanol and partially filled with n-heptane. In the measurement, one droplet water of 5 μ L was provided by the pipette tip to the bottom surface of the macro cuvette.

The equilibrium contact angle of the water droplet in the bulk n-heptane solution was measured to be $47^\circ \pm 4^\circ$. The measurement was repeated 6 times. Figure 3.3 illustrates a picture of the water droplet taken by the camera of the CAM 200 instrument.

3.2.3. SLUG LENGTH OF DRY SLUG FLOW

This chapter focuses on the slug flow pattern, features of which have already been introduced in Section 1.3.1. Usually, at room temperature, when $Ca < 1 \times 10^{-3}$ for both phases, dry slug flow occurs [13]. The maximum Ca number to be investigated in the experiments is 7.47×10^{-4} , which guarantees that the flow pattern belongs to dry slug flow. The "slug length" in this research refers to the length where the organic slugs are in direct contact with the microfluidic chip wall, as illustrated in Figure 3.4.

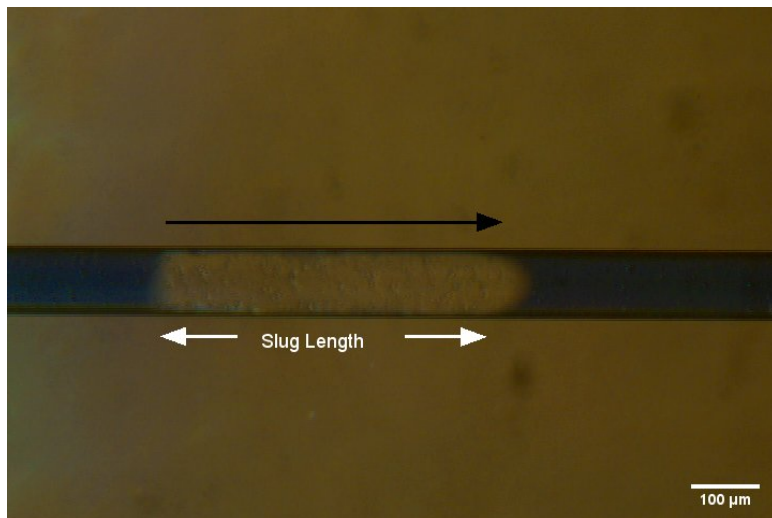


Figure 3.4: The slug length of a n-heptane slug inside the microfluidic chip. The black arrow indicates the flow direction. The water phase is dyed with methylene blue (0.1%, w/w).

3.2.4. GOVERNING EQUATIONS AND MODEL DESCRIPTION

The governing equations for dry slug flow of water and n-heptane in a microfluidic channel are the Cahn-Hilliard equation (Equation 2.23), the continuity equation (Equation 2.2) and the Navier-Stokes momentum equations (Equation 2.24) for multiphase flows. These equations have been introduced in detail in Section 2.5. Besides, the dimensionless formation of these equations as well as the related dimensionless numbers are introduced in Section 2.5.4.

Based on the geometry of the microfluidic channel in Table 3.1, a 2-dimensional model was built in COMSOL by placing the bottom-left point of the main channel on the (0, 0) point in the 2-dimensional Cartesian coordinate. In Figure 3.5, the horizontal axis and the vertical axis show the x-position and y-position in the 2-dimensional coordinate, respectively.

As shown in Figure 3.6a, the average velocity of the fluids at the two inlets was prescribed as boundary conditions. The average velocity was calculated based on the volumetric flow rates of fluids and the cross-sectional area of the inlets of the IMT ICC-DY05 microfluidic chip. The velocity profile was assumed to be fully developed Poiseuille flow, as shown in Figure 3.7a. This condition was acceptable because the fluid flowed through a relatively long capillary tubing (Length: 25 cm) which connected the syringes and the microfluidic chip in the experiments. Figure 3.7b demonstrates a typical case of the fully developed flow velocity profile at the water inlet (upper inlet) of the microfluidic channel. The average velocity is $4.17 \times 10^{-3} \text{ m s}^{-1}$ (the corresponding Re number is 0.42) and the flow profile is parabolic. At the two outlets, as shown in Figure 3.6b, a reference pressure (Pressure = 0 Pa) was used as the boundary condition. The no-slip boundary condition was imposed at the solid walls. Equation 2.39 with $\mu_f = 0 \text{ Pa} \cdot \text{s}$ was adopted for the boundary condition for the contact angle. Such a boundary condition is termed the equilibrium contact angle boundary condition. The value of the equilibrium contact angle (θ_e) was 47° , as measured in Section 3.2.2.

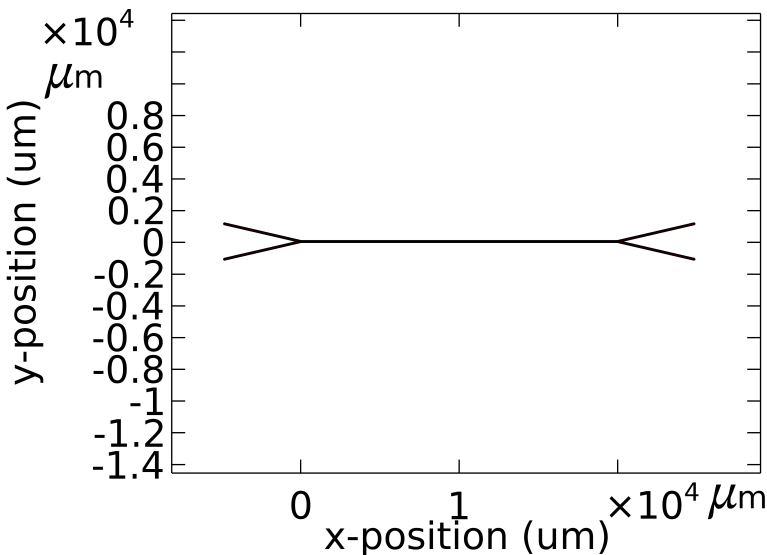


Figure 3.5: The 2-dimensional model based on the IMT ICC-DY05 microfluidic chip built in COMSOL.

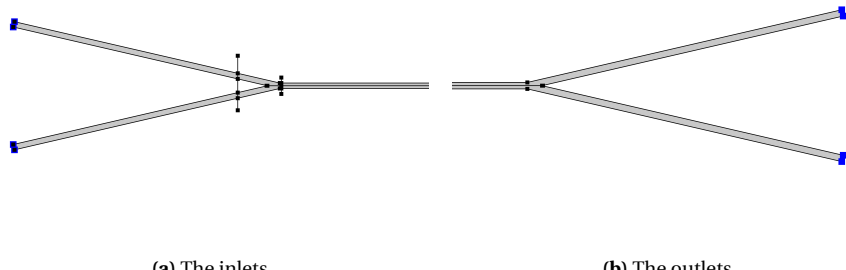


Figure 3.6: Inlets and outlets of the microfluidic channel in COMSOL.

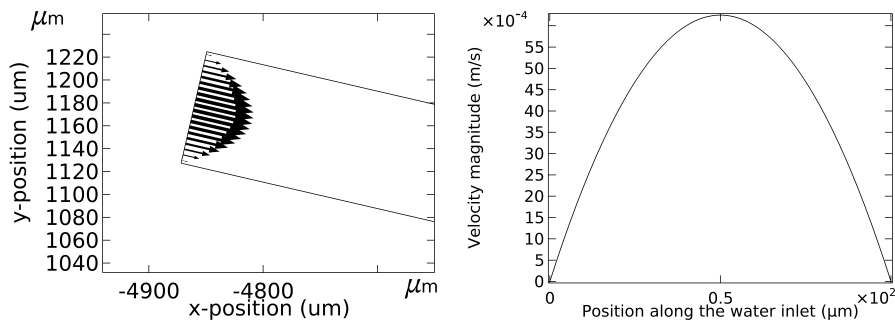


Figure 3.7: Velocity prescribed at the water inlet (the upper inlet) of the microfluidic channel.

Figure 3.8 illustrates a typical case of the n-heptane slug formation process. The color legend indicates the value of the order parameter (ϕ). $\phi = 1$ represents the aqueous phase, $\phi = -1$ represents the n-heptane, and the intermediate region is the diffusive interface. Due to the diffusive interface with finite thickness, the interface is not a sharp line. In this research, the contour line of $\phi = 0$ is therefore regarded as the interface when obtaining the slug length in the simulations. In Figure 3.8, the flow rates of both phases are $1.0 \mu\text{L}/\text{min}$. The corresponding Ca number of the aqueous phase is 1.07×10^{-4} while the Ca number of n-heptane is 4.13×10^{-5} . In Figure 3.8a, a n-heptane slug is forming and the slug becomes longer in Figure 3.8b. The n-heptane slug is formed in Figure 3.8c and it is moving in the main channel in Figure 3.8d.

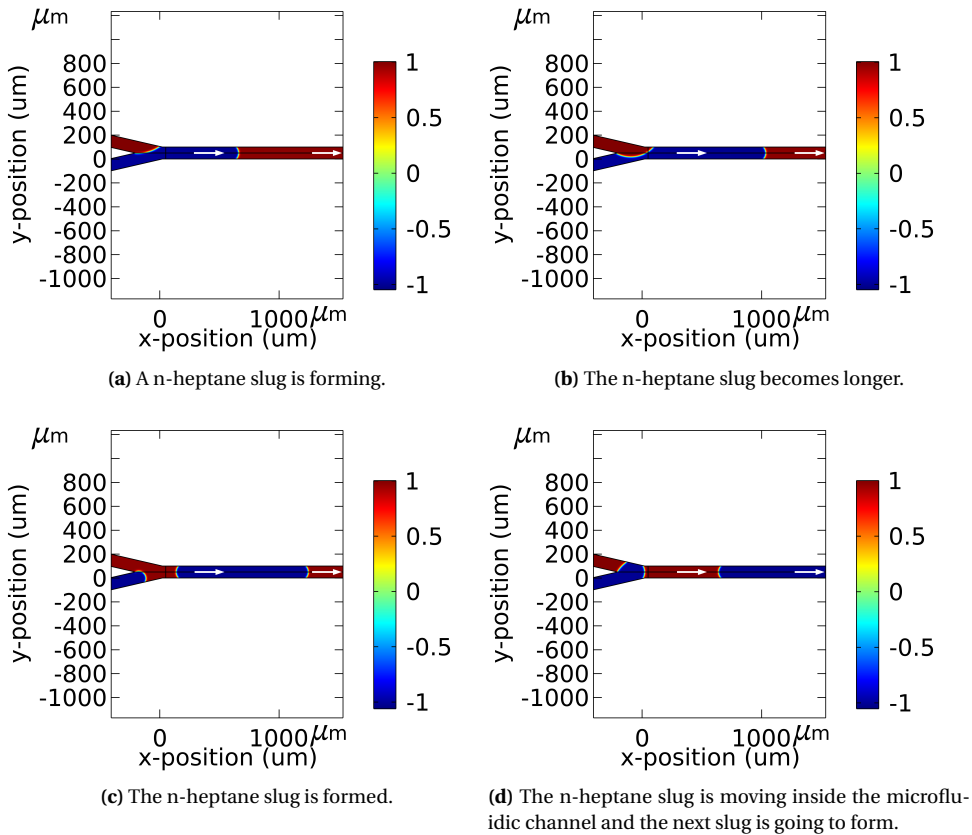


Figure 3.8: Numerical results of the n-heptane slug formation process inside the microfluidic chip. The white arrow indicates the direction of the flow. The color legend indicates the value of the order parameter ϕ . $\phi = 1$ indicates the aqueous phase while $\phi = -1$ represents the n-heptane.

3.2.5. MESH DEPENDENCY STUDY

COMSOL solves the series of PDEs that govern multiphase flows in the microfluidic channel with the Finite Element Method. The COMSOL built-in solver Parallel Direct Sparse Solver (PARDISO) was chosen with a relative tolerance of 0.01. As for the time domain, the backward differentiation formula (BDF) was selected and the maximum time step was limited to 0.001 s.

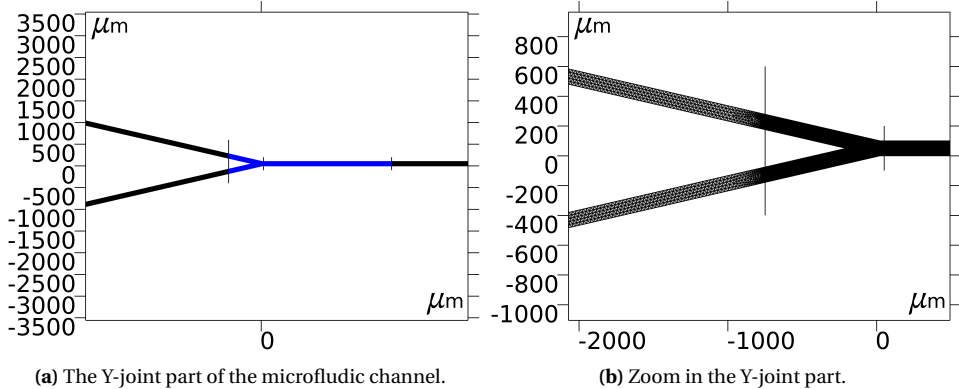


Figure 3.9: Finer mesh is used in the Y-joint part at the inlets of the microfluidic channel.

The "free triangular" meshes were chosen in the simulations, as shown in Figure 3.9b. The mesh size was set between a minimum of $5\mu\text{m}$ and a maximum of $25\mu\text{m}$. At the Y-joint part of the microfluidic channel (the blue part of Figure 3.9a with a length of $3000\mu\text{m}$ in the main channel), finer meshes were chosen, to ensure there are enough node points within the diffusive interface [15]. The initial interface was prescribed within the Y-joint part, the reason for this will be explained in Section 3.3.1. If slugs are formed and before they leave the Y-joint part, the calculation is stopped. In this way, the calculation is not too expensive, compared with meshing the whole channel with the finner mesh.

A mesh-independence study was conducted at $\epsilon = 6\mu\text{m}$ by examining the slug length. The choice of $\epsilon = 6\mu\text{m}$ ensured that the calculation was affordable (keeping the calculation time within a few hours). Figure 3.10 illustrates the dimensionless slug length by changing the maximum mesh size at the Y-joint part while keeping other parameters (including the mesh size of other parts) constant. In Figure 3.10, when decreasing the maximum mesh size to $6\mu\text{m}$, no noticeable deviation on the slug length is found. As introduced in Section 2.5.1, the thickness of the diffusive interface equals approximately 4 times the capillary width (ϵ). Hence, for $\epsilon = 6\mu\text{m}$, the thickness of the diffusive interface is about $24\mu\text{m}$. With the maximum mesh size being $6\mu\text{m}$, there are at least 4 node points within the diffusive interface. The Cn number describes the ratio between the capillary width (ϵ) and the characteristic length (L) of the microfluidic system. In this thesis, to make the calculation affordable, the choice of the Cn number therefore ranges from 0.04 to 0.1.

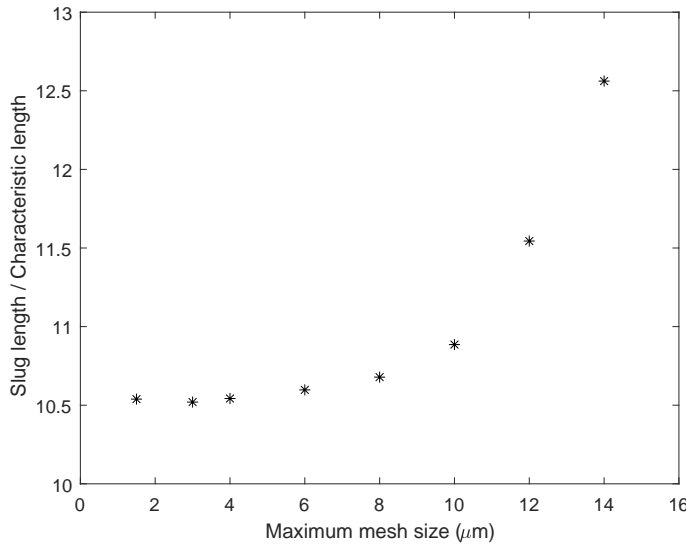


Figure 3.10: Mesh dependency study for dry slug flow in COMSOL. The horizontal axis shows the maximum mesh size at the Y-joint part. The vertical axis indicates the dimensionless slug length which is the ratio of the slug length to the characteristic length (L) of the microfluidic channel (width of the channel).

3.3. RESULTS AND DISCUSSION

In this research, three main flow patterns are observed. One of them is the dry slug flow pattern. In this flow pattern, one phase is dispersed at the Y-shaped joint part of the microfluidic channel, as depicted in Figure 3.11a. One other flow pattern is the parallel flow pattern, which is to be used in the microfluidic solvent extraction to ^{99}Mo . In this flow pattern, two immiscible phases flow side-by-side continuously and neither of them is dispersed in the main channel of the microfluidic channel, as depicted in Figure 3.11c. Besides the above mentioned dry slug flow and parallel flow, there is a third flow pattern: the transition flow pattern. In the transition flow pattern, in the beginning, the immiscible two phases flow side-by-side in the main channel. However, the interface breaks at the Y-shaped part of the outlets of the microfluidic channel and one phase is dispersed, as illustrated in Figure 3.11b. The dry slug flow pattern occurs when the volumetric flow rates of both phases are low. By increasing the volumetric flow rates of both phases at the inlets, the dry slug flow pattern changes to the transition flow pattern and eventually to the parallel flow pattern. The change of these flow patterns will be further discussed in Chapter 5.

3

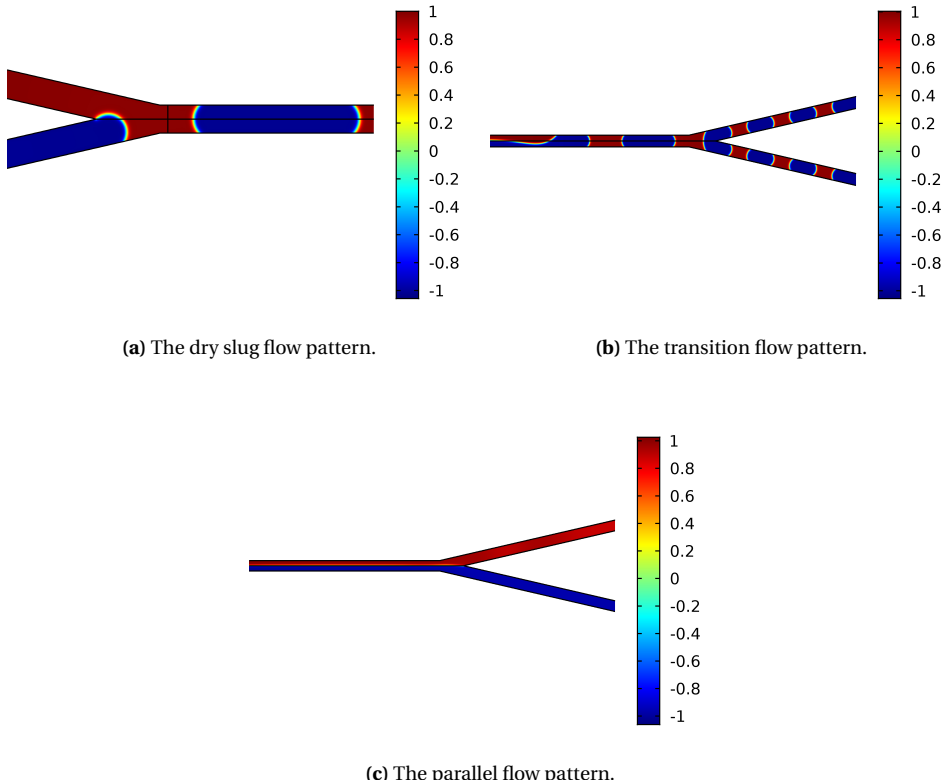


Figure 3.11: Schematic diagram of flow patterns inside a double Y-shaped microfluidic channel. The color legend indicates the value of the order parameter ϕ . $\phi = 1$ indicates the aqueous phase while $\phi = -1$ represents the organic phase. The dry slug flow pattern occurs when the volumetric flow rates of phases are low. By increasing the volumetric flow rates of both phases at the inlets, the dry slug flow pattern changes to the transition flow pattern and eventually to the parallel flow pattern.

3.3.1. STUDY OF THE INITIAL INTERFACE IN THE PHASE FIELD METHOD

In this study, the initial interface in the simulation is either prescribed in the middle of the microfluidic channel (as demonstrated in Figure 3.12a) or at the Y-joint part of the microfluidic channel (as illustrated in Figure 3.12b). In general, parallel flow occurs when the volumetric flow rates are higher while dry slug flow occurs when volumetric flow rates are lower. Prescribing the initial interface in the middle of the microfluidic channel aims to simulate if the parallel flow pattern can transform into dry slug flow by reducing volumetric flow rates. Prescribing the initial interface at the Y-joint part models the experimental procedure as described in Section 3.2.1 where the aqueous phase was always first pumped into the microfluidic channel.

In the first test, the initial interface is prescribed in the middle of the microfluidic channel, as illustrated in Figure 3.12a. In the simulations, the contact line friction parameter (μ_f) is set to zero. The mobility parameter (M) is a measure for the diffusive transport of the order parameter (ϕ). In this test, the mobility parameter (M) has been varied in the range from $1.60 \times 10^{-14} \text{ m}^3/\text{kg}$ to $1.60 \times 10^{-3} \text{ m}^3/\text{kg}$. When the value of the mobility parameter (M) is out of this range, the simulation results do not converge. *Jacqmin* reported that the convergence of the Phase Field method did not only depend on meshing but also on the mobility parameter (M). This parameter needed to be selected large enough to ensure convergence. However, if the value of the mobility parameter (M) was too large, it would overly damp the flow, leading to non-convergent results [1] [5].

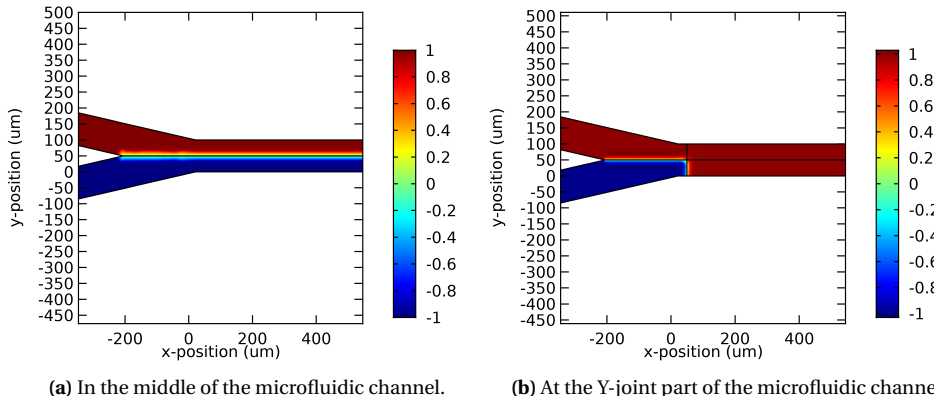


Figure 3.12: Schematic diagram of the position of the initial interface inside the double Y-shaped microfluidic channel. The color legend indicates the value of the order parameter ϕ . $\phi = 1$ indicates the aqueous phase while $\phi = -1$ represents the organic phase.

Figure 3.13 demonstrates the flow pattern map of the convergent simulation results when the initial interface is prescribed in the middle of the microfluidic channel. The Cn number (being a measure for ϵ) is plotted on the vertical axis while the Pe number (being a function of both ϵ and M) is plotted on the horizontal axis. In Figure 3.13 the Ca num-

ber of the aqueous phase is 4.15×10^{-4} while the Ca number of n-heptane is 3.20×10^{-4} . The Pe number and the Ca number are calculated based on the average velocity of the fluids at the inlets of the microfluidic channel. According to Section 3.2.3, at such low Ca number ($Ca < 1 \times 10^{-3}$), dry slug flow is expected. However, in Figure 3.13, the flow pattern always belongs to the parallel flow pattern, regardless of the Cn number and the Pe number. Additionally, numerical tests were conducted by changing the Ca number (varying the volumetric flow rates) of both phases between 1×10^{-5} and 1×10^{-3} . However, the parallel flow pattern remains throughout the whole channel. Obviously, these simulation results do not agree with experimental observations that the dry slug flow appears when the Ca number of both phases is smaller than 1×10^{-3} .

3

To further investigate this phenomenon, Figure 3.14 has been set up. Figure 3.14 depicts the distribution of the order parameter (ϕ) along the width of the channel when the initial interface is prescribed in the middle of the microfluidic channel. The vertical axis represents the value of the order parameter (ϕ) while the horizontal axis denotes the width of the microfluidic channel (*i.e.*, the vertical direction in Figure 3.12a at x -position = 400 μm). In Figure 3.14, the Cn number is set to 0.06 and the Pe number of the aqueous phase is set to 6.52×10^{-2} (the corresponding symbol for this data point has already been made larger in Figure 3.13), as a typical test case that the profile has become stationary.

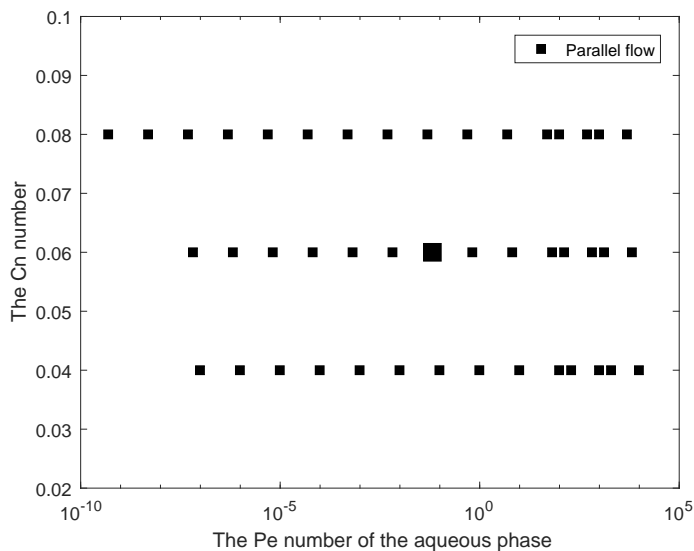


Figure 3.13: The flow pattern map of the simulation results when the initial interface is prescribed in the middle of the microfluidic channel. The Ca number of the aqueous phase is 4.15×10^{-4} while the Ca number of n-heptane is 3.20×10^{-4} . The larger data point indicates the simulation conditions of Figure 3.14.

In Figure 3.14, it can be seen that the profile of the order parameter (ϕ) appears as a hyperbolic tangent function shape, which indicates that the diffusive interface is at equilibrium. In addition, the profile of the order parameter (ϕ) is the same at time 0.01 s, 0.05 s and 0.08 s, which means that the profile is stationary.

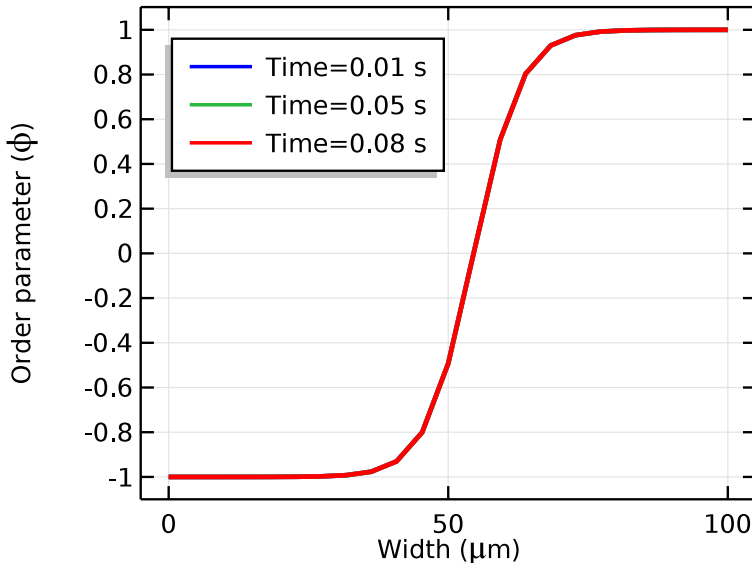


Figure 3.14: Distribution of the order parameter (ϕ) along the width of the microfluidic channel when the initial interface is prescribed in the middle of the microfluidic channel. $\phi = 1$ indicates the aqueous phase while $\phi = -1$ represents the organic phase. The Ca number of the aqueous phase is 4.15×10^{-4} while the Ca number of n-heptane is 3.20×10^{-4} . $\mu_f = 0 \text{ Pa} \cdot \text{s}$. $Cn = 0.06$. $Pe = 6.52 \times 10^{-2}$. The lines for the three times are overlapped.

The evolution of the order parameter (ϕ) is a key factor in calculating the interfacial tension in the Phase Field method. As explained in Section 2.5.1, the Phase Field method minimizes the free energy (E_{free}) of the whole system by changing the distribution of the order parameter (ϕ), to approach the equilibrium state. On the other hand, the convective flow tries to distort the equilibrium interface [5]. As a result, the dynamics of the interface is reflected by the competition between the order parameter (ϕ) relaxing to the equilibrium state and the convective flow distorting it from the equilibrium state. When the initial interface is prescribed in the middle of the microfluidic channel, the convective flow (in the y-direction of Figure 3.12a) is not strong enough to distort the equilibrated interface. In this case, the diffusive interface loses its "dynamics" and is unable to calculate the interfacial tension in the Phase Field method.

When the initial interface is prescribed at the Y-joint part of the microfluidic channel, as illustrated in Figure 3.12b, the initial interface is distorted by convective flow. Then,

the distorted diffusive interface tends to relax to the equilibrium state, thereby changing the free energy (E_{free}) of the system. Under such a circumstance, the interfacial tension can be expressed and dry slug flow occurs as expected. Thus, in this thesis, the initial interface is positioned at the Y-joint part of the microfluidic channel unless mentioned otherwise.

3.3.2. THE PE NUMBER VERSUS SLUG LENGTH

3

As introduced in Section 2.5, the Phase Field method introduces a diffusive interface to remove the mathematical singularity at the solid wall when the no-slip boundary condition is applied. The mobility parameter (M) controls the diffusive movement of the order parameter (ϕ) within the diffusive interface while the capillary width (ϵ) determines the thickness of the diffusive interface. However, how the mobility parameter (M) and the capillary width (ϵ) determine the interface breakup dynamics is not known. In Section 3.3.2 and Section 3.3.3, this topic will be investigated by monitoring the slug length within a microfluidic channel. Specifically, Section 3.3.2 focuses on the relationship between the mobility parameter (M) and the slug length while Section 3.3.3 focuses on the relationship between the capillary width (ϵ) and the slug length.

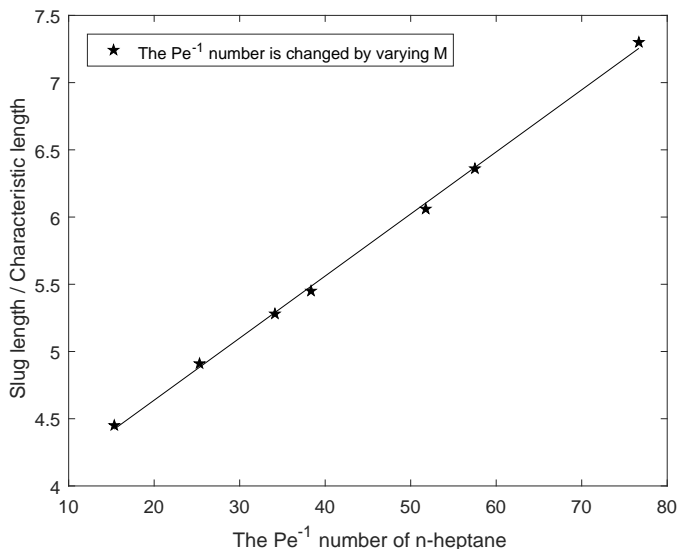
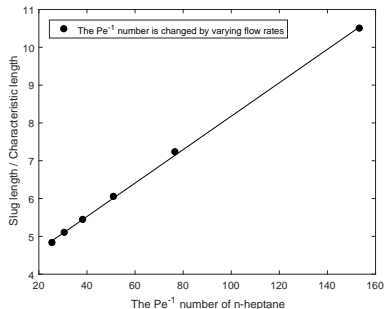


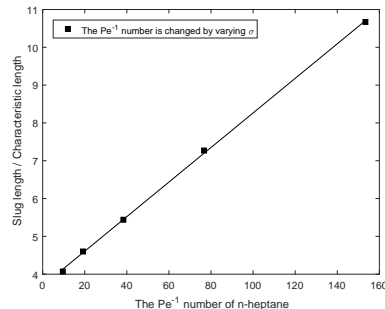
Figure 3.15: The slug length of n-heptane is linearly proportional to the Pe^{-1} number of n-heptane. The coefficient of determination (R^2) of the linear regression line is 0.9988. In the simulations, the Cn number is 0.06 and the volumetric flow rate of both phases are $2.0\mu\text{L}/\text{min}$.

In the simulations, the volumetric flow rate of the two phases is $2.0\mu\text{L}/\text{min}$ while the corresponding Ca number of water and n-heptane is 1.66×10^{-4} and 6.41×10^{-5} , respectively. Such small Ca numbers ensures dry slug flow ($Ca < 1 \times 10^{-3}$). M is varied from

$1.44 \times 10^{-9} \text{ m}^3/\text{kg}$ to $7.20 \times 10^{-9} \text{ m}^3/\text{kg}$, while the Cn number is 0.06 (reflecting a constant interface thickness). Figure 3.15 illustrates the relationship between the slug length and mobility parameter (M) simulated with the Phase Field method. On the horizontal axis, the reciprocal of the Pe number of n-heptane is plotted, as the mobility parameter (M) only appears in the Pe number. Clearly, the slug length increases linearly with the reciprocal of the Pe number (by varying M). To further test if the slug length is linearly proportional the Pe^{-1} number by varying other variables in the Pe number, Figure 3.16 illustrates the simulation results of the influence of the Pe^{-1} number on the slug length when the Pe^{-1} number is varied by changing the flow rates or by varying the coefficient of interfacial tension (σ).



(a) The slug length of n-heptane is linearly proportional to the Pe^{-1} number when the flow rates are varied. The R^2 of the linear regression line is 0.9994. $\sigma = 50.2 \text{ mN/m}$.



(b) The slug length of n-heptane is linearly proportional to the Pe^{-1} number when σ is varied. The R^2 of the linear regression line is 0.9986. The flow rate of both phase is $2.0 \mu\text{L}/\text{min}$.

Figure 3.16: Influence of the Pe^{-1} number on the slug length. The Cn number is 0.06 and M is $3.60 \times 10^{-9} \text{ m}^3/\text{kg}$.

Figure 3.16a presents the dimensionless slug length as a function of the Pe^{-1} number varied by changing flow rates. The Cn number is kept at 0.06 and M is kept at $3.60 \times 10^{-9} \text{ m}^3/\text{kg}$. The volumetric flow rates of the two phases are always kept the same ($\Phi_{aq} = \Phi_{org}$). As the flow rates are varied, the corresponding Ca number of n-heptane is in the range of 1.60×10^{-5} to 9.61×10^{-5} . In Figure 3.16a, it is clear that the slug length is still linearly proportional to the reciprocal of the Pe number at different flow rates. In addition, Figure 3.16b illustrates the simulation results when the Pe^{-1} number is varied by only changing the coefficient of interfacial tension (σ). The Cn number and M are the same as those of Figure 3.16a. In Figure 3.16b, the flow rate of both phase is $2.0 \mu\text{L}/\text{min}$, which is the same as that of Figure 3.15. When the coefficient of interfacial tension (σ) is varied, the corresponding Ca number of n-heptane varies from 1.60×10^{-5} to 2.56×10^{-4} . The results in Figure 3.16b show that the slug length is still linearly proportional to the Pe^{-1} number when the Pe^{-1} number is varied by changing the coefficient of interfacial tension (σ).

To investigate if the slug length is determined by the Pe number when the Cn number is fixed, Figure 3.17 illustrates the slug length when the Pe number is set to 1.30×10^{-2} or 2.60×10^{-2} when the Cn number is 0.06. The coefficient of interfacial tension (σ) between water and n-heptane is varied, as shown on the horizontal axis. In this process, the Ca number of both phases is always smaller than 1×10^{-3} . At the same time, the mobility parameter (M) is also changed accordingly to keep the Pe number at 1.30×10^{-2} or 2.60×10^{-2} . In addition, the flow rate of both phases is $1.0 \mu\text{L}/\text{min}$ in Figure 3.17a and $2.0 \mu\text{L}/\text{min}$ in Figure 3.17b. Based on the results of Figure 3.17, when the Pe number is 1.30×10^{-2} , the dimensionless slug length is around 7 and when the Pe number is 2.60×10^{-2} , the dimensionless slug length is around 5.5. These results indicate that it is equivalent to varying the three variables (U , M and σ) in the Pe number ($Pe = \frac{2\sqrt{2}UL\epsilon}{3M\sigma}$) when the Cn number is fixed. It can be concluded that when the Ca number is less than 1×10^{-3} and the Cn number is fixed, for the given system (L is constant), the slug length in the microfluidic channel is determined by the Pe number.

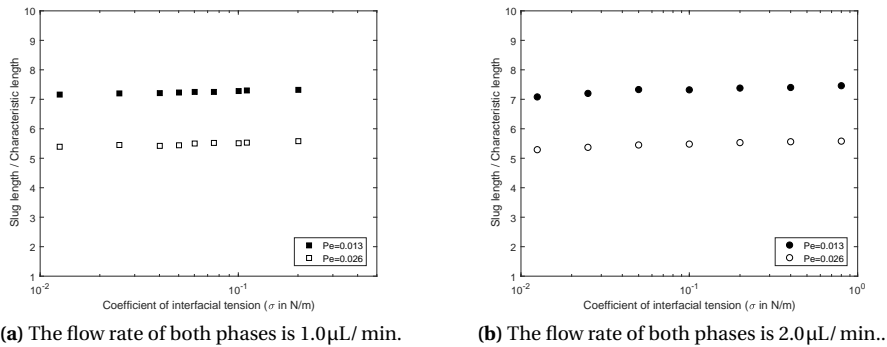


Figure 3.17: Relationship between the Pe number and the slug length with the Cn number fixed at 0.06. The coefficient of interfacial tension (σ) between water and n-heptane is varied. At the same time, the mobility parameter (M) is also changed accordingly to keep the Pe number at 1.30×10^{-2} or 2.60×10^{-2} .

3.3.3. THE Cn NUMBER VERSUS SLUG LENGTH

In Section 3.3.2, it was shown that the slug length is linearly proportional to the Pe^{-1} number when the Cn number is fixed. This section discusses the influence of the Cn number on the slug length and the relationship between the Cn number and the Pe^{-1} number in determining the slug length.

As introduced in Equation 2.45, the Cn number is defined as the ratio of the capillary width (ϵ) and the characteristic length (L) of the microfluidic system. Figure 3.18 shows the influence of the Cn number on the slug length, with a flow rate of both phases of

$1.0\mu\text{L}/\text{min}$ and the coefficient of interfacial tension $\sigma = 50.2\text{mN/m}$. When ϵ is varied, the mobility parameter (M) is also changed accordingly to keep the Pe number at 1.30×10^{-2} or 2.60×10^{-2} . According to the results of Figure 3.17, when the value of ϵ is fixed, the slug length is linearly proportional to the Pe^{-1} number. However, Figure 3.18 shows that, when ϵ is changed, even though the Pe number kept constant by varying M accordingly, the slug length changes with respect to ϵ . Thus, ϵ influences the slug length independently.

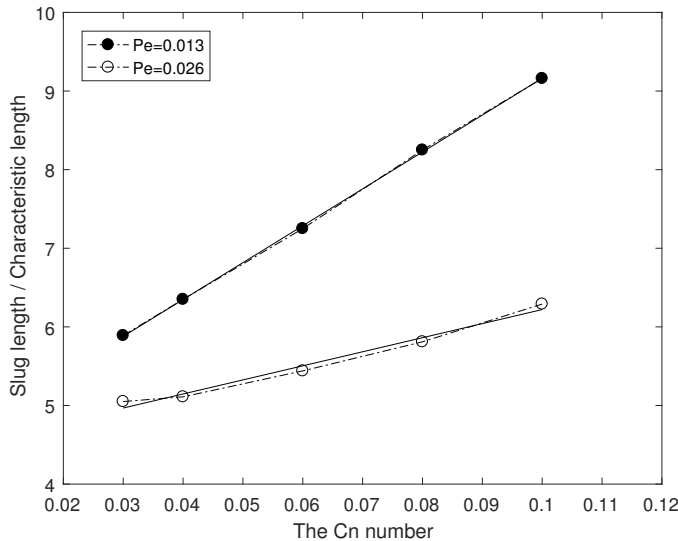
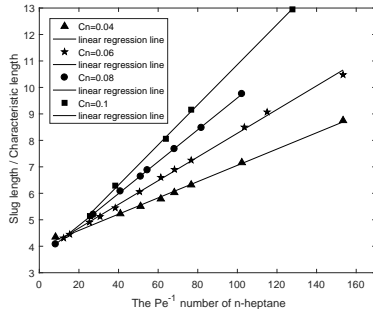


Figure 3.18: Influence of the Cn number on the slug length. When ϵ is varied, the mobility parameter (M) is also changed accordingly to keep the Pe number at 1.30×10^{-2} or 2.60×10^{-2} . The flow rate of both phases is $1.0\mu\text{L}/\text{min}$. $\sigma = 50.2\text{mN/m}$. The values of R^2 are all larger than 0.98 for the linear regression lines.

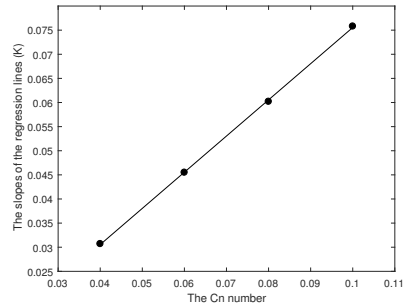
To further investigate the relationship between the slug length and the Cn number, Figure 3.19a demonstrates the relationship between the slug length and the reciprocal of the Pe number at the Cn number of 0.04, 0.06, 0.08 and 0.1. In the simulations, the Pe^{-1} number is changed by varying the mobility parameter (M) and the flow rates. In this process, the flow rates of the two phases are always kept the same ($\Phi_{aq} = \Phi_{org}$) and the coefficient of interfacial tension (σ) is constant ($\sigma = 50.2\text{mN/m}$). At each value of the Cn number, the slug length is still linearly proportional to the reciprocal of the Pe number. Focusing on the relationship between the slope (K) of the linear regression lines and the Cn number, the slopes (K) of the linear regression lines are 0.0307, 0.0455, 0.0602 and 0.0758 for $Cn = 0.04, 0.06, 0.08$ and 0.1 , respectively. The slopes (K) are also approximately linearly proportional to the Cn number (see Figure 3.19b), which indicates that the slug length is linearly proportional to the Cn number. For that reason, it would be interesting to investigate the dimensionless slug length (Slug

length/Characteristic length) versus the product $CnPe^{-1}$. Figure 3.19c shows the dimensionless slug length versus this product. The data in Figure 3.19c are directly extracted from Figure 3.19a. In Figure 3.19c, the dimensionless slug length follows linear relationship: Slug length/Characteristic length = $0.72CnPe^{-1} + 3.86$. This result indicates that, for dry slug flow ($Ca < 1 \times 10^{-3}$), to keep the slug length constant, the mobility parameter (M) needs to be changed according to $CnPe^{-1} = \text{constant}$.

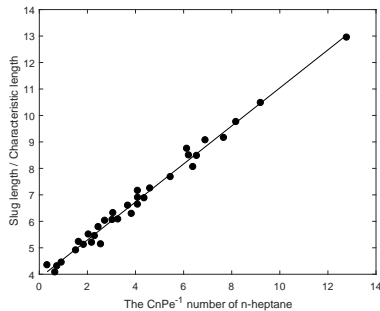
3



(a) The triangles, stars, circles and squares represent the simulation results when the Cn number is 0.04, 0.06, 0.08 and 0.1, respectively. The values of R^2 are all larger than 0.99 for the linear regression lines when the Cn number is varied.



(b) The slope (K) of the linear regression lines (from Figure 3.19a) versus the Cn number. The R^2 for the linear regression line is 0.9988.



(c) The data are directly extracted from Figure 3.19a. The R^2 for the linear regression line is 0.9877.

Figure 3.19: Relationship between the slug length and the Pe^{-1} number when the Cn number is varied.

The meaning of the relationship between the Cn number and the Pe number (*i.e.*, $CnPe^{-1} = \text{constant}$) can be explained by the mechanism of the Phase Field method. As explained in Section 2.5.1, the Phase Field method minimizes the free energy (E_{free}) of the whole system by changing the distribution of the order parameter (ϕ), relaxing to an equilibrium state. In the meanwhile, the interfacial tension is reflected by the order parameter (ϕ)

relaxation process [2]. Since the mobility parameter (M) determines the order parameter (ϕ) relaxation speed, the calculated interfacial tension is a function of the mobility parameter (M). To be more specific, as shown in Figure 3.17, when the Cn number is constant, it is equivalent to varying the mobility parameter (M) or the interfacial tension coefficient (σ), to obtain the same slug length by keeping the Pe number a constant. Thus, it can be concluded that the calculated interfacial tension is linearly proportional to the mobility parameter (M). As for the influence of the Cn number, according to the expression for the interfacial tension (Equation 2.32) of the Phase Field method, the capillary width (ϵ) appears in the generalized chemical potential (G in Equation 2.17), which indicates that the calculated interfacial tension is also a function of the capillary width (ϵ). Concerning the relationship between the Cn number and the calculated interfacial tension, Figure 3.18 shows that the slug length is linearly proportional to the Cn number when the Pe number is constant. In addition, Figure 3.16b has already illustrated that the slug length is linearly proportional to the coefficient of interfacial tension (σ). Thus, combining the results in Figure 3.18 and Figure 3.16b, it can be found that the calculated interfacial tension is also linearly proportional to the capillary width (ϵ). Since calculated interfacial tension is linearly proportional to both the capillary width (ϵ) and the mobility parameter (M), to obtain the same calculated interfacial tension, the capillary width (ϵ) and the mobility parameter (M) should be chosen by following $CnPe^{-1} = \text{constant}$.

3.3.4. COMPARING SLUG LENGTH IN THE SIMULATIONS WITH THAT IN THE EXPERIMENTS

In the Phase Field method, when the capillary width (ϵ) is fixed, there should be one specific value of the mobility parameter (M) that can reflect the dynamics of a physical interface between two specific combination of fluids [12]. This section focuses on the comparison of the slug length in the experiments with the one in the simulations, to check if one specific combination of the mobility parameter (M) and capillary width (ϵ) can reflect the interfacial dynamics correctly. In the experiments, the slug length of n-heptane is measured at various volumetric flow rates while the volumetric flow rates of water and n-heptane are always equal to each other. The results are plotted in Figure 3.20 in terms of the Ca number of n-heptane. In Figure 3.20, the asterisks with error bars represent the experimentally measured slug length with its standard deviation. Each slug length in the experimental data is the average of 7 n-heptane slugs in the same experimental conditions. Figure 3.20 shows that as the Ca number is increased, the slug length decreases.

Figure 3.20 also illustrates the simulation results when the Cn number has a fixed value of 0.06, to keep it computationally affordable. Figure 3.20 demonstrates the simulation results when the mobility parameter (M) is set to $1.44 \times 10^{-9} \text{ m}^3/\text{s}/\text{kg}$, $3.60 \times 10^{-9} \text{ m}^3/\text{s}/\text{kg}$ and $5.60 \times 10^{-9} \text{ m}^3/\text{s}/\text{kg}$, respectively. The Ca number of n-heptane is changed by varying the volumetric flow rates. In this process, the flow rates of the two phases are always kept the same ($\Phi_{aq} = \Phi_{org}$) and the coefficient of interfacial tension (σ) is constant ($\sigma = 50.2 \text{ mN/m}$). It can be seen that the slug length of n-heptane equals the experimental results reasonably well when the mobility parameter (M) is set to $3.60 \times 10^{-9} \text{ m}^3/\text{s}/\text{kg}$.

Thus, the combination of $Cn = 0.06$ and $M = 3.60 \times 10^{-9} \text{ m}^3 \text{s/kg}$ can be regarded to reflect the interfacial dynamics of the water and n-heptane system, which will be further used in Chapter 4.

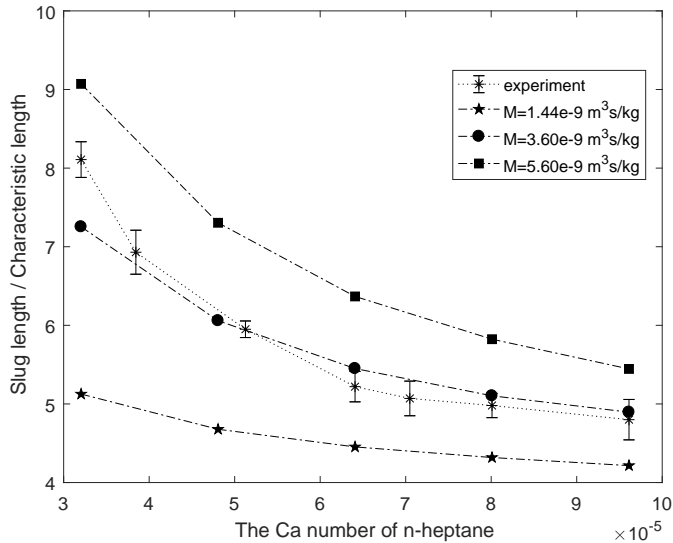


Figure 3.20: The slug length of n-heptane in the experiments versus the slug length in the simulations. The Ca number is changed by varying the volumetric flow rates in both the experiments and simulations while keeping $\Phi_{aq} = \Phi_{org}$. The asterisks with error bars represent the experimental results with the standard deviation. The star, round and square symbols denote the simulation results of $M=1.44 \times 10^{-9} \text{ m}^3 \text{s/kg}$, $3.60 \times 10^{-9} \text{ m}^3 \text{s/kg}$ and $5.60 \times 10^{-9} \text{ m}^3 \text{s/kg}$. The Cn number is 0.06.

3.4. CONCLUSIONS

This chapter focuses on modelling dry slug flow with the Phase Field method since dry slug flow involves the *Interface Breakup Problem* and *Moving Contact Line Problem*. In this chapter, monitoring the slug length provides a straightforward way to check if the *Interface Breakup Problem* is correctly modelled with the Phase Field method.

It is found that the results depend on the position of the initial interface. When $Ca < 1 \times 10^{-3}$ for the two phases, dry slug flow is expected in the simulations. However, when the initial interface is prescribed in the middle of the microfluidic channel, the flow pattern always belongs to the parallel flow, which does not agree with the experimental results. When the initial interface is prescribed at the Y-joint part of the microfluidic channel, the initial interface is distorted by the convective flow. In such a situation, the dynamics of the diffusive interface of the Phase Field method can be simulated correctly

and dry slug flow occurs as expected.

It is found that the slug length calculated with the Phase Field method is influenced by both the mobility parameter (M) and the capillary width (ϵ). Further research shows that the slug length is linearly proportional to the Pe^{-1} number and the Cn number when the Ca number of the two phases is smaller than 1×10^{-3} . In the microfluidic channel in this study, the dimensionless slug length follows the relationship: $\text{Slug length}/\text{Characteristic length} = 0.72CnPe^{-1} + 3.86$. To generate consistent slug length when the capillary width (ϵ) is varied, the mobility parameter (M) needs to be changed by following $CnPe^{-1} = \text{constant}$. In addition, one specific combination of the mobility parameter (M) and the capillary width (ϵ) has been found for which the slug length in the simulations agrees with that in the experiments.

REFERENCES

- 3
- [1] David Jacqmin. Calculation of two-phase Navier–Stokes flows using phase-field modeling. *Journal of Computational Physics*, 155(1):96 – 127, 1999.
 - [2] Pengtao Yue, James J. Feng, Chun Liu, and Jie Shen. A diffuse-interface method for simulating two-phase flows of complex fluids. *Journal of Fluid Mechanics*, 515:293–317, 2004.
 - [3] P. Yue and J. J. Feng. Can diffuse-interface models quantitatively describe moving contact lines? *The European Physical Journal Special Topics*, 197(1):37, Aug 2011.
 - [4] F. Magaletti, F. Picano, M. Chinappi, L. Marino, and C. M. Casciola. The sharp-interface limit of the Cahn–Hilliard/Navier–Stokes model for binary fluids. *Journal of Fluid Mechanics*, 714:95–126, 2013.
 - [5] David Jacqmin. Contact-line dynamics of a diffuse fluid interface. *J. Fluid Mech*, 402:57–88, 2000.
 - [6] V.V. Khatavkar, P.D. Anderson, and H.E.H. Meijer. On scaling of diffuse–interface models. *Chemical Engineering Science*, 61(8):2364 – 2378, 2006.
 - [7] Pengtao Yue, Chunfeng Zhou, and James J. Feng. Sharp-interface limit of the Cahn–Hilliard model for moving contact lines. *Journal of Fluid Mechanics*, 645:279–294, 2010.
 - [8] Mario De Menech. Modeling of droplet breakup in a microfluidic T-shaped junction with a phase-field model. *Phys. Rev. E*, 73:031505, Mar 2006.
 - [9] M. De Menech, P. Garstecki, F. Housse, and H. A. Stone. Transition from squeezing to dripping in a microfluidic T-shaped junction. *Journal of Fluid Mechanics*, 595:141–161, 2008.
 - [10] Harish Ganapathy, Ebrahim Al-Hajri, and Michael M. Ohadi. Phase field modeling of Taylor flow in mini/microchannels, Part II: Hydrodynamics of taylor flow. *Chemical Engineering Science*, 94:156 – 165, 2013.
 - [11] Harish Ganapathy, Ebrahim Al-Hajri, and Michael M. Ohadi. Phase field modeling of Taylor flow in mini/microchannels, Part I: Bubble formation mechanisms and phase field parameters. *Chemical Engineering Science*, 94:138 – 149, 2013.
 - [12] Feng Bai, Xiaoming He, Xiaofeng Yang, Ran Zhou, and Cheng Wang. Three dimensional phase-field investigation of droplet formation in microfluidic flow focusing devices with experimental validation. *International Journal of Multiphase Flow*, 93:130 – 141, 2017.
 - [13] Vyas Srinivasan and Sameer Khandekar. Thermo-hydrodynamic transport phenomena in partially wetting liquid plugs moving inside micro-channels. *Sādhāraṇā*, 42(4):607–624, Apr 2017.

- [14] Aurélien F. Stalder, Tobias Melchior, Michael Müller, Daniel Sage, Thierry Blu, and Michael Unser. Low-bond axisymmetric drop shape analysis for surface tension and contact angle measurements of sessile drops. *Colloids and Surfaces A: Physico-chemical and Engineering Aspects*, 364(1):72–81, 2010.
- [15] Xuan Cai. *Interface-Resolving Simulations of Gas-Liquid Two-Phase Flows in Solid Structures of Different Wettability*. PhD thesis, Karlsruher Institut für Technologie (KIT), 2016.

4

INVESTIGATING THE APPARENT CONTACT ANGLE OF SLUGS WITHIN A DOUBLE Y-SHAPED MICROFLUIDIC CHANNEL

4.1. INTRODUCTION

When utilizing the parallel microfluidic solvent extraction to purify ^{99}Mo , as has been illustrated in Figure 1.7, one of the practical problems is that it is difficult to avoid leakage from one phase to the other at the outlet of the microfluidic channel, leading to failure of the extraction. The leakage is related to the *Moving Contact Line*, *i.e.*, the movement of the interface between two immiscible phases at the solid surface. Until now, the physics behind the *Moving Contact Line* is not entirely clear [1] [2]. As introduced in Section 2.3, the difficulty in understanding the *Moving Contact Line* originates from the fact that physical phenomena at different length scales are involved. In general, it is believed that the multiphase flow in the microfluidic channel is governed by hydrodynamic theory at the macroscopic scale while the movement of the contact line needs to be described at the microscopic scale with the molecular-kinetic theory [3][4].

4

The Phase Field method attempts to integrate the hydrodynamic description and the molecular-kinetic description of the *Moving Contact Line* in one framework [5]. According to the continuum hypothesis in the hydrodynamic description of multiphase flows, the *Moving Contact Line* is not compatible with the no-slip boundary condition. Imposing the no-slip boundary condition on the wall, the stress and viscous dissipation became infinite at the moving contact line. From a mathematical point of view, the no-slip boundary condition brought a singularity to the moving contact line [6]. As introduced in Section 2.5, the Phase Field method approaches the *Moving Contact Line* by introducing a diffusive interface, to remove the singularity at the wall. The evolution of the order parameter (ϕ) of the Phase Field method within the diffusive interface reflects the molecular-kinetic description of the *Moving Contact Line*.

Concerning simulating leakage at the outlet of the microfluidic channel¹, with the equilibrium contact angle boundary condition (Equation 2.39 with $\mu_f = 0 \text{ Pa} \cdot \text{s}$) used in Chapter 3, the leakage does not appear as that of the experimental results. These simulation results indicate that the physics of the *Moving Contact Line* is not modelled correctly with the equilibrium contact angle boundary condition. Thus, this chapter simulates the *Moving Contact Line* with the non-equilibrium contact angle boundary condition first proposed by Jacqmin [7][8]. It sets the contact line friction parameter (μ_f in Equation 2.39) to a positive value, to allow for a slower relaxation of the free energy at the wall. It has been found by Carlson *et al.* that the application of such a boundary condition results in more physical results in capturing the droplet spreading process in the Phase Field simulation [9] [10]. However, not all mechanisms of the non-equilibrium contact angle boundary condition are fully understood. As a consequence, it is not clear if this boundary condition is universally applicable in other multiphase flows [5].

Hence, this chapter is dedicated to the question of whether the non-equilibrium contact angle boundary condition can capture some of the aspects of the *Moving Contact Line*. The *Moving Contact Line* can be characterized by the contact angle formed between the interface and the solid wall [1]. As introduced in Figure 1.5, in dry slug flow, there are two

¹The leakage will be further discussed in Chapter 6

apparent contact angles (θ_{app}), *i.e.*, the advancing contact angle (θ_A) and the receding contact angle (θ_R) of the slug. In general, due to the movement of the contact line, the advancing contact angle (θ_A) would be larger than the equilibrium contact angle (θ_e) while the receding contact angle (θ_R) would be smaller than the equilibrium contact angle (θ_e) [2]. Besides the contact angle, the velocity of the *Moving Contact Line* is also an important aspect to check if the *Moving Contact Line* is correctly simulated.

Thus, by investigating dry slug flow of the n-heptane/water system, this chapter aims to clarify the effect of the non-equilibrium contact angle boundary condition on the *Moving Contact Line*. To the best of the author's knowledge, this is the first time that the non-equilibrium contact angle boundary condition is imposed on dry slug flow in microfluidics. The objectives of this study are: firstly, investigating the apparent contact angles (θ_{app}) of the n-heptane slugs in terms of the Ca_f number of the fluids when the non-equilibrium contact angle boundary condition is applied. Secondly, this chapter studies the effect of the Phase Field parameters (*i.e.*, capillary width and mobility parameter) on the apparent contact angles (θ_{app}) and the velocity of the slugs. Lastly, comparing the simulation results with the experimental results, this chapter determines the value of the contact line friction parameter (μ_f), to provide guidelines for simulating the leakage phenomenon at the outlet of the microfluidic channel in Chapter 6.

4.2. MATERIALS AND METHODS

4.2.1. MICROFLUIDIC CHIP AND EXPERIMENTAL PROCEDURE

The microfluidic chip (IMT ICC-DY05, Material: borosilicate glass) and working fluids were the same as those in Chapter 3. The microfluidic channel was double Y-shaped with two inlets and two outlets. Its two inlets were connected to two syringes (1 mL, Inkjet-F BD) separately by capillary tubings (PEEK, Length: 25 cm, ID: 0.26 mm). The syringes were driven by two Aladdin single-syringe pumps (WPI).

The experimental procedure was also the same as that in Chapter 3. The microfluidic chip was firstly rinsed with ethanol for around ten minutes. After rinsing with the ethanol, the whole system was flushed with Milli-Q water for around ten minutes. During the measurement, at each flow rate, the whole microfluidic system was first pumped with the aqueous solution. After making sure that there was no gas bubble in the microfluidic system, then the organic solution was pumped into the microfluidic channel. In the experiments, Milli-Q water served as the aqueous solution and n-heptane served as the organic solution.

4.2.2. GOVERNING EQUATIONS AND BOUNDARY CONDITIONS

The governing equations for multiphase flows in the microfluidic channel were the Cahn-Hilliard equation (Equation 2.23), the continuity equation (Equation 2.2) as well as the Navier-Stokes momentum equations (Equation 2.24). A two-dimensional model was built in COMSOL Multiphysics according to the geometry of the microfluidic chip. At

the two inlets, the average velocity of the fluids was prescribed as boundary conditions. The average velocity was calculated based on the volumetric flow rates of fluids and the cross-sectional area of the inlet of the microfluidic chip (the geometry of the microfluidic chip is shown in Table 3.1). The velocity profile was assumed to be fully developed since the fluid needed to flow through a capillary tubing (Length: 25 cm) in the experiments. A reference pressure (Pressure = 0 Pa) was added as the boundary condition at the outlets and the no-slip boundary condition was imposed at the solid wall. The meshing details and convergence criteria are the same as those of Section 3.2.5.

The contact angle boundary condition was different from the one in Chapter 3. In Chapter 3, Equation 2.39 was adopted for the contact angle boundary condition by setting the value of the contact line friction parameter (μ_f) to zero. In this case, the apparent contact angle (θ_{app}) in the simulations was forced to reach the equilibrium contact angle (θ_e) immediately. In this chapter, the influence of the contact line friction parameter (μ_f) is taken into account by setting μ_f to a positive value.

4.2.3. DERIVATION OF THE EQUILIBRIUM CONTACT ANGLE AND APPARENT CONTACT ANGLE

In the experiments, n-heptane is the dispersed phase, forming n-heptane slugs, see Figure 3.4. In order to investigate the relationship between the apparent contact angle (θ_{app}) and the equilibrium contact angle (θ_e) of n-heptane slugs, it is necessary to measure the equilibrium contact angle (θ_e) of an n-heptane droplet in bulk water on a glass surface. However, such measurement is not possible because the density of water is higher than that of n-heptane. Due to the buoyancy effect, the n-heptane droplet floats on the surface of water. Instead, the θ_e of n-heptane can be determined by taking the supplementary angle of θ_e of a water droplet in bulk n-heptane. The θ_e of a water droplet in bulk n-heptane is 47° as measured in Section 3.2.2. Thus, the θ_e of n-heptane in bulk water on a glass surface is $180^\circ - 47^\circ = 133^\circ$. Thus, if there is no further notification, $\theta_e = 133^\circ$ in this chapter.

As the dispersed phase moves along the microfluidic channel, the contact angle which is measured macroscopically is called the apparent contact angle (θ_{app}). Furthermore, as demonstrated in Figure 4.1, the apparent contact angles (θ_{app}) at the front and back of the dispersed slug are termed the "advancing contact angle (θ_A)" and "receding contact angle (θ_R)", respectively. In the experiments, the apparent contact angle (θ_{app}) was measured directly from the images captured by the high-speed camera, using the drop analysis plug-in package of the image processing program ImageJ. The drop analysis package calculates the contact angle based on Young-Laplace fit [11], which is the same as the method used in Section 3.2.2 to measure the equilibrium contact angle (θ_e). In the simulations, the apparent contact angle (θ_{app}) was also derived from the drop analysis package of ImageJ, by analyzing the digital images of the n-heptane slugs.

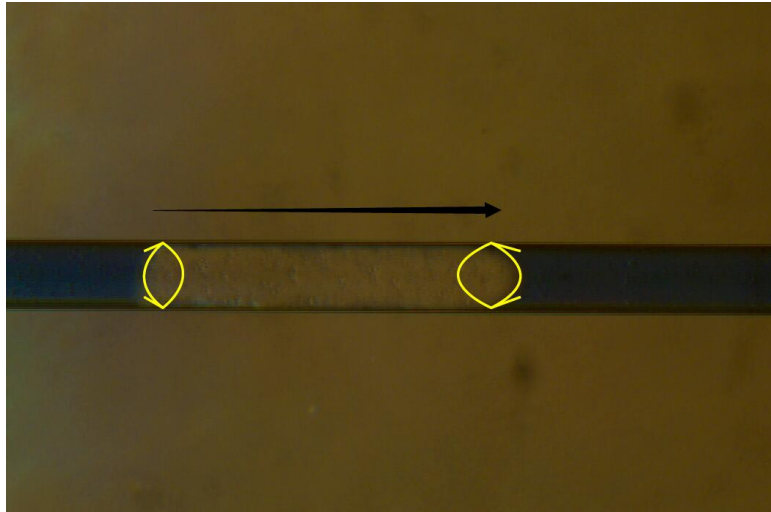


Figure 4.1: Schematic diagram of measurement of the apparent contact angles (θ_{app}) of the n-heptane slug with ImageJ. The arrow indicates the direction of the flow.

4.3. RESULTS AND DISCUSSION

4.3.1. INFLUENCE OF THE CA NUMBER ON THE APPARENT CONTACT ANGLES IN THE SIMULATIONS

This section focuses on the influence of the equilibrium contact angle boundary condition and the non-equilibrium contact angle boundary condition on the advancing contact angle (θ_A) and the receding contact angle (θ_R) of the slugs in the Phase Field method. The Ca number has been used to describe the apparent contact angle (θ_{app}) forming at the moving contact line [1][2][4]. Thus, the simulation results in this section are investigated in terms of the Ca number of the fluids.

As introduced in Section 2.5.4, the Cn number indicates the relative thickness of the capillary width (ϵ) of the diffusive interface to the characteristic length (L) of the microfluidic system. In the simulations, the Cn number is set to 0.06 and the mobility parameter (M) is set to $3.60 \times 10^{-9} \text{ m}^3/\text{s}/\text{kg}$. As determined in Section 3.3.4, with this combination of the Cn number and mobility parameter (M), the slug length in the simulations agrees with that in the experiments in the n-heptane/water system.

Figure 4.2 and Figure 4.3 present the advancing contact angle (θ_A) and the receding contact angle (θ_R) of the n-heptane slugs respectively, as a function of the Ca number of n-heptane and the contact line friction parameter (μ_f). The solid symbols in Figures 4.2 and 4.3 represent the case where the Ca number of n-heptane is varied by changing the volumetric flow rates. When the volumetric flow rates are changed, the volumetric flow

rates of the two phases are always kept equal ($\Phi_{aq} = \Phi_{org}$) and the corresponding Re number of n-heptane ranges from 0.37 to 6.61. In this process, the coefficient of interfacial tension is a constant ($\sigma = 50.2 \text{ mN/m}$). Since the flow rates of the two phase are always equal, the Ca number of water can also be used if necessary. The open symbols in Figures 4.2 and 4.3 represent the case where the Ca number of n-heptane is varied by changing the coefficient of interfacial tension (σ). When changing the coefficient of interfacial tension (σ), the volumetric flow rates of both phases are kept as $2.0 \mu\text{L}/\text{min}$ and the corresponding Re number of n-heptane is 1.47.

When the contact line friction parameter (μ_f) is set to zero (indicating the equilibrium contact angle boundary condition is imposed), both the advancing contact angle (θ_A) and the receding contact angle (θ_R) equal the equilibrium contact angle ($\theta_e = 133^\circ$), showing no dependency on the Ca number of n-heptane, see Figure 4.2 and Figure 4.3. In such a situation, the simulations do not show the contact angle hysteresis, which does not agree with the experimental observation in Figure 4.9.

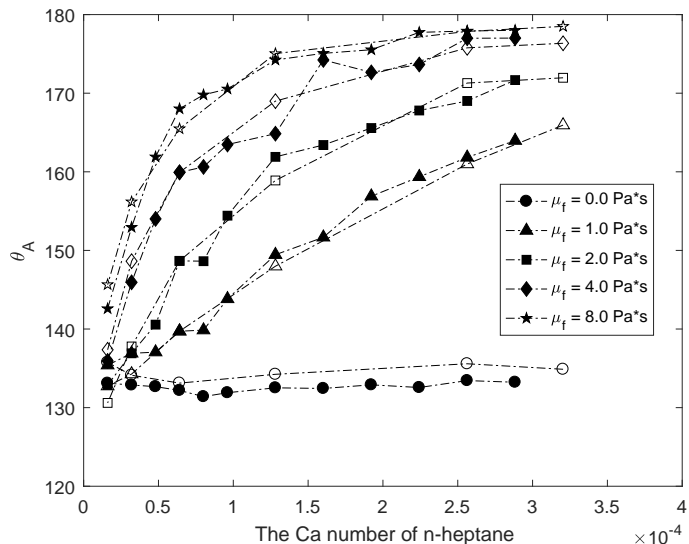


Figure 4.2: Influence of the Ca number of n-heptane on the advancing contact angle (θ_A) of the slugs. $Cn = 0.06$, $M = 3.60 \times 10^{-9} \text{ m}^3/\text{s/kg}$, $\theta_e = 133^\circ$. The solid symbols denote that the Ca number is varied by changing the volumetric flow rates of the two phases. The open symbols denote that the Ca number is varied by changing the coefficient of interfacial tension (σ).

When imposing the non-equilibrium contact angle boundary condition by setting μ_f to a positive value, it cannot be known a priori what the value of μ_f should be. By comparing the experimental results with the Phase Field simulation results of the droplet spreading, Carlson *et al.* found that the value of μ_f of a water droplet is $0.15 \text{ Pa}\cdot\text{s}$ while

the value of μ_f of a glycerin-water droplet is $1.02 \text{ Pa} \cdot \text{s}$ [10]. In this study of dry slug flow, the value of μ_f is varied from $1.0 \text{ Pa} \cdot \text{s}$ to $8.0 \text{ Pa} \cdot \text{s}$. When the contact line friction parameter (μ_f) is set to a positive constant, it is clear that both the advancing contact angle (θ_A) and the receding contact angle (θ_R) deviate from the equilibrium contact angle (θ_e) in Figure 4.2 and Figure 4.3. Furthermore, the advancing contact angle (θ_A) is larger than the equilibrium contact angle (θ_e) while the receding contact angle (θ_R) is smaller than the equilibrium contact angle (θ_e). Such results agree with the observation of the contact angle hysteresis in nature [1][2].

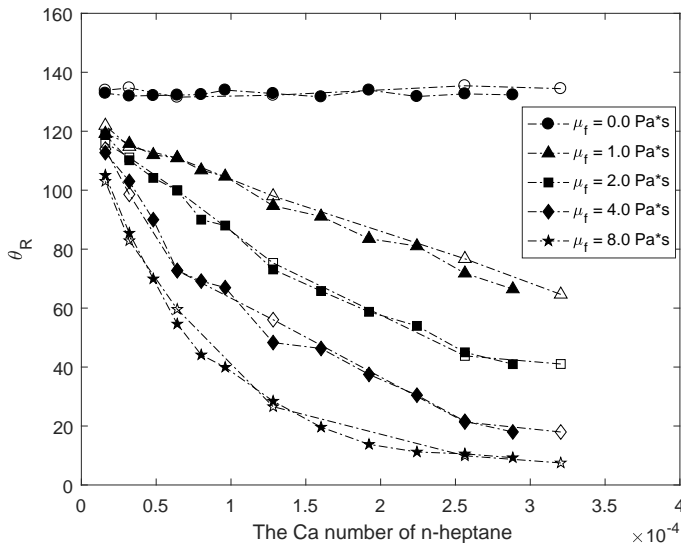


Figure 4.3: Influence of the Ca number of n-heptane on the receding contact angle (θ_R) of the slugs. $Cn = 0.06$, $M=3.60 \times 10^{-9} \text{ m}^3/\text{kg}$, $\theta_e = 133^\circ$. The solid symbols denote that the Ca number is varied by changing the volumetric flow rates of the two phases. The open symbols denote that the Ca number is varied by changing the coefficient of interfacial tension (σ).

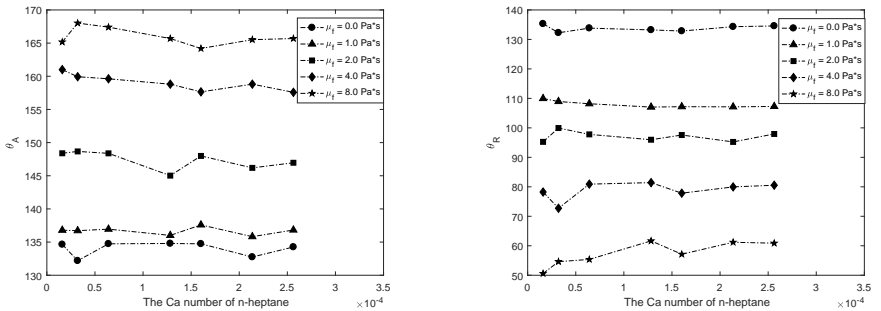
The influence of μ_f on the results in Figure 4.2 and Figure 4.3 can be explained by the evolution of the order parameter (ϕ). As mentioned in Section 2.5, the order parameter (ϕ) needs to relax to the equilibrium stable state, to minimize the free energy (E_{free}). Based on Equation 2.15, the free energy (E_{free}) equals the sum of the mixing energy (E_{mix}) between two fluids and the wall surface free energy (E_{wall}). When μ_f is set to zero, the equilibrium state of the wall surface free energy (E_{wall}) is reached immediately [7][8]. As a result, both the advancing contact angle (θ_A) and the receding contact angle (θ_R) are forced to be equal to the equilibrium contact angle (θ_e). This is the reason that Equation 2.39 with $\mu_f = 0$ is denoted as the equilibrium contact angle boundary condition. When μ_f is set to a positive value, the wall surface free energy (E_{wall}) does not immediately reach the equilibrium state. This means μ_f exhibits a delaying effect on the

relaxing process of the wall surface free energy [12]. Focusing on the deviation between the apparent contact angle (*i.e.*, θ_A and θ_R) and the equilibrium contact angle (θ_e) in Figure 4.2 and Figure 4.3, when the value of μ_f is fixed and larger than zero, the apparent contact angle (θ_{app}) varies with the Ca number, both by variation of the coefficient of interfacial tension (σ) and the volumetric flow rates. These results indicate that the convective flow (represented by the U_{org} in the nominator of the Ca number) tends to distort the apparent contact angle (θ_{app}) from the equilibrium contact angle (θ_e) while the coefficient of interfacial tension (represented by the σ in the denominator of the Ca number) tries to keep the apparent contact angle (θ_{app}) at the equilibrium contact angle (θ_e). In addition, when the value of μ_f is constant, the convective flow distorts the shape of the interface, forming an apparent contact angle (θ_{app}) that deviates from the prescribed equilibrium contact angle (θ_e). On the other hand, the interfacial tension tries to keep the the apparent contact angles (θ_{app}) at the prescribed equilibrium contact angle (θ_e).

4

Figure 4.4 demonstrates the influence of the Ca number on the apparent contact angles (θ_{app}) by varying the dynamic viscosity. In the simulations, the mobility parameter (M) is set to $3.60 \times 10^{-9} \text{ m}^3/\text{s}/\text{kg}$ and the Cn number is 0.06, which are the same as those in Figure 4.2 and Figure 4.3. The volumetric flow rates of both phases are $2.0 \mu\text{L}/\text{min}$ and the coefficient of interfacial tension is a constant ($\sigma = 50.2 \text{ mN/m}$). When varying the dynamic viscosity, the dynamic viscosity ratio of the two phases is kept constant (*i.e.*, $\frac{\mu_{aq}}{\mu_{org}} = \text{constant}$). In Figure 4.4, it is seen that varying the Ca number by the dynamic viscosity does influence the apparent contact angles (both θ_A and θ_R). Based on the experimental investigation of the apparent contact angle of a liquid-liquid-solid system where glycerin serves as the advancing fluid and silicone oil as the receding fluid in a glass capillary tube, *Fermigier and Jenffer* found that the dynamic viscosity of the receding fluid is not an influencing factor in determining the apparent contact angle when the Ca number is small ($Ca < 1 \times 10^{-2}$) [13]. The simulation results in Figure 4.4 indicate that, when the dynamic viscosity ratio is kept constant, the dynamic viscosity of neither phase determines the apparent contact angles (θ_{app}) of the slugs.

From the simulation results of Figures 4.2, 4.3 and 4.4, it can be concluded that for dry slug flow ($Ca < 1 \times 10^{-3}$), with the equilibrium contact angle boundary condition ($\mu_f = 0 \text{ Pa} \cdot \text{s}$ in Equation 2.39), neither the advancing contact angle (θ_A) nor the receding contact angle (θ_R) deviate from the equilibrium contact angle (θ_e). With the non-equilibrium contact angle boundary condition ($\mu_f > 0 \text{ Pa} \cdot \text{s}$ in Equation 2.39), physically meaningful contact angle hysteresis is observed, *i.e.*, $\theta_A > \theta_e$ and $\theta_R < \theta_e$. In addition, it is found that the volumetric flow rate, coefficient of interfacial tension as well as the contact line friction parameter (μ_f) determine the apparent contact angle (θ_{app}) and their joint effect which will be discussed in Section 4.3.2



(a) The advancing contact angle (θ_A) of the n-heptane slugs.

(b) The receding contact angle (θ_R) of the n-heptane slugs.

Figure 4.4: Influence of the *Ca* number on the apparent contact angles of the n-heptane slugs when changing the *Ca* number by the dynamic viscosity. $Cn = 0.06$, $M=3.60 \times 10^{-9} \text{ m}^3/\text{kg}$, $\theta_e = 133^\circ$. $\frac{\mu_{aq}}{\mu_{org}} = \text{constant}$.

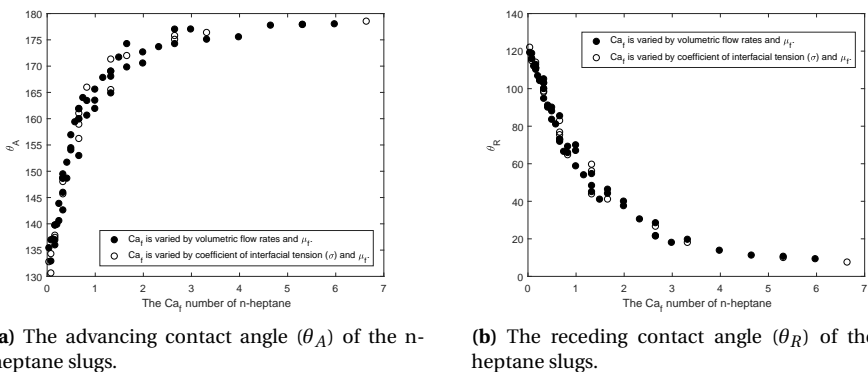
4.3.2. INFLUENCE OF THE Caf NUMBER ON THE APPARENT CONTACT ANGLES

Based on the simulation results of Section 4.3.1, it is found that by imposing the non-equilibrium contact angle boundary condition ($\mu_f > 0 \text{ Pa}\cdot\text{s}$ in Equation 2.39), the apparent contact angles (θ_{app}) of the slugs are allowed to deviate from the prescribed equilibrium contact angle (θ_e). According to Figures 4.2 Figure 4.3, when the *Ca* number of n-heptane is the same, while the value of μ_f is increased, the deviation between the apparent contact angles (θ_{app}) and the equilibrium contact angle (θ_e) becomes larger. Obviously, the value of the contact line friction parameter (μ_f) influences the apparent contact angles (θ_{app}). This section investigates the role of the contact line friction parameter (μ_f) in determining the apparent contact angle (θ_{app}) of the n-heptane slugs.

Figure 4.5a and 4.5b present the advancing contact angle (θ_A) and receding contact angle (θ_R) of the n-heptane slugs in terms of the Caf number ($Caf = \frac{\mu_f U_{org}}{\sigma}$, as defined in Equation 2.46) of n-heptane. The Caf number of the aqueous phase can also be used if necessary. The data in Figure 4.5a are directly extracted from Figure 4.2 while the data in Figure 4.5b are extracted from Figure 4.3. Focusing on the advancing contact angle (θ_A) of the slugs in Figure 4.5a, the solid symbols represent the case that the Caf number of n-heptane is varied by changing the volumetric flow rates ($U_{org}=U_{aq}$ in this process) and μ_f ($1.0 \text{ Pa}\cdot\text{s} \leq \mu_f \leq 8.0 \text{ Pa}\cdot\text{s}$). The open symbols represent that the Caf number of n-heptane is varied by changing the coefficient of interfacial tension (σ) and μ_f ($1.0 \text{ Pa}\cdot\text{s} \leq \mu_f \leq 8.0 \text{ Pa}\cdot\text{s}$).

In Figure 4.5a, it is found that the advancing contact angle (θ_A) becomes a function of the Caf number of n-heptane. Besides, to generate the same advancing contact angle

(A), it is equivalent to varying the three variables (U_{org} , σ and μ_f) in the Caf number. The simulation results in Figure 4.5b show that the receding contact angle (θ_R) is also determined by the Caf number. In Section 4.3.1, it has been shown that when μ_f is set to a positive value, μ_f exhibits a delaying effect on the relaxing process of the wall surface free energy (E_{wall}) [12]. Since the apparent contact angles (θ_{app}) are determined by the Caf number, it can be understood as that the relaxing process of the wall surface free energy behaves like viscous stress at the three-phase moving contact line. The results in Figure 4.5a and 4.5b indicate that the "viscous stress at the three-phase moving contact line" and the convective flow deforms the shape of the interface, enlarging the deviation between the apparent contact angles (θ_{app}) and the equilibrium contact angle (θ_e). The interfacial tension keeps the apparent contact angles (θ_{app}) at the equilibrium contact angle (θ_e). It can be concluded that for dry slug flow ($Ca < 1 \times 10^{-3}$) in the Phase Field method, when the equilibrium contact angle (θ_e) is fixed, the apparent contact angles (θ_{app}) are determined by the Caf number of the system. Increasing the Caf number results in a larger deviation between the apparent contact angles (θ_{app}) and the equilibrium contact angle (θ_e).



(a) The advancing contact angle (θ_A) of the n-heptane slugs.

(b) The receding contact angle (θ_R) of the n-heptane slugs.

Figure 4.5: Influence of the Caf number on the apparent contact angle (θ_{app}) of the n-heptane slugs. $Cn = 0.06$. $M = 3.60 \times 10^{-9} \text{ m}^3/\text{kg}$. $\theta_e = 133^\circ$. The solid symbols denote that the Caf number is varied by changing the volumetric flow rates and the contact line friction parameter (μ_f). The open symbols denote that the Caf number is varied by changing the coefficient of interfacial tension (σ) and the contact line friction parameter (μ_f).

4.3.3. INFLUENCE OF THE VALUE OF THE EQUILIBRIUM CONTACT ANGLE ON THE APPARENT CONTACT ANGLES

Section 4.3.2 has revealed that when the value of the equilibrium contact angle (θ_e) is a constant, the apparent contact angle (θ_{app}) is determined by the Caf number. This section focuses on the influence of the prescribed value of the equilibrium contact angle

(θ_e) on the apparent contact angles (θ_{app}) of the n-heptane slugs.

Figure 4.6 shows the difference between the apparent contact angle (θ_{app}) and the equilibrium contact angle (θ_e) as a function of the Ca_f number of n-heptane. The advancing contact angle (θ_A) is always larger than the equilibrium contact angle (θ_e), and the difference is defined as: $\Delta\theta_{app} = \Delta\theta_A = \theta_A - \theta_e$. The receding contact angle (θ_R) is smaller than the equilibrium contact angle (θ_e), and the difference is defined as: $\Delta\theta_{app} = |\Delta\theta_R| = |\theta_R - \theta_e|$. The squares represent $\theta_e = 133^\circ$, the data of which are extracted from Figures 4.5a and 4.5b. The circles represent $\theta_e = 90^\circ$ and the simulation conditions are the same as those of $\theta_e = 133^\circ$, i.e., the Ca_f number of n-heptane is varied by changing the volumetric flow rates and μ_f . The volumetric flow rates of the two phases are always kept equal ($\Phi_{aq} = \Phi_{org}$) and the corresponding Re number of n-heptane ranges from 0.37 to 6.61. The coefficient of interfacial tension is a constant ($\sigma = 50.2 \text{ mN/m}$) and the μ_f is varied from $1.0 \text{ Pa}\cdot\text{s}$ to $8.0 \text{ Pa}\cdot\text{s}$. The Cn number is 0.06 and the mobility parameter (M) is $3.60 \times 10^{-9} \text{ m}^3\text{s/kg}$.

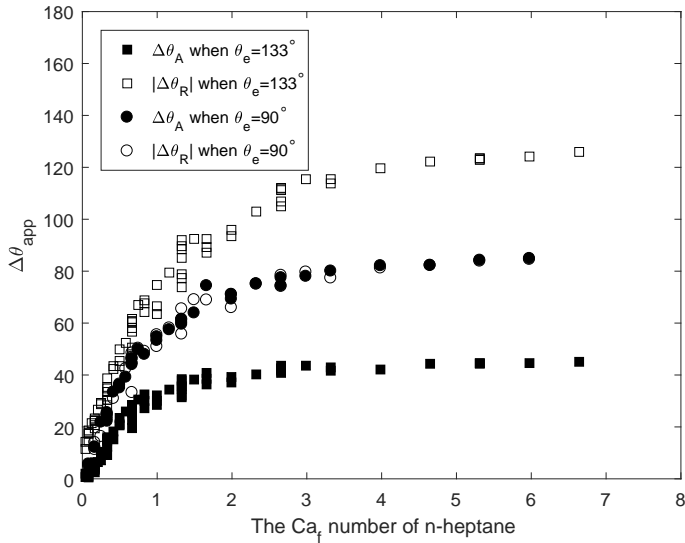


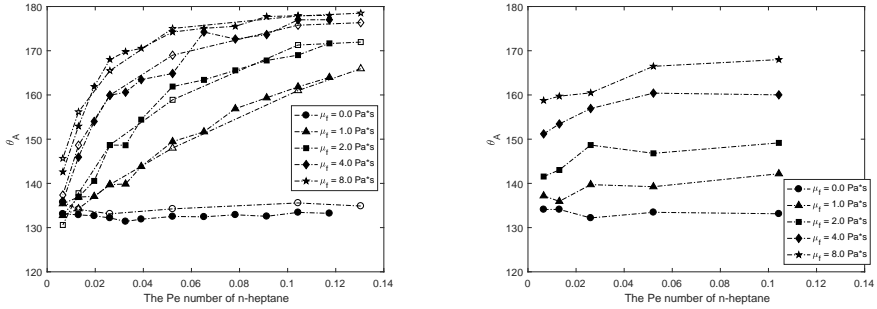
Figure 4.6: Influence of the Ca_f number and θ_e on the $\Delta\theta_{app}$ of the n-heptane slugs. The Ca_f number of n-heptane is varied by changing the volumetric flow rates and μ_f . $Cn = 0.06$, and $M = 3.60 \times 10^{-9} \text{ m}^3\text{s/kg}$. The solid symbols denote $\Delta\theta_{app} = \Delta\theta_A = \theta_A - \theta_e$ while the open symbols denote $\Delta\theta_{app} = |\Delta\theta_R| = |\theta_R - \theta_e|$.

For $\theta_e = 133^\circ$, with constant Ca_f number of the n-heptane, it is found that $|\Delta\theta_R|$ is always larger than $\Delta\theta_A$. However, in the case of $\theta_e = 90^\circ$, $|\Delta\theta_R|$ is always equal to $\Delta\theta_A$ when the Ca_f number is constant. Clearly, $\Delta\theta_{app}$ is also determined by the value of θ_e . Focusing on the $\Delta\theta_A$ when $\theta_e = 133^\circ$ and $\theta_e = 90^\circ$, it is found that the $\Delta\theta_A$ of $\theta_e = 90^\circ$ is always larger than that of $\theta_e = 133^\circ$. On the other hand, the $\Delta\theta_R$ of $\theta_e = 90^\circ$ is always smaller

than that of $\theta_e = 133^\circ$. With simulating dry slug flow with the Phase Field method, the $\Delta\theta_{app}$ is determined by the difference between θ_e and 180° (for θ_A) or 0° (for θ_R). The larger the difference, the larger the $\Delta\theta_{app}$. When $\theta_e = 133^\circ$, $|\Delta\theta_R|$ is always larger than $\Delta\theta_A$ with the same Ca_f number. In addition, when $\theta_e = 90^\circ$ at the same Ca_f number, the advancing contact angle (θ_A) and the receding contact angle (θ_R) differ from the equilibrium contact angle (θ_e) at the same magnitude.

4.3.4. INFLUENCE OF THE PE NUMBER AND THE CN NUMBER ON THE APPARENT CONTACT ANGLES

In Section 4.3.1, the mobility parameter (M) and capillary width (ϵ) are kept constant in the simulations. This section focuses on the influence of these two parameters on the apparent contact angles (θ_{app})



(a) The solid symbols denote that the Pe number is varied by changing the volumetric flow rates of the two phases. The open symbols denote that the Pe number is varied by changing the coefficient of interfacial tension (σ). $M=3.60 \times 10^{-9} \text{ m}^3/\text{kg}$.

(b) The Pe number is varied by changing the mobility parameter (M).

Figure 4.7: Influence of the Pe number on the advancing contact angle (θ_A) of the n-heptane slugs. $Cn = 0.06$, and $\theta_e = 133^\circ$.

Figure 4.7a presents the advancing contact angle (θ_A) as a function of the Pe number of n-heptane. The simulation conditions are the same as those of Figure 4.2: the mobility parameter (M) is $3.60 \times 10^{-9} \text{ m}^3/\text{kg}$ and the Cn number is 0.06. The solid symbols indicate that the Pe number of n-heptane is varied by changing the volumetric flow rates (keeping $\Phi_{aq} = \Phi_{org}$) and keeping the coefficient of interfacial tension constant ($\sigma = 50.2 \text{ mN/m}$). The open symbols indicate that the Pe number of n-heptane is varied by changing the coefficient of interfacial tension (σ). The volumetric flow rates of both phases are set to $2.0 \mu\text{L}/\text{min}$ and the corresponding Ca number of both phases is always smaller than 1×10^{-3} .

Figure 4.7b shows the advancing contact angle (θ_A) as a function of the n-heptane slugs (varied by changing the mobility parameter (M)). In the simulations, the volumetric flow rates of both phases are $2.0\mu\text{L}/\text{min}$, the coefficient of interfacial tension is a constant ($\sigma = 50.2\text{mN/m}$) and the Cn number is 0.06. It can be seen that the advancing contact angle (θ_A) is much less sensitive to the mobility parameter (M), compared to the case in Figure 4.7a. For instance, in the case of $\mu_f = 1.0\text{ Pa}\cdot\text{s}$, when the Pe number is varied from 6.52×10^{-3} to 1.4×10^{-1} by changing the mobility parameter (M), the advancing contact angle (θ_A) changes from 137° to 142° (by 3.6%). As a comparison, when the Pe number is varied in the same range by changing the flow rates in Figure 4.7a, the corresponding advancing contact angle (θ_A) changes from 133° to 161° (by 21.1%).

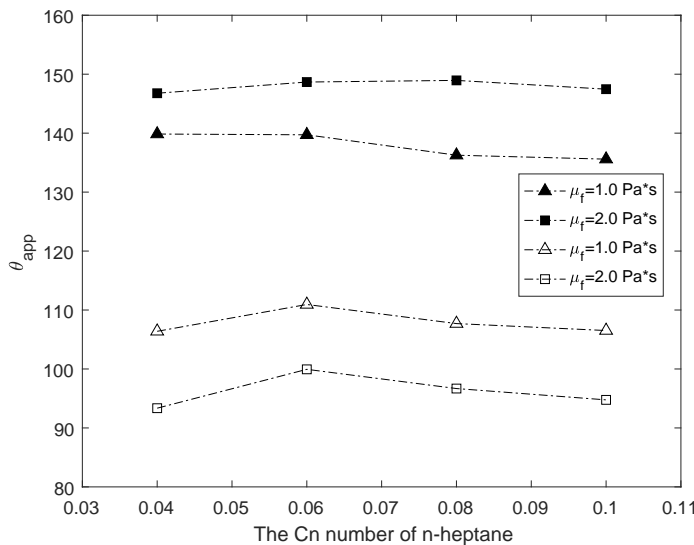


Figure 4.8: The apparent contact angles (θ_{app}) as a function of the Cn number of the n-heptane slugs. The solid symbols denote the advancing contact angle (θ_A) and the open symbols denote the receding contact angle (θ_R). $\theta_e = 133^\circ$. The Pe number of n-heptane is 0.026.

Concerning the influence of the Cn number on the apparent contact angles (θ_{app}), Figure 4.8 demonstrates the apparent contact angles (θ_{app}) of the n-heptane slugs. The volumetric flow rates of both phases are $2.0\mu\text{L}/\text{min}$ and the coefficient of interfacial tension (σ) is 50.2mN/m . The corresponding Ca number of n-heptane is 6.41×10^{-5} and the corresponding Re number of n-heptane is 1.47. When ϵ is varied, M is also changed accordingly, to keep the Pe number of n-heptane constant at 0.026. Based on the simulation results of Figure 4.8, as the Cn number varied from 0.04 to 0.1, neither the advancing contact angle (θ_A) nor the receding contact angle (θ_R) shows significant change.

In Chapter 3, it has been shown that both the capillary width (ϵ) and the mobility parameter (M) affect the slug length in dry slug flow. To generate consistent slug length

when the capillary width (ϵ) is varied, the mobility parameter (M) needs to be changed by following $CnPe^{-1} = \text{constant}$. Unlike the slug length, based on the results of Figure 4.7b and 4.8, the mobility parameter (M) and capillary width (ϵ) do not bring noticeable influence on the apparent contact angles (θ_{app}) of the n-heptane slugs in dry slug flow. Thus, concerning the choice of the numerical parameters for simulating the dry slug flow with the Phase Field method, it can be concluded that the capillary width (ϵ) and the mobility parameter (M) influence the slug length and the contact line friction parameter (μ_f) influences the apparent contact angles (θ_{app}).

4.3.5. COMPARING SIMULATION RESULTS OF THE APPARENT CONTACT ANGLE WITH THE EXPERIMENTAL RESULTS

Section 4.3.1 has shown that by setting the contact line friction parameter (μ_f) to a positive value, the apparent contact angle (θ_{app}) deviates from the equilibrium contact angle (θ_e). This section focuses on comparing the apparent contact angle (θ_{app}) in the simulations with the experimental results, to study if the non-equilibrium contact angle boundary condition simulates the apparent contact angles (θ_{app}) in dry slug flow correctly.

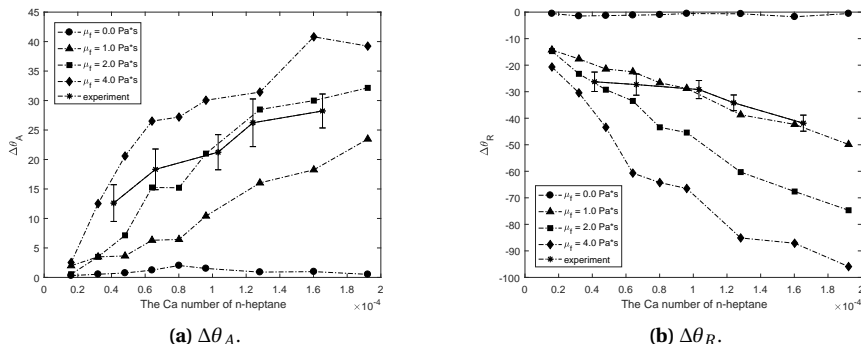


Figure 4.9: Comparing $\Delta\theta_{app}$ in the experiments with those in the simulations. The Ca number of n-heptane is varied by changing the flow rates. The asterisks with error bars represent the experimental results with the standard deviation. In the simulations, $Cn = 0.06$ and $M=3.60 \times 10^{-9} \text{ m}^3/\text{kg}$.

Figure 4.9 presents the experimental results as well as the simulation results of $\Delta\theta_A$ and $\Delta\theta_R$ with respect to the Ca number of n-heptane. In the experiments, the Ca number of n-heptane is varied by changing the volumetric flow rates of n-heptane and water, while the volumetric flow rates of the two phases are kept the same. The $\Delta\theta_A$ and $\Delta\theta_R$ have been derived from the average results of 7 slugs at the same experimental conditions. In the simulations, the Ca number of n-heptane is varied by changing the volumetric flow rates of n-heptane and water. In this process, the volumetric flow rates of these two

phases are kept the same. The Cn number is 0.06 and the mobility parameter (M) is set to $3.60 \times 10^{-9} \text{ m}^3 \text{s/kg}$, which are the same as those of Figure 4.2 and Figure 4.3. For the deviation of the advancing contact angle ($\Delta\theta_A$), the simulation results of $\mu_f = 2.0 \text{ Pa}\cdot\text{s}$ is mostly resembling the experimental results while for the deviation of receding contact angle ($\Delta\theta_R$), the simulation results of $\mu_f = 1.0 \text{ Pa}\cdot\text{s}$ fit the experimental results better. Thus, it can be considered that for fitting the experimental results of dry slug flow of the n-heptane/water system, the value of the contact line friction parameter (μ_f) ranges from $\mu_f = 1.0 \text{ Pa}\cdot\text{s}$ to $\mu_f = 2.0 \text{ Pa}\cdot\text{s}$.

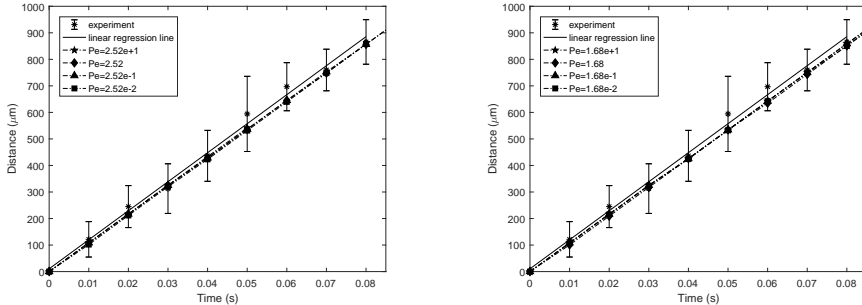
4.3.6. INFLUENCE OF THE NUMERICAL PARAMETERS ON THE VELOCITY OF THE SLUGS

As mentioned in Section 4.1, besides the apparent contact angles (θ_{app}), monitoring the velocity of the three-phase moving contact line is another way to verify if the *Moving Contact Line* is correctly simulated. Thus, this section investigates the velocity of the slugs in the simulations, especially the influence of the numerical parameters (capillary width and mobility parameter) with the equilibrium or non-equilibrium contact angle boundary conditions.

The investigation is carried out by comparing the velocity of the n-heptane slugs in the experiments with that in the simulations. In the experiments, the flow rates of both phases are $1.0 \mu\text{L}/\text{min}$. The corresponding Ca number of the aqueous phase is 1.07×10^{-4} while the Ca number of n-heptane is 4.13×10^{-5} . As introduced in Section 3.2.3, such small Ca number ensures that the flow pattern belongs to dry slug flow. A camera recorded the distance of the moving n-heptane slugs to a reference position with respect to time. The distance of the n-heptane slugs to the reference position is derived from the average distance of 7 slugs. Figure 4.10 shows the experimental results of the temporal evolution of the distance to the reference position with the asterisk symbol. The slope of the linear regression line is $1.09 \times 10^{-2} \text{ m/s}$, which can be considered as the average velocity of the n-heptane slugs.

In the simulations, the Ca number of the two phases is the same as that of the experiments by controlling the flow rates. The contact line friction parameter (μ_f) is set to zero, *i.e.*, the equilibrium contact angle boundary condition is applied. The Pe number is varied by changing the mobility parameter (M) while keeping other parameters constant. In Figure 4.10a, the Cn number is 0.04 and the Cn number is 0.06 in Figure 4.10b. In the simulations, the velocity of the n-heptane slugs is derived by finding the slope of the linear regression line, which is the same as deriving the velocity of the n-heptane slugs in the experiments. In Figure 4.10a, in the case of $Cn = 0.04$, when the Pe number is varied from 2.52×10^{-2} to 25.2 by changing the mobility parameter (M), the simulated velocity ranges from $1.06 \times 10^{-3} \text{ m/s}$ to $1.08 \times 10^{-3} \text{ m/s}$, hence with a deviation less than 2 %. The situation is similar in Figure 4.10b when the Cn number is 0.06. Thus, concerning the simulated velocity in Figure 4.10, it can be concluded that neither the capillary width (ϵ) nor the mobility parameter (M) brings significant influence on the velocity of the slugs.

when μ_f is zero. Furthermore, the difference between the velocity in the simulation and that in the experiment is less than 2.8 %. Therefore, it can be concluded that the simulation results agree well with the experimental results.



(a) The C_n number is 0.04. The star, diamond, triangle and square symbols denote the Pe numbers are set to 2.52×10^1 , 2.52 , 2.52×10^{-1} and 2.52×10^{-2} by varying the mobility parameter (M). $\mu_f=0.0\text{Pa}\cdot\text{s}$.

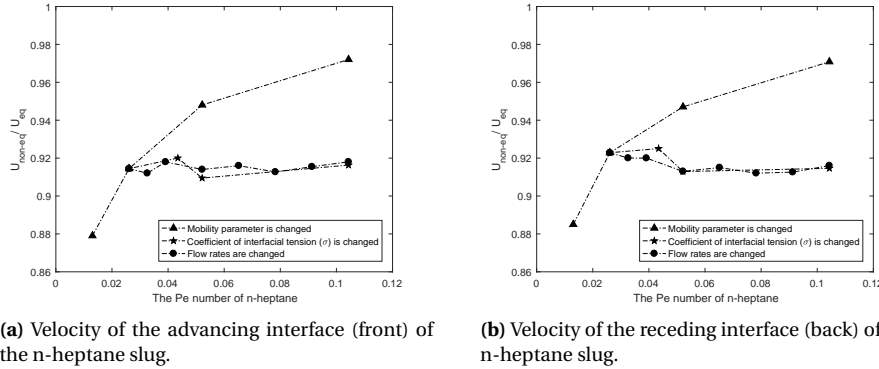
(b) The C_n number is 0.06. The star, diamond, triangle and square symbols denote the Pe numbers are set to 1.68×10^1 , 1.68 , 1.68×10^{-1} and 1.68×10^{-2} by varying the mobility parameter (M). $\mu_f=0.0\text{Pa}\cdot\text{s}$.

Figure 4.10: Temporal evolution of the distance of the n-heptane slugs to the reference position. The corresponding Ca number of the aqueous phase is 1.07×10^{-4} while the Ca number of n-heptane is 4.13×10^{-5} . The asterisks with error bars represent the experimental results with the standard deviation. The coefficient of determination (R^2) of the linear regression line is 0.9943.

However, in Figure 4.11, when the non-equilibrium contact angle boundary condition is imposed by setting μ_f to a positive value, it is found that the mobility parameter (M) influences the velocity of the slugs. In Figure 4.11, the C_n number is kept as 0.06 and μ_f is set to $1.0\text{Pa}\cdot\text{s}$. The Pe number of n-heptane is varied by changing the mobility parameter (M), the coefficient of interfacial tension (σ) or the flow rates of the two phases. When the Pe number is varied by changing the mobility parameter (M) or the coefficient of interfacial tension, the flow rates of both phases are kept constant. When the Pe number of n-heptane is varied by changing the volumetric flow rates, the volumetric flow rates of these two phases are always kept the same. The corresponding Pe number of n-heptane is plotted on the horizontal axis and the ratio of the velocity with $\mu_f > 0.0\text{Pa}\cdot\text{s}$ to the velocity with $\mu_f = 0.0\text{Pa}\cdot\text{s}$ (U_{non-eq}/U_{eq}) is plotted on the vertical axis.

In Figure 4.11a, when $\mu_f=1.0\text{Pa}\cdot\text{s}$, the velocity of the advancing interface of the slugs in the simulations is always lower than that in the experiments. When the Pe number of n-heptane is varied from 1.30×10^{-2} to 1.04×10^{-1} by changing the mobility parameter (M), the velocity of the advancing interface changes from 87.9 % to 97.2 % of the velocity with the equilibrium contact angle boundary condition. The situation is the same for the receding interface of the slugs in Figure 4.11b. On the other hand, when changing the

Pe number of n-heptane by varying the coefficient of interfacial tension (σ) or the flow rates, the velocity of the slugs does not change significantly. Thus, among the three variables varied in Figure 4.11, only the mobility parameter (M) determines the slow down effect of the velocity of the slugs when the non-equilibrium contact angle boundary condition is applied. The higher the value of the mobility parameter (M), the slower the slug moves.



(a) Velocity of the advancing interface (front) of the n-heptane slug.

(b) Velocity of the receding interface (back) of the n-heptane slug.

Figure 4.11: Influence of the *Pe* number on the velocity of the n-heptane slugs when the non-equilibrium contact angle boundary condition is applied. The *Cn* number is 0.06. $\mu_f = 1.0 \text{ Pa} \cdot \text{s}$.

Figure 4.12a demonstrates the influence of the *Cn* number on the velocity of the advancing interface of the n-heptane slugs when $1.0 \text{ Pa} \cdot \text{s}$. In Figure 4.12a, the flow rates of both phases are $1.0 \mu\text{L}/\text{min}$. The *Pe* number of n-heptane is set to 0.013 by adjusting the mobility parameter (M). In Figure 4.12a, as the *Cn* number is increased, the slug moves slower. Figure 4.12b shows the influence of the contact line friction parameter (μ_f) on the velocity of the advancing interface of the n-heptane slugs. The *Cn* number is 0.06 and the flow rates of both phases are kept as $1.0 \mu\text{L}/\text{min}$. The *Pe* number of n-heptane is changed by varying the mobility parameter (M). Figure 4.12b presents the simulation results of setting μ_f to $1.0 \text{ Pa} \cdot \text{s}$ and $2.0 \text{ Pa} \cdot \text{s}$. The simulation results of $\mu_f=1.0 \text{ Pa} \cdot \text{s}$ are extracted from Figure 4.11a. In Figure 4.12b, at the same *Pe* number, the velocity of the slug when $\mu_f=2.0 \text{ Pa} \cdot \text{s}$ is always smaller than that of $\mu_f=1.0 \text{ Pa} \cdot \text{s}$.

Based on the results of this section, when the equilibrium contact angle boundary condition is applied, the velocity of the slug shows no dependency on the numerical parameters (capillary width and mobility parameter). However, when the non-equilibrium contact angle boundary condition is imposed, according to Figure 4.11, Figure 4.12a and Figure 4.12b, the n-heptane slug moves slower, compared with applying the equilibrium contact angle boundary condition. The higher the value of the numerical parameters (capillary width, mobility parameter and contact line friction parameter), the slower the n-heptane slug moves. According to Carlson *et al.*, a similar slowing down effect has also been found in simulating droplet spreading process with the non-equilibrium con-

tact angle boundary condition [10] and the mechanism behind that is still not clear [12]. Further work is needed to address this issue.

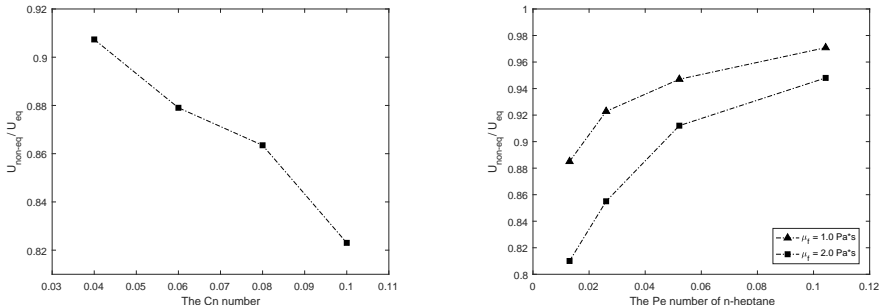


Figure 4.12: Influence of the capillary width (ϵ) and the contact line friction parameter (μ_f) on the velocity of the n-heptane slugs. The flow rates of both phases are $1.0 \mu\text{L}/\text{min}$.

4.4. CONCLUSIONS

When utilizing the parallel microfluidic solvent extraction to purify ^{99}Mo , in the experiments in Chapter 6, there can be leakage from one phase to the other at the outlet of the microfluidic channel, leading to failure of the extraction. However, the leakage can not be simulated correctly with the widely applied equilibrium contact angle boundary condition in the Phase Field method. The leakage involves the so-called *Moving Contact Line*, which can be characterized by the apparent contact angle (θ_{app}) formed between the interface and the wall. This chapter deals with the question of whether the Phase Field method can model the apparent contact angle (θ_{app}) of the *Moving Contact Line* correctly with the non-equilibrium contact angle boundary condition first proposed by *Jacqmin* [7][8]. In order to study this boundary condition, the case of dry slug flow is chosen since dry slug flow provides a direct way to monitor the apparent contact angles (θ_{app}).

For dry slug flow ($Ca < 1 \times 10^{-3}$) in the simulations, by imposing the equilibrium contact angle boundary condition, the apparent contact angle (θ_{app}) is always equal to the equilibrium contact angle (θ_e). In such a situation, the *Moving Contact Line* has no effect on the apparent contact angle (θ_{app}). With the non-equilibrium contact angle boundary condition, the apparent contact angle (θ_{app}) deviates from the equilibrium contact angle (θ_e). Furthermore, in the case of dry slug flow, the simulated advancing contact angle (θ_A) is larger than the equilibrium contact angle (θ_e) while the receding contact angle

(θ_R) is smaller than the equilibrium contact angle (θ_e) , which fulfils the observation of contact angle hysteresis in nature.

Furthermore, this research shows that the apparent contact angle (θ_{app}) of the slugs is determined by the Ca_f number of the system. This is equivalent to varying the three variables (U_{org} , σ and μ_f) in the Ca_f number to generate the same apparent contact angle (θ_{app}) . These results indicate that, with the non-equilibrium contact angle boundary condition, the convective flow deforms the shape of the interface and leads to a difference between the apparent contact angles (θ_{app}) and the equilibrium contact angle (θ_e) . The interfacial tension tries to keep the apparent contact angles (θ_{app}) at the equilibrium contact angle (θ_e) . With the contact line friction parameter (μ_f) in the range between 1.0 and 2.0 Pa·s, the apparent contact angles (θ_{app}) of the slugs in the simulations reasonably agree with those in the experiments.

4

Besides the Ca_f number, it is found that the value of the equilibrium contact angle (θ_e) influences the magnitude of the deviation between the apparent contact angle (θ_{app}) and the equilibrium contact angle (θ_e) in dry slug flow. When the Ca_f number is fixed, $\Delta\theta_{app}$ is determined by the difference between θ_e and 180° (for θ_A) or 0° (for θ_R).

Regarding the velocity of the slugs, with the equilibrium contact angle boundary condition, it does not depend on the capillary width or the mobility parameter. In this case, the velocity of the slugs in the simulations agree with that in the experiments. With the non-equilibrium contact angle boundary condition, the slug moves slower with the increase of the value of the numerical parameters (capillary width, the mobility parameter and contact line friction parameter), which conflicts with the experiments.

REFERENCES

- 4
- [1] Daniel Bonn, Jens Eggers, Joseph Indekeu, Jacques Meunier, and Etienne Rolley. Wetting and spreading. *Rev. Mod. Phys.*, 81:739–805, May 2009.
 - [2] Terence D. Blake. The physics of moving wetting lines. *Journal of Colloid and Interface Science*, 299(1):1 – 13, 2006.
 - [3] Jacco H. Snoeijer and Bruno Andreotti. Moving contact lines: Scales, regimes, and dynamical transitions. *Annual Review of Fluid Mechanics*, 45(1):269–292, 2013.
 - [4] Yi Sui, Hang Ding, and Peter D.M. Spelt. Numerical simulations of flows with moving contact lines. *Annual Review of Fluid Mechanics*, 46(1):97–119, 2014.
 - [5] P. Yue and J. J. Feng. Can diffuse-interface models quantitatively describe moving contact lines? *The European Physical Journal Special Topics*, 197(1):37, Aug 2011.
 - [6] Chun Huh and L.E Scriven. Hydrodynamic model of steady movement of a solid/liquid/fluid contact line. *Journal of Colloid and Interface Science*, 35(1):85 – 101, 1971.
 - [7] David Jacqmin. Calculation of two-phase Navier–Stokes flows using phase-field modeling. *Journal of Computational Physics*, 155(1):96 – 127, 1999.
 - [8] David Jacqmin. Contact-line dynamics of a diffuse fluid interface. *J. Fluid Mech.*, 402:57–88, 2000.
 - [9] A. Carlson, M. Do-quang, and G. Amberg. Dissipation in rapid dynamic wetting. *Journal of Fluid Mechanics*, 682:213–240, 2011.
 - [10] A. Carlson, G. Bellani, and G. Amberg. Contact line dissipation in short-time dynamic wetting. *Europhysics Letters*, 97(4):44004, feb 2012.
 - [11] Aurélien F. Stalder, Tobias Melchior, Michael Müller, Daniel Sage, Thierry Blu, and Michael Unser. Low-bond axisymmetric drop shape analysis for surface tension and contact angle measurements of sessile drops. *Colloids and Surfaces A: Physico-chemical and Engineering Aspects*, 364(1):72–81, 2010.
 - [12] Pengtao Yue and James J. Feng. Wall energy relaxation in the Cahn–Hilliard model for moving contact lines. *Physics of Fluids*, 23(1):012106, 2011.
 - [13] Marc Fermigier and Patrice Jenffer. An experimental investigation of the dynamic contact angle in liquid-liquid systems. *Journal of Colloid and Interface Science*, 146(1):226 – 241, 1991.

5

INVESTIGATING FLOW PATTERNS INSIDE A DOUBLE Y-SHAPED MICROFLUIDIC CHANNEL WITH PHASE FIELD METHOD

5.1. INTRODUCTION

In microfluidic liquid-liquid solvent extraction, the small-scale feature of microfluidic channels reduces the diffusion distance for solutes, which ensures high extraction efficiency [1]. Besides the high extraction efficiency, in the parallel flow pattern, the automatic phase separation at the outlet of the microfluidic channel is also advantageous in extracting radionuclides because it reduces radiation exposure to operators [2]. The working principle of the microfluidic liquid-liquid solvent extraction for ^{99}Mo has been briefly demonstrated in Figure 1.6. For the purpose of utilizing parallel microfluidic liquid-liquid solvent extraction to purify ^{99}Mo , a stable interface is of paramount importance. A stable interface means the interface between the immiscible two phases is always parallel to the main channel, as depicted in Figure 1.6. An unstable interface may break, forming segmented flow and leading to contamination of the extracted ^{99}Mo . Thus, the flow pattern should be maintained to the parallel flow pattern.

5

However, until now, there are no clear criteria that are available for accurately predicting flow patterns in microfluidic channels [3]. One of the reasons for the difficulty in predicting flow patterns is that there are lots of influencing factors to be taken into account. The geometry and fabrication material of the microfluidic channel [4] [5] as well as the physical properties of the working fluids [6] have been reported to be influencing factors on flow patterns. Moreover, operating conditions, including the volumetric flow rates of phases as well as their ratio [7] [8] and which fluid is first injected into the microfluidic channel [9] are also found to affect flow patterns.

Researchers have tried to predict flow patterns with dimensional analysis in terms of fluid forces. The *Reynolds* number ($Re = \frac{\rho UL}{\mu}$), the *Capillary* number ($Ca = \frac{\mu U}{\sigma}$) and the *Weber* number ($We = \frac{\rho U^2 L}{\sigma}$), or the combination of these dimensionless numbers are all reported to be used for predicting flow patterns [6] [10] [11] [12] [13] [14] [15] [16] [17] [18]. Nevertheless, these analysis are all limited to their specific flow conditions and are not universally applicable [18]. For example, *Tice et al.* have studied the influence of liquid viscosity on plug formation in the microfluidic channel. They have proposed to use the *Ca* number to predict flow patterns [11]. *Dessimoz et al.* have predicted the flow patterns within a Y-shaped and a T-shaped microfluidic channel with the mean *Ca* number and the mean *Re* number of the fluids. [6]. However, by investigating flow patterns inside a T-shaped microfluidic channel, *Guillot and Colin* have found that the flow patterns can not be expressed in terms of the *Ca* number [12]. Besides the *Ca* number, the *We* number has also been proposed to predict the flow patterns. *Zhao et al.* have investigated the flow patterns with water and kerosene inside a PMMA T-shaped channel. They have found that parallel flow is formed at higher values of the *We* number and have concluded that the flow patterns are attributed to the competition between the inertia force and the interfacial tension [10].

Besides the competition between fluid forces, the contact angle has also been reported to affect multiphase flows in microfluidics [19] [20] [21]. *Bashir et al.* have studied the

droplet formation in a T-shaped microfluidic channel and have reported that the droplet length is influenced by the contact angle [22]. *Zhao et al.* have changed the contact angle of the fluids inside a T-shaped PMMA microfluidic channel with surface modification. They have found that the parallel flow pattern is more likely to occur after surface modification. For the purpose of selective extraction, extractants are usually added in the organic solution [1], which change the fluid property, leading to the change of the contact angle.

For modelling parallel flow in microfluidic channels within hydrodynamics-based simulation methods, even though the Volume-of-Fluid method is more widely being used [13] [21] [23] [24] [25], the Phase Field method has the advantage of being compatible with the no-slip boundary condition in continuum fluid dynamics so that no special treatments are required [26]. This chapter deals with the parallel flow pattern in a double Y-shaped microfluidic channel with the Phase Field method, and aims to utilize the method as a numerical tool to understand the occurrence of parallel flow. The objectives of the present work are: firstly, to determine the mobility parameter (M) and the capillary width (ϵ) in modelling parallel flow. Based on the study of dry slug flow in Chapter 3, to generate consistent slug length, it needs to set up the numerical parameters by following $CnPe^{-1} = \text{constant}$. This work will examine whether such a scaling law still holds in modelling parallel flow. Secondly, by combining the Phase Field method with experiments based on the toluene/water system and the n-heptane/water system, this study aims to reveal the dominating force that determines the occurrence of parallel flow inside the microfluidic chip under investigation here. Lastly, with help of the Phase Field method, this study clarifies when the interface is located in the centre of the main channel, the influence of the contact angle between the liquids and the wall on flow patterns.

5.2. MATERIALS AND METHODS

The experiments of investigating flow patterns were conducted in the IMT ICC-DY05 double Y-shaped microfluidic chip, the geometry and fabrication material of which can be found in Section 3.2.1. In the experiments, Milli-Q water served as the aqueous phase. Toluene and n-heptane, which were purchased from Sigma Aldrich, served as the organic phase. The experiments also included the mixture of toluene and Aliquat 336 (purchased from Sigma Aldrich). Aliquat 336 is a water insoluble quaternary ammonium salt with octyl and decyl chains. The choice of the mixture of toluene and Aliquat 336 in this study is: firstly, adding Aliquat 336 to toluene can change the equilibrium contact angle (θ_e) between water and toluene on a glass surface. Secondly, it has been reported that Aliquat 336 is able to extract uranium(VI) from HCl media [27] [28] [29]. As introduced in Section 1.2.3, recovering the non-fissioned ^{235}U from the fission products in the loop system is meaningful, which ensures that the ^{235}U can be better consumed.

Physical properties (density, dynamic viscosity, coefficient of interfacial tension and equilibrium contact angle) of the fluids related to this research served as input parameters in the simulations. Section 5.2.1 briefly introduces the measurement of the physical properties of the fluids which can not be found in literature.

5.2.1. MEASUREMENT OF PHYSICAL PROPERTY OF FLUIDS

The equilibrium contact angle (θ_e) between water and toluene on a glass surface was measured with the same method which has been introduced in Section 3.2.2. The macro cuvette with a glass surface (described in Section 3.2.2) served as the container of the bulk solution. The equilibrium contact angle of the water droplet in the bulk toluene solution was measured to be $49^\circ \pm 5^\circ$, the measurement of which was repeated 6 times. Figure 5.1a illustrates a picture of the water droplet in the bulk toluene solution, which is taken by the camera of the CAM 200 instrument. Besides, Figure 5.1b illustrates one water droplet in the bulk toluene solution (in which 0.1 mol/L Aliquat 336 is dissolved) on a glass surface. It is clear that by adding Aliquat 336, the equilibrium contact angle (θ_e) of water in Figure 5.1b is larger than 90° , which indicates that the organic solution preferentially wetting the glass surface of the macro cuvette. The measured equilibrium contact angle (θ_e) with respect to the concentration of Aliquat 336 in toluene is plotted in Figure 5.2. The results in Figure 5.2 indicate that the equilibrium contact angle (θ_e) does not show noticeable dependency on the concentration of Aliquat 336 in the range from 0.1 mol/L to 0.4 mol/L.

Measurement of the coefficient of interfacial tension (σ) between water and the mixture of toluene and Aliquat 336 was also conducted with the CAM 200 instrument (KSV Instruments Ltd., Finland), with the pendant drop method. The CAM 200 instrument measures the coefficient of interfacial tension (σ) based on the deformation of the droplet by gravity and the interfacial tension. At equilibrium, the shape of the pendant drop obeys the Young–Laplace Equation. The built-in software of the CAM 200 instrument determines the coefficient of interfacial tension (σ) by iterative fitting the Young–Laplace Equation [30].

The macro cuvette served as the container of the bulk toluene solution (or the mixture of toluene and Aliquat 336). One water droplet was provided by the pipette tip. The coefficient of interfacial tension (σ) between water and pure toluene was measured first, as a benchmark test. The measurement was repeated more than 5 times and the measured value was 34.3 ± 2.3 mN/m, which was considered to agree with the value found in literature (listed in Table 5.1). Figure 5.3a illustrates the shape of water droplet in pure bulk toluene solution. When Aliquat 336 was added to the toluene solution, the shape of the water droplet changed accordingly, which is demonstrated in Figure 5.3b. The measured coefficient of interfacial tension (σ) with respect to the concentration of Aliquat 336 is demonstrated in Figure 5.4. In Figure 5.4, as the concentration of Aliquat 336 is varied from 0.1 mol/L to 0.4 mol/L, the coefficient of interfacial tension (σ) does not change significantly.



(a) One water droplet in bulk toluene solution on a glass surface.

(b) One water droplet in the mixture solution of toluene and Aliquat 336 (in which the concentration of Aliquat 336 is 0.1 mol/L) on a glass surface.

5

Figure 5.1: Measurement of the equilibrium contact angle (θ_e) of one water droplet in bulk toluene solution on a glass surface. The macro cuvette serves as the container of the bulk solution. In Figure 5.1a, the equilibrium contact angle (θ_e) is smaller than 90° while the equilibrium contact angle (θ_e) in Figure 5.1b is larger than 90° .

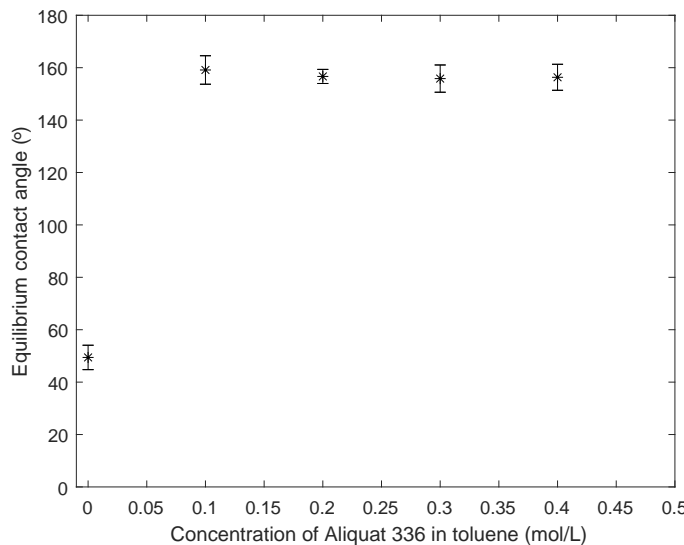


Figure 5.2: Measurement of the equilibrium contact angle (θ_e) of one water droplet in bulk toluene solution (in which Aliquat 336 is dissolved) on a glass surface.



(a) One water droplet in pure bulk toluene solution.

(b) One water droplet in the mixture solution of toluene and Aliquat 336 (in which the concentration of Aliquat 336 is 0.4 mol/L).

5

Figure 5.3: Measurement of the coefficient of interfacial tension (σ) of one water droplet in bulk toluene solution with the pendant drop method in the experiments. Due to the larger interfacial tension, the water droplet in Figure 5.3a is rounder compared with the one in Figure 5.3b.

The dynamic viscosity of the mixture solution of toluene and Aliquat 336 was measured using a rheometer (TA Instruments, AR-G2) with 40 mm parallel plate. However, it was found that, among all the samples, only the mixture with Aliquat 336 concentration of 0.4 mol/L could reach the lowest measurement limit of the rheometer. Thus, the mixture with Aliquat 336 concentration of 0.4 mol/L was chosen as the working fluid in the experiments and the measured dynamic viscosity is listed in Table 5.1. In Table 5.1, the fluid "tol+Aliquat" indicates the mixture of toluene and Aliquat 336 in which the concentration of Aliquat 336 is 0.4 mol/L. The abbreviation will be used in the following text. In addition, the coefficient of interfacial tension (σ) indicates the σ between the organic phase and water.

Table 5.1: Physical properties of fluids in the simulations

Fluids	Viscosity (Pa · s)	Density (g/cm ³)	σ (mN/m)	θ_e
Water	1×10^{-3}	1		
n-heptane	3.86×10^{-4}	0.68	50.2	$47^\circ \pm 4^\circ$
toluene	5.86×10^{-4}	0.87	36.1	$49^\circ \pm 5^\circ$
tol+Aliquat	$(1.22 \pm 0.05) \times 10^{-3}$	0.95	5.7 ± 0.7	$156^\circ \pm 5^\circ$

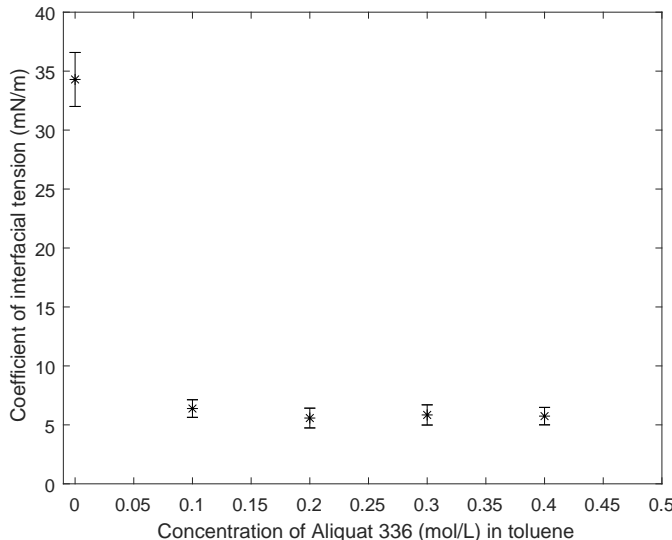


Figure 5.4: Measurement of the coefficient of interfacial tension (σ) between water and mixture solution of toluene and Aliquat 336.

5.2.2. EXPERIMENTAL PROCEDURE

The experimental procedure was the same as those introduced in Section 3.2.1: before the experiments, the microfluidic chip was rinsed by ethanol for around ten minutes to clean. Then, the whole system was flushed by Milli-Q water for around ten minutes. After making sure that there was no gas bubble in the microfluidic system, the organic solution was pumped into the microfluidic channel. The volumetric flow rates were varied in the experiments, to study the flow patterns.

5.2.3. MODEL DESCRIPTION AND SIMULATION SETUP

In the simulations, the governing equations were the Cahn-Hilliard equation (Equation 2.23), the continuity equation (Equation 2.2) and the Navier-Stokes momentum equations (Equation 2.24) for multiphase flows. These equations have been introduced in detail in Section 2.5.

In COMSOL, based on the geometry of the microfluidic channel as introduced in Table 3.1, a 2-dimensional model was built. To save the computational effort, the length of the main channel was set to 2000 μm , which was shorter than the one used in the experiments (see Table 3.1). This change was made based on the research that the channel length starts to influence flow patterns when it is longer than 4 m [5]. At the two inlets, the average velocity of the fluids was prescribed as boundary conditions. The average velocity was calculated based on the volumetric flow rates of fluids and the cross-

sectional area of the inlet of the microfluidic chip (the geometry of the microfluidic chip is shown in Table 3.1). The velocity profile was assumed to be fully developed since the fluid needed to flow through a capillary tubing (Length: 25 cm) in the experiments. At the two outlets, a reference pressure (Pressure = 0 Pa) was used as the boundary condition. At the solid wall, the no-slip boundary condition was imposed and Equation 2.39 with $\mu_f = 0 \text{ Pa} \cdot \text{s}$ was adopted for the contact angle boundary condition.

5.3. RESULTS AND DISCUSSION

The experiments concerning the flow patterns were conducted in the IMT double Y-shaped microfluidic chip with the toluene/water system, the n-heptane/water system and the tol+Aliquat/water system, respectively. In the experiments, the volumetric flow rates of both phases were varied and three flow patterns appeared, namely the segmented flow pattern, the parallel flow pattern and the transition flow pattern. Features of these flow patterns have already been introduced in Section 3.3.1.

5

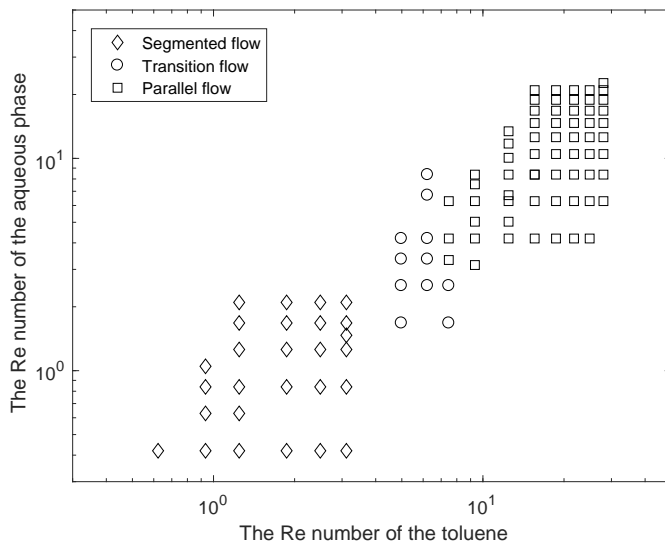


Figure 5.5: Flow pattern map of the toluene/water system in the IMT double Y-shaped microfluidic chip. The diamonds, circles and squares denote the segmented flow, the transition flow and the parallel flow pattern, respectively.

The experimental results of the flow patterns by varying the volumetric flow rates of the toluene/water system in the microfluidic chip are plotted in Figure 5.5 based on the Re number of each phase. The Re number of each phase is calculated based on the average velocity of the fluid at the inlet of the microfluidic channel. The average velocity was calculated based on the volumetric flow rate of the fluid and the cross-sectional area

of the inlet of the microfluidic chip. In Figure 5.5, it has been shown that the segmented flow pattern occurs when the volumetric flow rates of both phases are low. By increasing the volumetric flow rates, the segmented flow pattern eventually changes to the parallel flow pattern. The parallel flow pattern is maintained when the *Re* number of toluene is larger than approximately 10 while the *Re* number of the aqueous phase is larger than approximately 5. Section 5.3.1 will study the influence of the numerical parameters on the flow patterns. In this case, Figure 5.5 will serve as the benchmark for comparing the numerical results with the experimental results.

5.3.1. INFLUENCE OF THE MOBILITY PARAMETER AND CAPILLARY WIDTH ON FLOW PATTERNS

As been introduced in Section 2.5, in the Phase Field method, the capillary width (ϵ , a numerical parameter) determines the thickness of the diffusive interface and the mobility parameter (M , a numerical parameter) determines the diffusive transport of the order parameter (ϕ). Besides, these two adjustable parameters also affect the simulation results. By investigating the slug length inside the microfluidic channel in Chapter 3, it has been found to generate constant slug length in dry slug flow, it is necessary to choose these two numerical parameters by following $CnPe^{-1} = \text{constant}$. This section investigates if such a criterion is still valid in modelling the occurrence of parallel flow in the microfluidic channel.

The investigation starts with the influence of the mobility parameter (M) on the flow pattern. For this purpose, a simulation model is built based on the toluene/water system in the IMT microfluidic chip. The physical properties of the fluids and the equilibrium contact angle are adopted from Table 5.1. The initial interface is prescribed at the Y-joint part of the microfluidic channel, as illustrated in Figure 3.12b. Such a choice agrees with the experimental procedure in Section 5.2.2 where the aqueous phase was first pumped into the microfluidic channel.

In the simulations, the volumetric flow rate ratio (Φ_{aq}/Φ_{org}) of the aqueous phase to toluene is kept at 0.66. Such a choice is based on positioning the interface in the centre of the main channel, which is beneficial for obtaining complete phase separation at the outlet of the microfluidic channel¹. Pohar *et al.* proposed an empirical correlation for positioning of the interface in the centre of the microfluidic channel [31]:

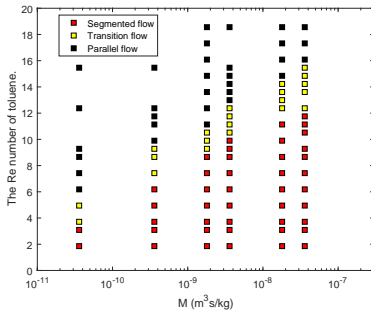
$$\frac{\Phi_{aq}}{\Phi_{org}} = \left(\frac{\mu_{aq}}{\mu_{org}} \right)^{-0.76} \quad (5.1)$$

where Φ_{aq} and Φ_{org} represent the volumetric flow rate of the aqueous phase and the organic phase, respectively. μ_{aq} and μ_{org} denote the dynamic viscosity of the aqueous phase and the organic phase, respectively. By filling in the viscosity of toluene and water, the volumetric flow rate ratio of $\Phi_{aq}/\Phi_{org}=0.66$ is derived.

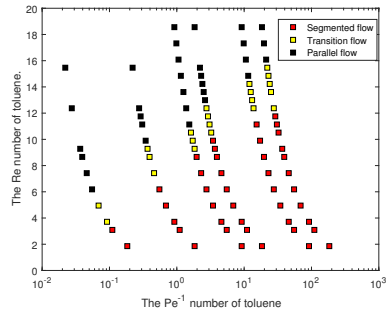
¹The complete phase separation will be further discussed in Chapter 6

Concerning the influence of the mobility parameter (M) on the flow pattern, the Cn number is fixed at 0.06, to ensure the calculation time is affordable (within a few hours). The volumetric flow rates and the mobility parameter (M) are varied in the simulations. The simulation results are plotted in Figure 5.6a with colors to distinguish different flow patterns. The mobility parameter (M) is plotted on the horizontal axis and the Re number of toluene is plotted on the vertical axis. The Re number is varied because of the change of the volumetric flow rate. Since the volumetric flow rate ratio (Φ_{aq}/Φ_{org}) of the aqueous phase to toluene is kept at 0.66, the Re number of the aqueous phase can be calculated if needed. When the value of the mobility parameter (M) is fixed and the volumetric flow rates are increased (the Re number increased accordingly), the flow pattern first changes from segmented flow, to transition flow and then to parallel flow. Such a tendency agrees with the experimental results in Figure 5.5 where the parallel flow pattern is more likely to occur when the Re numbers are high.

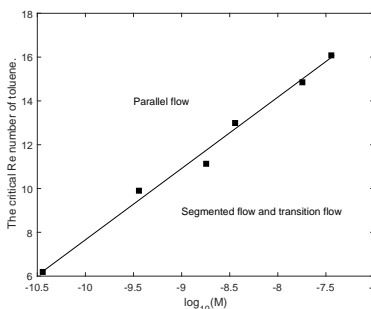
5



(a) The flow pattern map as as function of the mobility parameter (M) and the Re number of toluene.



(b) The flow pattern map as as function of the Pe^{-1} number and the Re number of toluene.



(c) The relationship between the critical Re number of toluene and the mobility parameter (M). The R^2 of the linear regression line is 0.9844.

Figure 5.6: Simulation results of the influence of the mobility parameter (M) on flow patterns. The red, yellow and black colors denote segmented flow, transition flow and parallel flow, respectively. The Cn number is 0.06.

To further study the influence of the mobility parameter (M) on the flow patterns, the simulation results in Figure 5.6a have been plotted in term of the Pe^{-1} number and the Re number in Figure 5.6b. In Section 3.3.2, it finds that to obtain the same slug length in dry slug flow, it is equivalent to varying the volumetric flow rate and the mobility parameter (M). As a result, the Pe^{-1} number determines the slug length when the Cn number is constant. In modelling the occurrence of parallel flow, the focus is given to the critical Re number (the first time that the parallel flow occurs by increasing the flow rates). However, in Figure 5.6b, when the mobility parameter (M) is varied in the Pe^{-1} number, the critical Re number is not the same. In other words, the critical Re number of interest in this study does not show a clear dependence on the Pe^{-1} number.

In addition, Figure 5.6c only plots the critical Re number at different values of mobility parameter (M), which are directly extracted from Figure 5.6a. In Figure 5.6c, when the value of the mobility parameter (M) becomes larger, the critical Re number of toluene shifts to a higher value. Focusing on the relationship between the critical Re number and the mobility parameter (M), the critical Re number of toluene approximately linearly scales to the common logarithm (logarithm with base 10) of the mobility parameter (M), *i.e.*, $Re_{critical} \propto \log_{10} M$.

Considering the influence of the capillary width (ϵ) on the flow patterns, the simulation results are plotted in Figure 5.7. The Cn number ($Cn = \frac{\epsilon}{L}$) is plotted on the horizontal axis while the Re number of toluene is plotted on the vertical axis. The simulation conditions are similar to those of Figure 5.6a with setting the mobility parameter (M) to $7.20 \times 10^{-11} \text{ m}^3/\text{kg}$ ². As the value of the Cn number becomes higher, the critical Re number of toluene shifts to a higher value as well. Based on the linear regression line derived from the critical Re number and the Cn number in Figure 5.7, the critical Re number of toluene increases linearly with respect to the Cn number, *i.e.*, $Re_{critical} \propto Cn$. Such results agree with the findings in Section 3.3.3 that the slug length (feature of the flow to monitor) is linearly proportional to the Cn number.

²With this value when $Cn = 0.06$, the simulation results agree with the experimental results, which will be further introduced in Figure 5.8

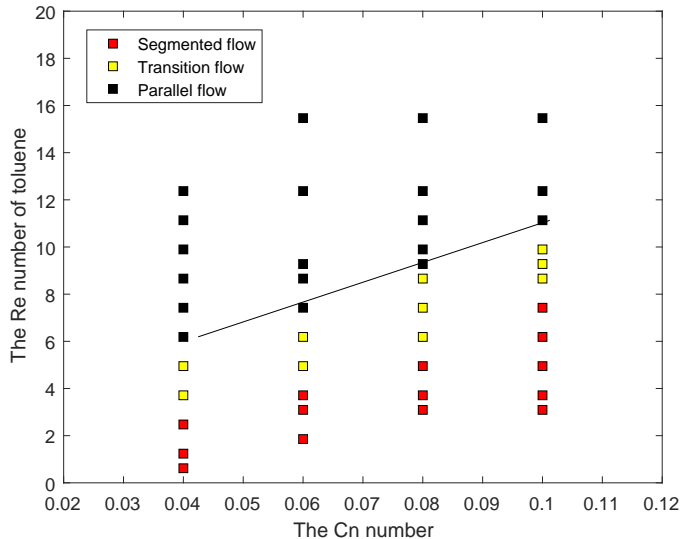


Figure 5.7: The flow pattern map as a function of the Cn number and the Re number of toluene. The linear regression line is derived from the critical Re number and the Cn number. The R^2 of the linear regression line is 0.9917. The red, yellow and black colors denote segmented flow, transition flow and parallel flow, respectively.

Focusing on the research question of this section: to obtain the same simulation result, by keeping $CnPe^{-1}$ constant is still valid in modelling the occurrence of parallel flow in the microfluidic channel? Combining the results in Figure 5.6 and 5.7, clearly the scaling law does not hold anymore. In Chapter 3, it explains that the calculated interfacial tension is linearly proportional to both the capillary width (ϵ) and the mobility parameter (M). Thus, to obtain the same slug length, when the capillary width (ϵ) is varied, the mobility parameter (M) need to be changed by following $CnPe^{-1} = \text{constant}$. In modelling parallel flow in this study, the calculated interfacial tension is still proportional to the Cn number since the critical Re number increases linearly as the Cn number (see Figure 5.7). However, the critical Re number of toluene approximately linearly scales to the common logarithm (logarithm with base 10) of the mobility parameter (M) in Figure 5.6c. Such results indicate the scaling law has changed, even for the same system. The reason behind that could be the Ca number has been changed. *Khatavkar et al.* have investigated the relationship between the capillary width (ϵ) and the mobility parameter (M) by studying the mixing of two immiscible fluids in a lid-driven cavity flow [33]. They have found that the scaling law varies as the Ca number changes. In the dry slug flow studied in Chapter 3, interfacial tension plays an important role (the Ca number around 1×10^{-4}). However, for simulating parallel flow, the interfacial tension is relatively less important and viscous forces take over the flow (which will be discussed in Section 5.3.2 and 5.3.3). Thus, the conclusion here is the scaling law found by dry slug flow does not work in modelling multiphase flow.

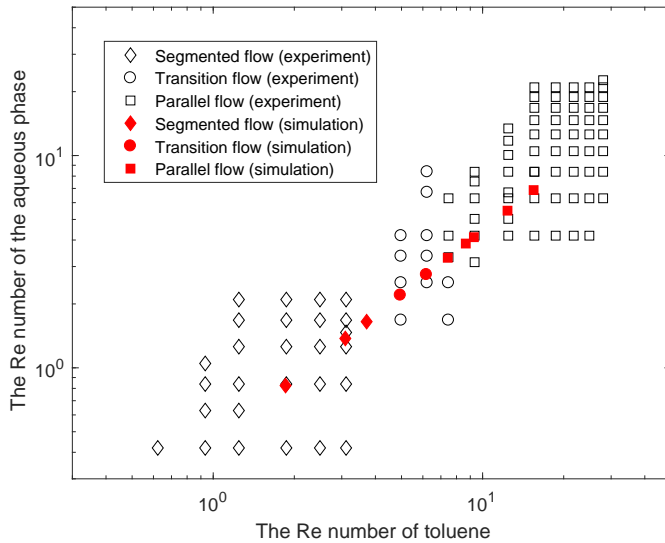


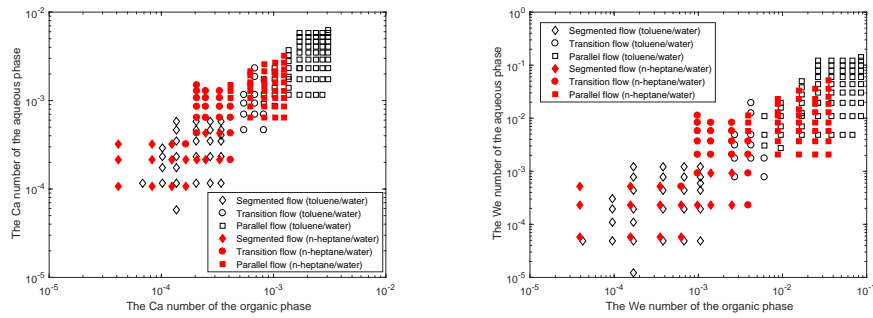
Figure 5.8: Comparison of the experimental results with the simulation results. The flow pattern map is plotted based on the Re number of the toluene/water system. The mobility parameter (M) is set to $7.20 \times 10^{-11} \text{ m}^3/\text{s}/\text{kg}$ while the Cn number of the simulation is 0.06. The diamonds, circles and squares denote segmented flow, transition flow and parallel flow, respectively. The black symbols indicate the experimental results while the red symbols indicate the simulation results.

Based on the simulation results of Figure 5.6, increasing the values of the mobility parameter (M) and the capillary width (c) leads to an increasing critical Re number of the system. To utilize the Phase Field method as a predictive tool to model the multiphase flow pattern inside the microfluidic channel, it is necessary to find if there is a specific combination of these two numerical parameters, with which the flow pattern in the simulations agrees with that in the experiments. For this purpose, in the simulations, the Cn number is kept as 0.06, to ensure the calculation is affordable. The mobility parameter (M) has been varied from $1 \times 10^{-11} \text{ m}^3/\text{s}/\text{kg}$ to $1 \times 10^{-9} \text{ m}^3/\text{s}/\text{kg}$. The volumetric flow rate ratio (Φ_{aq}/Φ_{org}) of the aqueous phase to toluene is kept at 0.66, which is calculated based on Equation 5.1. In Figure 5.8, the experimental results of the toluene/water system serving as the benchmark are directly extracted from Figure 5.5. Among all the tested mobility parameters, it is found that when the mobility parameter (M) is set to $7.20 \times 10^{-11} \text{ m}^3/\text{s}/\text{kg}$, the simulation results fit the experimental results best. Therefore, to highlight the comparison between the simulation results and the experimental results, only the simulation results when the mobility parameter (M) is set to $7.20 \times 10^{-11} \text{ m}^3/\text{s}/\text{kg}$ are plotted in Figure 5.8. Thus, $M = 7.20 \times 10^{-11} \text{ m}^3/\text{s}/\text{kg}$ is set as the specific mobility parameter for the toluene/water system when the Cn number is 0.06, which will be further used in the following study in this chapter.

5.3.2. FLOW PATTERN VERSUS THE CA NUMBER

Concerning predicting flow patterns with dimensional analysis, as has been mentioned in Section 5.1, there are no universally applicable criteria on the flow patterns in microfluidic channels. According to Section 2.1.3, the interfacial tension between the two phases tries to bend the interface, forming segmented flow in microfluidics. On the other hand, based on the experimental results in Figure 5.5, the parallel flow pattern occurs at high volumetric flow rates. Regarding the dimensionless number, the Ca number scales the relative importance of the viscous forces to the interfacial tension while the We number scales the relative importance of the inertia forces to the interfacial tension. Both of them have been proposed to predict flow patterns [6] [10] [11]. This section focuses on if the flow patterns can be predicted with the Ca number while Section 5.3.3 investigates the effect of the We number.

5



(a) The flow pattern map is plotted based on the Ca number of the two phases.

(b) The flow pattern map is plotted based on the We number of the two phases.

Figure 5.9: Flow pattern maps of the toluene/water system and n-heptane/water system in the IMT double Y-shaped microfluidic chip. The diamonds, circles and squares denote the segmented flow, the transition flow and the parallel flow pattern, respectively. The black symbols denote the toluene/water system while the red symbols denote n-heptane/water system.

Experiments concerning the flow patterns were conducted in the IMT double Y-shaped microfluidic chip with the toluene/water system and the n-heptane/water system, respectively. For both systems, the volumetric flow rates of both phases were varied and three flow patterns appeared, namely the segmented flow pattern, the parallel flow pattern and the transition flow pattern. This section mainly focuses on the conditions when the parallel flow pattern appears, under which the parallel microfluidic solvent extraction can be applied. The experimental results are plotted in Figure 5.9. Specifically, in Figure 5.9a, the flow pattern map is plotted based on the Ca number of the two phases while the flow pattern map based on the We number of the two phases is plotted in Figure 5.9b. The dimensionless number of each phase is calculated based on the average velocity of the fluid at the inlet of the microfluidic channel. In Figure 5.9a, for

both the toluene/water system and the n-heptane/water system, the parallel flow pattern is maintained when the Ca number of both phases is larger than approximately 1×10^{-3} . Concerning the We number, the We number needs to be larger than approximately 5×10^{-3} for both phases to sustain the parallel flow pattern. However, increasing the volumetric flow rate of the fluid results in increasing the values of both the Ca number and the We number. Therefore, based on the results in Figure 5.9, no solid conclusion can be drawn yet which dimensionless number determines the flow patterns in the studied microfluidic channel. This issue will be further discussed with help of the Phase Field method, where the Ca number and the We number can be changed independently by varying the dynamic viscosity or the density of the fluids.

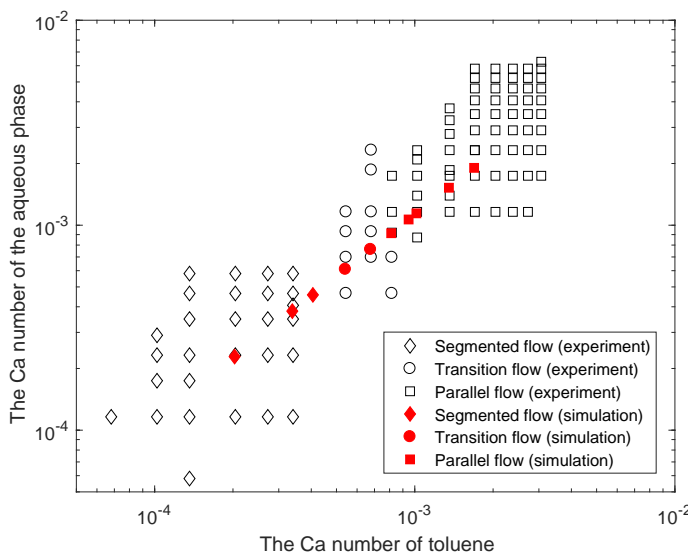


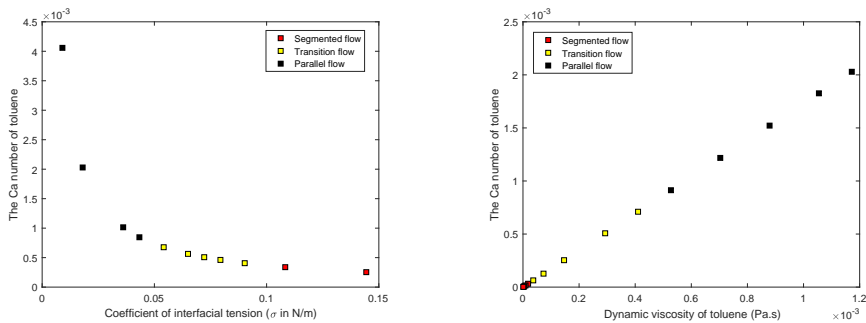
Figure 5.10: Comparison of the experimental results with the simulation results. The flow pattern map is plotted based on the Ca number of the toluene/water system. The mobility parameter (M) is set to $7.20 \times 10^{-11} \text{ m}^3\text{s/kg}$ while the Cn number of the simulation is 0.06. The diamonds, circles and squares denote segmented flow, transition flow and parallel flow, respectively. The black symbols indicate the experimental results while the red symbols indicate the simulation results.

To numerically study the dominating forces in the flow patterns with the Phase Field method, the results in Figure 5.10 are demonstrated with the Ca number of the fluids, which is varied by changing the volumetric flow rates. The shapes of the symbols are used to distinguish different flow patterns and the colors of the symbols are used to denote the experimental results and simulation results. The mobility parameter (M) is set to $7.20 \times 10^{-11} \text{ m}^3\text{s/kg}$ while the Cn number is set to 0.06, as determined in Figure 5.8. The volumetric flow rate ratio (Φ_{aq}/Φ_{org}) of the aqueous phase to toluene is kept at 0.66, which is calculated based on Equation 5.1. As can be found in Figure 5.10, in the simulations, the segmented flow pattern occurs when the Ca number of toluene is smaller

than 4.06×10^{-4} and the parallel flow pattern appears when the Ca number of toluene is larger than 8.12×10^{-4} . In between, the transition flow pattern is found.

To further study if the Ca number can predict flow patterns in the microfluidic channel under investigation, Figure 5.11 demonstrates a set of numerical tests of the influence of the Ca number on the flow pattern. In the simulations, the Cn number is set to 0.06 while the mobility parameter (M) is set to $7.20 \times 10^{-11} \text{ m}^3\text{s/kg}$, which has been proven to agree with the experimental results in Figure 5.10. The volumetric flow rate of toluene had a fixed value of $15.0 \mu\text{L}/\text{min}$ while the volumetric flow rate of the aqueous phase had a fixed value of $9.9 \mu\text{L}/\text{min}$. The corresponding Ca number of toluene and the aqueous phase in the experiments are 1.01×10^{-3} and 1.14×10^{-3} , respectively. Under such circumstances, the parallel flow pattern is obtained in the experiments.

In Figure 5.11a, the Ca number of toluene is varied by changing the coefficient of interfacial tension (σ). The value of the coefficient of interfacial tension (σ) is plotted on the horizontal axis while the corresponding Ca number is plotted on the vertical axis. As the Ca number is increased, the flow pattern changes from segmented flow to transition flow and lastly to parallel flow, the tendency of which agrees with the experimental results in Figure 5.9a. Specifically, in the simulations, when the Ca number of toluene is larger than 8.45×10^{-4} , the flow pattern belongs to the parallel flow pattern.



(a) The Ca number of toluene is varied by changing the coefficient of interfacial tension (σ).

(b) The Ca number of toluene is varied by changing the dynamic viscosity.

Figure 5.11: Study the influence of the Ca number of toluene on the flow patterns. The red, yellow and black colors denote segmented flow, transition flow and parallel flow, respectively.

Besides, in Figure 5.11b, the Ca number of toluene is varied by changing the dynamic viscosity (μ) while the dynamic viscosity ratio (μ_{aq}/μ_{org}) of the two phases is always kept constant. Therefore, the ratio of the Ca number of toluene to the Ca number of water is also kept constant. The value of the dynamic viscosity of toluene is plotted on the horizontal axis while the corresponding Ca number of toluene is plotted on the vertical axis. It can be found that the critical Ca number of toluene for the parallel pattern

in the simulations due to the change of dynamic viscosity is 9.13×10^{-4} , which is comparable with that of changing the coefficient of interfacial tension ($Ca = 8.45 \times 10^{-4}$) in Figure 5.11a. Considering the simulation results in Figure 5.10, when varying the volumetric flow rates, the parallel flow pattern is found when the Ca number of toluene is larger than 8.12×10^{-4} . In addition, since the volumetric flow rate ratio of the aqueous phase to toluene (Φ_{aq}/Φ_{org}) follows Equation 5.1, it can be calculated that the critical Ca number of the aqueous phase is 9.14×10^{-4} . Therefore, combining the experimental results with the simulation results, it can be concluded that the parallel flow pattern can be maintained when the Ca number of both phases is larger than 1×10^{-3} , regarding the fact that it is equivalent to varying the coefficient of interfacial tension (σ) or the dynamic viscosity (μ) when Equation 5.1 is fulfilled.

5.3.3. FLOW PATTERN VERSUS THE WE NUMBER

This section discusses the influence of the We number on the flow patterns with the Phase Field method. For this purpose, in the simulations, the Cn number is set to 0.06 while the mobility parameter (M) is set to $7.20 \times 10^{-11} \text{ m}^3/\text{s/kg}$, which are the same as those in Section 5.3.2. Figure 5.12 shows the We number of both phases in the toluene/water system, where the We number is varied by changing the volumetric flow rates. The volumetric flow rate ratio of the aqueous phase to toluene (Φ_{aq}/Φ_{org}) is always kept as 0.66, which is calculated based on Equation 5.1. Focusing on the experimental results in Figure 5.12, which are extracted from Figure 5.10, the critical We number (the first time the parallel flow pattern is shown) of toluene is around 5×10^{-3} . The numerically found critical We number in Figure 5.12 is 6.02×10^{-3} , which is comparable with that of the experimental results. However, in Figure 5.12, when the We number of toluene is varied by changing the volumetric flow rate, the Ca number of toluene is also changed accordingly. To focus on the influence of the We number on the flow patterns, in the following simulations, the density of the fluids will be changed. In this way, the We number is varied due to the change of density while the Ca number, which is not a function of the density, can be kept constant. As a result, the influence of the We number can be independently studied.

To study the influence of the We number on the flow patterns, in the simulations, the volumetric flow rate of toluene is set to $5.0 \mu\text{L}/\text{min}$, $8.0 \mu\text{L}/\text{min}$, $15.0 \mu\text{L}/\text{min}$ and $30.0 \mu\text{L}/\text{min}$, respectively. The volumetric flow rate ratio of the aqueous phase to toluene (Φ_{aq}/Φ_{org}) is always kept as 0.66. The simulation results are plotted in Figure 5.13 where the We number of toluene is plotted on the horizontal axis while the corresponding Ca number of toluene is plotted on the vertical axis.

When the volumetric flow rate of toluene is set to $5.0 \mu\text{L}/\text{min}$, in the experiments, the corresponding Ca number of toluene is 3.38×10^{-4} while the corresponding We number is 1.05×10^{-3} . According to Figure 5.9, under such circumstances, the segmented flow pattern occurs. In the simulation results in Figure 5.13, keeping the Ca number of toluene at 3.38×10^{-4} and increasing the We number by changing the density of these two fluids, the parallel flow pattern appears. In this process, the density ratio (ρ_{aq}/ρ_{org})

of the two phases is always kept constant. The critical We number in the simulations is 2.09×10^{-1} . A similar effect is found in the case when the volumetric flow rate of toluene is $8.0 \mu\text{L}/\text{min}$. In this case, in the experiments, the corresponding Ca number of toluene is 5.41×10^{-4} while the corresponding We number is 2.68×10^{-3} . In this test, increasing the We number can change the transition flow pattern to the parallel flow pattern with a critical We number of 1.34×10^{-1} .

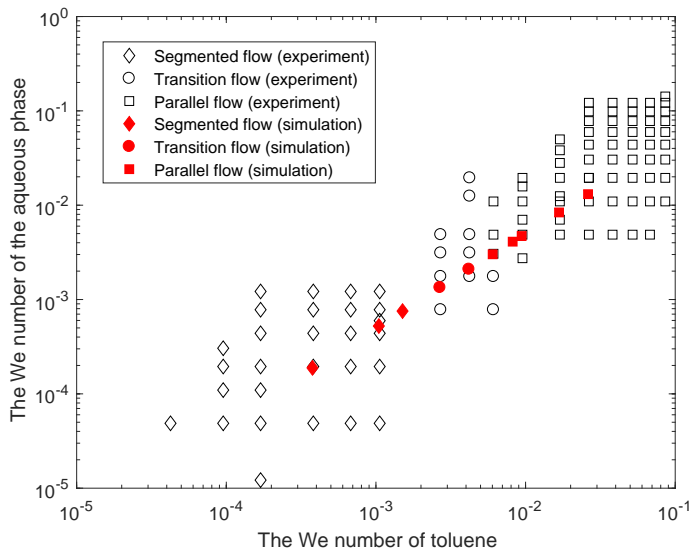


Figure 5.12: Comparison of the experimental results with the simulation results. The flow pattern map is plotted based on the We number of the toluene/water system. The diamonds, circles and squares denote segmented flow, transition flow and parallel flow, respectively. The black symbols indicate the experimental results while the red symbols indicate the simulation results.

With the volumetric flow rate of toluene setting to $15.0 \mu\text{L}/\text{min}$ and $30.0 \mu\text{L}/\text{min}$, the corresponding Ca number of toluene in the experiments is 1.01×10^{-3} and 2.03×10^{-3} . Under such situations, in Figure 5.13, the flow pattern always belongs to the parallel flow, even though the We number of toluene is decreased to 7.53×10^{-5} by changing the density. In other words, when the Ca number of toluene is larger than 1×10^{-3} , the flow pattern is always parallel, showing no dependency on the We number. Such results also confirms the conclusion in Section 5.3.2 that the parallel flow pattern is maintained when the Ca number is larger than 1×10^{-3} .

In summary, combining the results in Section 5.3.2 and this section, it can be concluded that for the studied microfluidic channel, the parallel flow pattern can be obtained when the Ca number of both phases are larger than 1×10^{-3} when Equation 5.1 is fulfilled. Besides, regarding the We number, the parallel flow pattern occurs by increasing the

density of the fluids when the We number of toluene is larger than 1×10^{-1} .

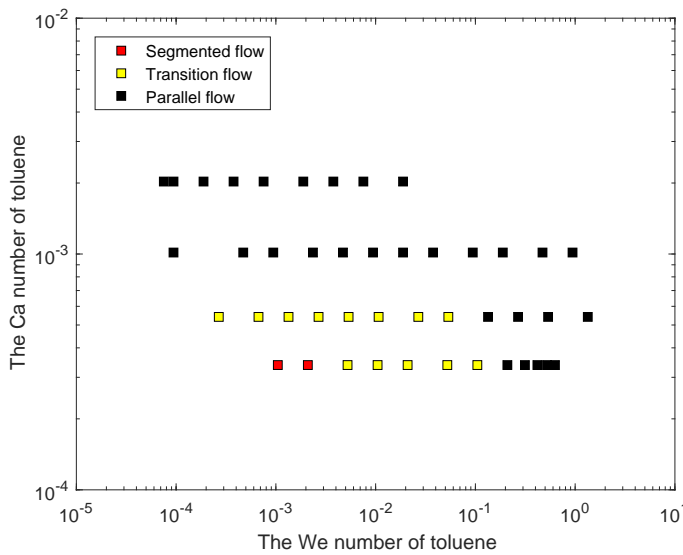


Figure 5.13: The influence of the We number of toluene on the flow patterns. The red, yellow and black colors denote the segmented flow, the transition flow and the parallel flow pattern, respectively. The Ca number is 0.06 and the mobility parameter (M) is set as $7.20 \times 10^{-11} \text{ m}^3\text{s/kg}$.

5.3.4. EQUILIBRIUM CONTACT ANGLE VERSUS FLOW PATTERNS

Based on the study of the toluene/water system, Section 5.3.2 and Section 5.3.3 have shown that the flow patterns within the microfluidic channel are determined by the Ca number when Equation 5.1 is fulfilled and the We number is less than 1×10^{-1} . For the tol+Aliquat/water system, however, the parallel flow pattern occurs at a lower value of the Ca number (*i.e.*, the critical Ca number of tol+Aliquat is 1×10^{-4} in Figure 5.14). One noticeable difference between the tol+Aliquat/water system and the toluene/water system is the equilibrium contact angle (θ_e). It is therefore important to investigate the influence of the equilibrium contact angle (θ_e) on the flow patterns as well.

Figure 5.14 demonstrates the flow pattern map of the tol+Aliquat/water system and the toluene/water system. The flow pattern map is plotted based on the Ca number of each system. For the tol+Aliquat/water system, the parallel flow already occurs when the Ca number is larger than approximately 1×10^{-4} . This result is different from the toluene/water system and n-heptane/water system where the critical Ca number is 1×10^{-3} . The reason for the different critical Ca number can be attributed to the difference in the equilibrium contact angle (θ_e). As shown in Table 5.1, the equilibrium contact angle (θ_e) between toluene/water/glass is 49° , which is comparable with that of n-

heptane/water/glass ($\theta_e = 47^\circ$). However, for the tol+Aliquat/water system, the equilibrium contact angle (θ_e) is 156° . To further investigate the influence of the equilibrium contact angle (θ_e) on the flow patterns, the equilibrium contact angle (θ_e) is therefore varied in the simulations.

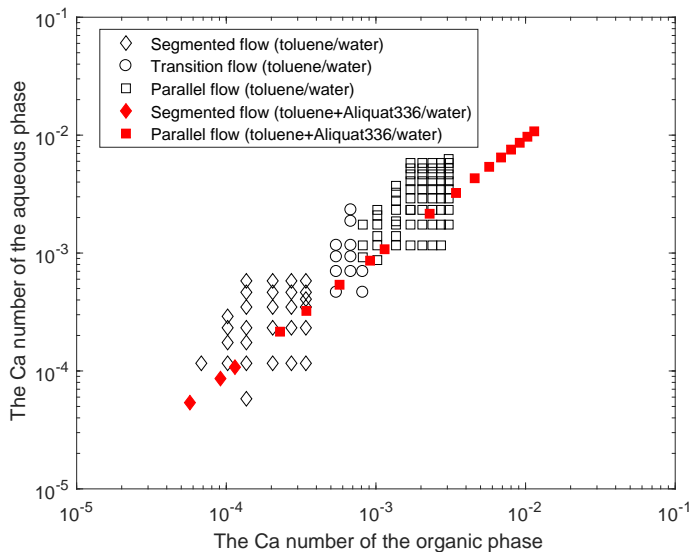


Figure 5.14: Experiment results of the flow patterns of the toluene/water system and the tol+Aliquat/water system in the IMT double Y-shaped microfluidic chip. The diamonds, circles and squares denote segmented flow, transition flow and parallel flow, respectively. The black symbols denote the toluene/water system while the red symbols denote tol+Aliquat/water system.

In the simulations, the working fluids are toluene and water. The C_n number is set to 0.06 while the mobility parameter (M) is set to $7.20 \times 10^{-11} \text{ m}^3\text{s/kg}$, which is the same as those in Section 5.3.2 and Section 5.3.3. The volumetric flow rates are varied in the simulations and the volumetric flow rate ratio of water to toluene is kept at 0.66, according to Equation 5.1. The corresponding Ca number of toluene is plotted on the horizontal axis in Figure 5.15 and the values of the equilibrium contact angle (θ_e) are plotted on the vertical axis of Figure 5.15. The equilibrium contact angle (θ_e) of 10° , 49° , 90° and 156° are investigated in the simulations, among which θ_e of 49° is the measured equilibrium contact angle (θ_e) between toluene and water in Table 5.1 and θ_e of 156° is the measured equilibrium contact angle (θ_e) between tol+Aliquat and water.

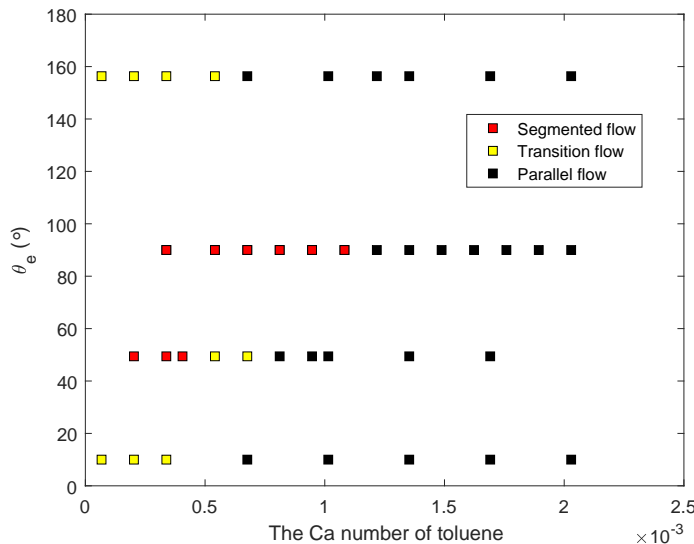


Figure 5.15: Simulation results of the influence of the equilibrium contact angle (θ_e) on the flow patterns. The Cn number is 0.06 and the mobility parameter (M) is set as $7.20 \times 10^{-11} \text{ m}^3/\text{s}/\text{kg}$. The red, yellow and black colors denote segmented flow, transition flow and parallel flow, respectively.

In Figure 5.15, when the equilibrium contact angle (θ_e) is set to 90° , the critical Ca number for the parallel flow pattern is 1.22×10^{-3} , which is larger than the critical Ca number ($Ca=8.12 \times 10^{-4}$) when the equilibrium contact angle (θ_e) is 49° . Moreover, when the equilibrium contact angle (θ_e) is set to 10° , the critical Ca number becomes even smaller, which is 5.41×10^{-4} . Obviously, these results indicate that the equilibrium contact angle (θ_e) influences the occurrence of the parallel flow pattern. When the equilibrium contact angle (θ_e) is set to 90° , it means that the two phases wet the solid surface equally. In this case, according to the simulation results of Figure 5.15, the parallel flow pattern is less likely to occur. In addition, it is also found that the transition flow is not shown. Such result indicates that with $\theta_e = 90^\circ$, as the interface reaches the outlet, it is more likely to pin at the Y-shaped joint part of the microfluidic channel. This simulation result needs further validation by experiments. On the other hand, with the equilibrium contact angle (θ_e) is set to 10° or 156° , one phase dominantly wets the solid surface. Under such a situation, the parallel flow pattern is more likely to occur, resulting in a smaller critical Ca number. Such results are confirmed by the experiments in Figure 5.14 that the critical Ca number in the tol+Aliquat/water system ($\theta_e = 156^\circ$) is lower than the one in the toluene/water system ($\theta_e = 49^\circ$). Additionally, based on the experiments of a kerosene/water two-phase flow system inside a T-shaped PMMA material microfluidic channel, Zhao *et al.* have found similar results that the parallel flow can be formed easily when the equilibrium contact angle (θ_e) close to 0° . Thus, combining the simulation results in this work, it can be concluded that as long as one phase dominantly wet the solid

surface (*i.e.* the equilibrium contact angle (θ_e) is closer to either 0° or 180°), the parallel flow can occur at a low value of the Ca number.

5.4. CONCLUSIONS

To utilize parallel flow microfluidic liquid-liquid solvent extraction to obtain a high-level purity of ^{99}Mo , it is important to keep the interface stable and parallel to the main channel of the microfluidic chip. Until now, there were no clear criteria available for accurately predicting flow patterns in microfluidic channels. This chapter, where experiments are combined with the Phase Field method, aims to provide such criteria for maintaining the parallel flow pattern.

5

This chapter starts with investigating the influence of the mobility parameter (M) and capillary width (ϵ) of the Phase Field method on modelling the parallel flow pattern. In modelling the occurrence of the parallel flow, it finds that increasing the value of the mobility parameter (M) and the capillary width (ϵ) shift the critical Re number (the first time that the parallel flow occurs) to a higher value. However, the criterion ($CnPe^{-1} = \text{constant}$) found based on dry slug flow in Chapter 3 is not valid in modelling parallel flow. The Phase Field method can be utilized in this chapter for predicting flow patterns by finding the specific combination of the mobility parameter (M) and the Cn number, under which condition the simulation results agree with the experimental results.

Based on the experiments, when the interface is located in the centre of the microfluidic channel, the parallel flow pattern can be maintained when the Ca number of both phases is larger than 1×10^{-3} . By studying all the three variables in the Ca number, the Phase Field simulation further confirms that it is the Ca number that determines the flow patterns in the studied microfluidic channel. Further research also shows that the We number plays a minor role in determining the occurrence of the parallel flow pattern in the studied microfluidic system. In other words, the competition between the viscous forces and the interfacial tension determines the occurrence of the parallel flow pattern in the studied microfluidic channel.

Besides the competition between the forces, the interaction between the fluids and the microfluidic channel wall influences the occurrence of parallel flow. Based on the experimental results and the Phase Field simulation of the toluene/water system and the tol+Aliquat/water system, when one of the phases dominantly wets the wall surface (*i.e.*, θ_e is close to 0° or 180°), the parallel flow pattern can occur at lower volumetric flow rates.

REFERENCES

- [1] Davide Ciceri, Jilska M. Perera, and Geoffrey W. Stevens. The use of microfluidic devices in solvent extraction. *Journal of Chemical Technology & Biotechnology*, 89(6):771–786, 2014.
- [2] Clarisse Mariet, Axel Vansteene, Marion Losno, Julien Pellé, Jean-Philippe Jasmin, Anthony Bruchet, and Gwendolyne Hellé. Microfluidics devices applied to radionuclides separation in acidic media for the nuclear fuel cycle. *Micro and Nano Engineering*, 3:7 – 14, 2019.
- [3] Jinyuan Qian, Xiaojuan Li, Zan Wu, Zhijiang Jin, and Bengt Sundén. A comprehensive review on liquid–liquid two-phase flow in microchannel: flow pattern and mass transfer. *Microfluidics and Nanofluidics*, 23:116, 2019.
- [4] Madhvanand N. Kashid and David W. Agar. Hydrodynamics of liquid–liquid slug flow capillary microreactor: Flow regimes, slug size and pressure drop. *Chemical Engineering Journal*, 131(1):1 – 13, 2007.
- [5] Jovan Jovanović, Evgeny V. Rebrov, T. A. (Xander) Nijhuis, M. T. Kreutzer, Volker Hessel, and Jaap C. Schouten. Liquid–liquid flow in a capillary microreactor: Hydrodynamic flow patterns and extraction performance. *Industrial & Engineering Chemistry Research*, 51(2):1015–1026, 2012.
- [6] Anne-Laure Dessimoz, Laurent Cavin, Albert Renken, and Lioubov Kiwi-Minsker. Liquid–liquid two-phase flow patterns and mass transfer characteristics in rectangular glass microreactors. *Chemical Engineering Science*, 63(16):4035 – 4044, 2008.
- [7] P.S. Sarkar, K. K. Singh, K. T. Shenoy, A. Sinha, H. Rao, and S. K. Ghosh. Liquid–liquid two-phase flow patterns in a serpentine microchannel. *Industrial & Engineering Chemistry Research*, 51(13):5056–5066, 2012.
- [8] Hooman Foroughi and Masahiro Kawaji. Viscous oil–water flows in a microchannel initially saturated with oil: Flow patterns and pressure drop characteristics. *International Journal of Multiphase Flow*, 37(9):1147 – 1155, 2011.
- [9] Abdelkader Salim, Mostafa Fourar, Jacques Pironon, and Judith Sausse. Oil–water two-phase flow in microchannels: Flow patterns and pressure drop measurements. *The Canadian Journal of Chemical Engineering*, 86(6):978–988, 2008.
- [10] Yuchao Zhao, Guangwen Chen, and Quan Yuan. Liquid–liquid two-phase flow patterns in a rectangular microchannel. *AICHE Journal*, 52(12):4052–4060, 2006.
- [11] Joshua D. Tice, Adam D. Lyon, and Rustem F. Ismagilov. Effects of viscosity on droplet formation and mixing in microfluidic channels. *Analytica Chimica Acta*, 507(1):73 – 77, 2004.
- [12] Pierre Guillot and Annie Colin. Stability of parallel flows in a microchannel after a T-junction. *Phys. Rev. E*, 72:066301, Dec 2005.

- 5
- [13] Madhvanand Kashid and Lioubov Kiwi-Minsker. Quantitative prediction of flow patterns in liquid–liquid flow in micro-capillaries. *Chemical Engineering and Processing: Process Intensification*, 50(10):972 – 978, 2011. Festschrift Renken.
 - [14] Jonathan D. Wehking, Michael Gabany, Larry Chew, and Ranganathan Kumar. Effects of viscosity, interfacial tension, and flow geometry on droplet formation in a microfluidic T-junction. *Microfluidics and Nanofluidics*, 16:441–453, 2014.
 - [15] Anna A. Yagodnitsyna, Alexander V. Kovalev, and Artur V. Bilsky. Flow patterns of immiscible liquid–liquid flow in a rectangular microchannel with t-junction. *Chemical Engineering Journal*, 303:547 – 554, 2016.
 - [16] Mayur Darekar, Krishna Kumar Singh, Sulekha Mukhopadhyay, and Kalsanka Trivikram Shenoy. Liquid–liquid two-phase flow patterns in Y-junction microchannels. *Industrial & Engineering Chemistry Research*, 56(42):12215–12226, 2017.
 - [17] Zan Wu, Zhen Cao, and Bengt Sunden. Flow patterns and slug scaling of liquid liquid flow in square microchannels. *International Journal of Multiphase Flow*, 112:27 – 39, 2019.
 - [18] Qi Zhang, Hongchen Liu, Shuainan Zhao, Chaoqun Yao, and Guangwen Chen. Hydrodynamics and mass transfer characteristics of liquid–liquid slug flow in microchannels: The effects of temperature, fluid properties and channel size. *Chemical Engineering Journal*, 358:794 – 805, 2019.
 - [19] Chi Young Lee and Sang Yong Lee. Influence of surface wettability on transition of two-phase flow pattern in round mini-channels. *International Journal of Multiphase Flow*, 34(7):706 – 711, 2008.
 - [20] N. Shao, A. Gavrilidis, and P. Angeli. Flow regimes for adiabatic gas–liquid flow in microchannels. *Chemical Engineering Science*, 64(11):2749 – 2761, 2009.
 - [21] Richa Raj, Nikita Mathur, and Vivek V. Buwa. Numerical simulations of liquid liquid flows in microchannels. *Industrial and Engineering Chemistry Research*, 49(21):10606–10614, 2010.
 - [22] Shazia Bashir, Julia M. Rees, and William B. Zimmerman. Simulations of microfluidic droplet formation using the two-phase level set method. *Chemical Engineering Science*, 66(20):4733 – 4741, 2011.
 - [23] Reiyu Chein and S. H. Tsai. Microfluidic flow switching design using volume of fluid model. *Biomedical Microdevices*, 6(1):81–90, Mar 2004.
 - [24] Peter J. Stiles and David F. Fletcher. Hydrodynamic control of the interface between two liquids flowing through a horizontal or vertical microchannel. *Lab Chip*, 4:121–124, 2004.

- [25] Peyman Foroozan Jahromi, Javad Karimi-Sabet, Younes Amini, and Hooman Fadaei. Pressure-driven liquid-liquid separation in Y-shaped microfluidic junctions. *Chemical Engineering Journal*, 328:1075 – 1086, 2017.
- [26] Martin Wörner. Numerical modeling of multiphase flows in microfluidics and micro process engineering: a review of methods and applications. *Microfluidics and Nanofluidics*, 12(6):841–886, May 2012.
- [27] Gwendolyne Hellé, Clarisse Mariet, and Gérard Cote. Liquid–liquid microflow patterns and mass transfer of radionuclides in the systems Eu(III)/HNO₃/DMDBT DMA and U(VI)/HCl/Aliquat® 336. *Microfluidics and Nanofluidics*, 17(6):1113–1128, Dec 2014.
- [28] Gwendolyne Hellé, Sean Roberston, Siméon Cavadias, Clarisse Mariet, and Gérard Cote. Toward numerical prototyping of labs-on-chip: modeling for liquid–liquid microfluidic devices for radionuclide extraction. *Microfluidics and Nanofluidics*, 19(5):1245–1257, Nov 2015.
- [29] Gwendolyne Hellé, Clarisse Mariet, and Gérard Cote. Liquid–liquid extraction of uranium(VI) with Aliquat® 336 from HCl media in microfluidic devices: Combination of micro-unit operations and online ICP-MS determination. *Talanta*, 139:123 – 131, 2015.
- [30] Joseph D. Berry, Michael J. Neeson, Raymond R. Dagastine, Derek Y.C. Chan, and Rico F. Tabor. Measurement of surface and interfacial tension using pendant drop tensiometry. *Journal of Colloid and Interface Science*, 454:226 – 237, 2015.
- [31] Andrej Pohar, Mitja Lakner, and Igor Plazl. Parallel flow of immiscible liquids in a microreactor: modeling and experimental study. *Microfluidics and Nanofluidics*, 12(1):307–316, Jan 2012.
- [32] David Jacqmin. Contact-line dynamics of a diffuse fluid interface. *J. Fluid Mech*, 402:57–88, 2000.
- [33] V.V. Khatavkar, P.D. Anderson, and H.E.H. Meijer. On scaling of diffuse–interface models. *Chemical Engineering Science*, 61(8):2364 – 2378, 2006.
- [34] F. Magaletti, F. Picano, M. Chinappi, L. Marino, and C. M. Casciola. The sharp-interface limit of the Cahn–Hilliard/Navier–Stokes model for binary fluids. *Journal of Fluid Mechanics*, 714:95–126, 2013.
- [35] Pengtao Yue, Chunfeng Zhou, and James J. Feng. Sharp-interface limit of the Cahn–Hilliard model for moving contact lines. *Journal of Fluid Mechanics*, 645:279–294, 2010.

6

LEAKAGE AT THE OUTLET OF THE DOUBLE Y-SHAPED MICROFLUIDIC CHANNEL

6.1. INTRODUCTION

When utilizing the parallel flow microfluidic solvent extraction to purify ^{99}Mo , it is important to maintain a parallel and stable interface [1] [2]. However, when the parallel flow pattern is established, there is leakage from one phase to the other at the outlet of the microfluidic channel, leading to contamination of the extracted ^{99}Mo . In principle, any contamination of the extracted ^{99}Mo is unacceptable because of the strict requirements of the purity of radiopharmaceuticals [3]. Even though the leakage is a common occurrence in parallel microfluidic solvent extraction, there are very few publications focusing on this phenomenon [4][5].

The reason for little attention is paid to the leakage phenomenon can be explained by the fact that, for extracting non-radioactive species, selective surface modification can be used to achieve complete phase separation. As introduced in Section 1.4, the selective surface modification partially changes the wettability of the microfluidic channel by coating the wall surface with a monolayer [6] [7]. For instance, in the case of the glass microfluidic channel in this study, partially coating the surface with a layer of organosilane makes it possible to maintain the aqueous phase in the bare hydrophilic side while keeping the organic phase in the coated hydrophobic side [4] [8] [9] [10]. However, the selective surface modification is not compatible with extracting radioactive nuclides in this research because the monolayer degrades under irradiation environment [11].

6

This thesis focuses on modelling the multiphase flow inside a microfluidic channel with the Phase Field method, aiming to provide guidelines for maintaining the parallel flow pattern and achieving complete phase separation. For this purpose, Chapter 5 dealt with flow patterns in the microfluidic channel by combining experiments with the Phase Field method. In Chapter 5, the leakage phenomenon did not appear probably attributed to the fact that the equilibrium contact angle boundary condition was imposed at the wall of the microfluidic channel, which is not adequate to capture the physics behind the leakage phenomenon.

Leakage involves the *Moving Contact Line*, *i.e.*, the movement of the interface between two immiscible phases on the solid channel wall. As introduced in Section 2.3, due to the movement of the contact line, the apparent contact angle (θ_{app}) deviates from the equilibrium contact angle (θ_e) [12]. Based on the investigation of Chapter 4, with the equilibrium contact angle boundary condition in the simulations, the apparent contact angle (θ_{app}) was always forced to be equal to the equilibrium contact angle (θ_e), which indicated that the physics behind the *Moving Contact Line* was not modelled correctly. With the non-equilibrium contact angle boundary condition, the apparent contact angle (θ_{app}) was allowed to deviate from the prescribed equilibrium contact angle (θ_e) in dry slug flow, which provided more physical simulation results. Thus, it is worthwhile to investigate the behaviour of the non-equilibrium contact angle boundary condition on simulating the leakage in the microfluidic channel.

Concerning the aims of this chapter, the following sections first concentrate on the im-

pact of the value of the prescribed equilibrium contact angle (θ_e) in the Phase Field method on the leakage direction in the studied double Y-shaped microfluidic channel. Secondly, with the equilibrium and non-equilibrium contact angle boundary conditions, this research studies the mechanism behind the occurrence of the leakage phenomenon in the Phase Field method. In addition, simulation results concerning leakage will be validated by experiments.

6.2. MATERIALS AND METHODS

The experiments of investigating the leakage phenomenon were conducted in the IMT ICC-DY05 double Y-shaped microfluidic chip, the geometry and material of which can be found in Section 3.2.1. In the experiments, Milli-Q water served as the aqueous phase. Toluene or tol+Aliquat (mixture solution of toluene and Aliquat336 in which the concentration of Aliquat336 is 0.4 mol/L) served as the organic phase. The experimental procedure was the same as those introduced in Section 3.2.1: before the experiments, the microfluidic chip was rinsed with ethanol for around ten minutes to clean. Then, the whole system was flushed with Milli-Q water for around ten minutes. After making sure that there was no gas bubble in the microfluidic system, the organic solution was pumped into the microfluidic channel.

6

In COMSOL, the 2-dimensional model was the same as the one used in Chapter 5. The input parameters of the physical properties of the fluids (density, dynamic viscosity, coefficient of interfacial tension and equilibrium contact angle) related to this research can be found in Table 5.1. The governing equations for the leakage phenomenon in the microfluidic channel are the Cahn-Hilliard equation (Equation 2.23), the continuity equation (Equation 2.2) as well as the Navier-Stokes momentum equations (Equation 2.24) for multiphase flows. These equations have been introduced in detail in Section 2.5.

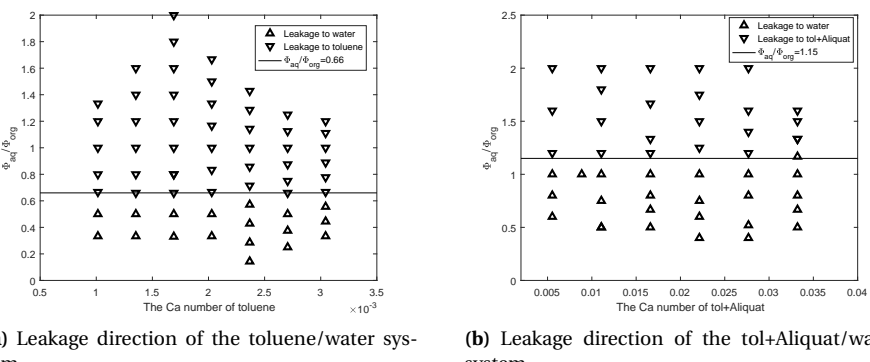
At the two inlets, the average velocity of the fluids was prescribed as boundary conditions. The average velocity was calculated based on the volumetric flow rates of the fluids and the cross-sectional area of the inlet of the microfluidic chip (the geometry of the microfluidic chip is shown in Table 3.1). The velocity profile was assumed to be fully developed since the fluid needed to flow through a capillary tubing (Length: 25 cm) in the experiments. At the two outlets, a reference pressure (Pressure = 0 Pa) was used as the boundary condition. At the solid wall, the no-slip boundary condition was imposed. Equation 2.39 was adopted for the contact angle with $\mu_f = 0 \text{ Pa} \cdot \text{s}$ representing the equilibrium contact angle boundary condition and $\mu_f > 0 \text{ Pa} \cdot \text{s}$ representing the non-equilibrium contact angle boundary condition.

6.3. RESULTS AND DISCUSSION

6.3.1. LEAKAGE DIRECTION AT THE OUTLET OF THE MICROFLUIDIC CHANNEL IN THE EXPERIMENTS

In the experiments, when the parallel flow pattern is obtained, there is always leakage from one phase to the other. The direction of leakage is not fixed and is influenced by operating conditions and fluid properties. This study focuses on the influence of the volumetric flow rate ratio of the aqueous phase to the organic phase (denoted as Φ_{aq}/Φ_{org}) on the leakage direction. The volumetric flow rate ratio (Φ_{aq}/Φ_{org}) is varied in the toluene/water system and the tol+Aliquat/water system. The Ca number of the organic phase, which is calculated using the average velocity of the fluid at the inlet of the microfluidic channel, is plotted on the horizontal axis of Figure 6.1 while the volumetric flow rate ratio (Φ_{aq}/Φ_{org}) is plotted on the vertical axis. The down-pointing triangles indicate that the leakage is from water to the organic phase, since water is always on the upper part of the figure, as illustrated in Figure 6.2. The up-pointing triangles indicate that the leakage is from the organic phase to water.

6



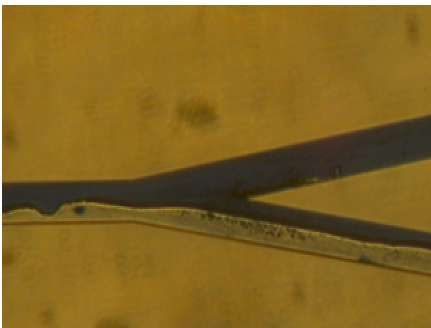
(a) Leakage direction of the toluene/water system.

(b) Leakage direction of the tol+Aliquat/water system.

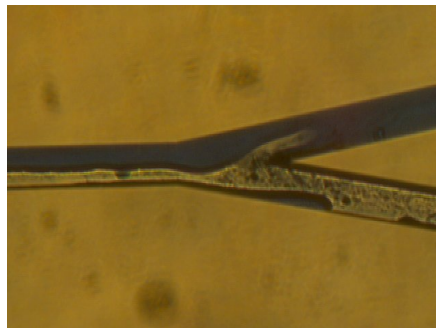
Figure 6.1: Experimental results of the leakage direction of two-phase flows inside the IMT microfluidic channel. The down-pointing triangles indicate that the leakage is from the aqueous phase to the organic phase. The up-pointing triangles indicate that the leakage is from the organic phase to the aqueous phase.

In the experiments, the Ca number of toluene is high enough ($Ca > 1 \times 10^{-3}$ by controlling the volumetric flow rate) to maintain the parallel flow pattern in the microfluidic channel. In Figure 6.1, the volumetric flow rate ratio (Φ_{aq}/Φ_{org}) influences the leakage direction by determining the position of the interface between the two phases in the microfluidic channel. Concerning avoiding the leakage, the first attempt is positioning the interface in the centre of the microfluidic channel. For this purpose, Pohar *et al.* have proposed an empirical correlation between the flow rate ratio (Φ_{aq}/Φ_{org}) and

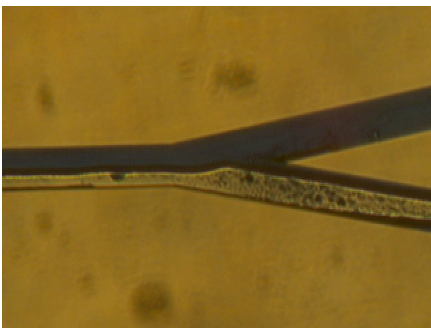
the dynamic viscosity ratio (μ_{aq}/μ_{org}) of the two phases for positioning the interface in the middle of a single Y-shaped microfluidic channel [13], as shown in Equation 5.1. According to Equation 5.1 and the physical properties of the fluids in Table 5.1, the flow rate ratio (Φ_{aq}/Φ_{org}) of the toluene/water system should be 0.66 and the tol+Aliquat/water system should be 1.15. Figure 6.1 shows solid lines to indicate the volumetric flow rate ratio calculated based on Equation 5.1 for the specific combination of fluids, which are parallel to the horizontal axis.



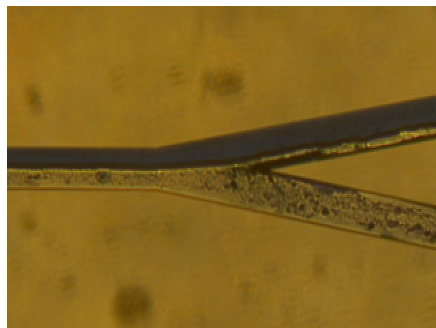
(a) Leakage of water to the toluene outlet. The Ca number of toluene is 2.18×10^{-3} . The volumetric flow rate ratio (Φ_{aq}/Φ_{org}) of these two phases is 0.8.



(b) Leakage of toluene to the water outlet. The Ca number of toluene is 2.18×10^{-3} . The volumetric flow rate ratio (Φ_{aq}/Φ_{org}) of these two phases is 0.3.



(c) Leakage of water to the toluene outlet. The Ca number of toluene is 2.18×10^{-3} . The volumetric flow rate ratio (Φ_{aq}/Φ_{org}) of these two phases is 0.67.



(d) Leakage of tol+Aliquat to the water outlet. The Ca number of tol+Aliquat is 1.14×10^{-3} . The volumetric flow rate ratio (Φ_{aq}/Φ_{org}) of these two phases is 1.

Figure 6.2: Leakage at the outlets of the double Y-shaped IMT microfluidic channel. The aqueous phase is dyed with methylene blue (0.1%, *w/w*).

The experimental results in Figure 6.1 clearly show that Equation 5.1 can be used to predict the leakage direction. When the volumetric flow rate ratio (Φ_{aq}/Φ_{org}) is larger than the one calculated based on Equation 5.1, the interface shifts downwards in the microfluidic channel, resulting in leakage to the organic outlet, vice versa. For example, in Figure 6.2a when $\Phi_{aq}/\Phi_{org} = 0.8 (> 0.66)$, water is leaking to the toluene outlet.

When $\Phi_{aq}/\Phi_{org} = 0.3$ (< 0.66) in Figure 6.2b, there is leakage from toluene to water. Adjusting the volumetric flow rate ratio (Φ_{aq}/Φ_{org}) to keep the interface in the middle of the microfluidic channel (*i.e.*, adjusting Φ_{aq}/Φ_{org} to approach the solid line in Figure 6.1) can help to reduce the amount of leakage, as shown in Figure 6.2c. Despite the fact that the location of the interface is positioned in the centre of the channel; however, leakage always exists and complete phase separation cannot be achieved. Besides, it is found that when the interface is positioned in the centre of the channel, the leakage direction is different in the toluene/water system and in the tol+Aliquat/water system. In the toluene/water system in Figure 6.2c, water tends to leak to the toluene outlet while the tol+Aliquat tends to leak to the water outlet in the tol+Aliquat/water system in Figure 6.2d. This can be explained as, according to Table 5.1, the equilibrium contact angle ($\theta_e = 49^\circ$) of water in bulk toluene solution is less than 90° , which means the glass channel wall is hydrophilic and is preferably wetted by water. In contrast, the equilibrium contact angle ($\theta_e = 156^\circ$) of water in the bulk tol+Aliquat solution on a glass surface is larger than 90° , which means the glass channel wall is preferable to be wetted by tol+Aliquat. The influence of the value of the equilibrium contact angle (θ_e) and the boundary conditions for the contact angle will be further studied in Section 6.3.2 with numerical simulations.

6.3.2. LEAKAGE PHENOMENON BY CHANGING THE EQUILIBRIUM ANGLE

6

This numerical study investigates whether the Phase Field method can simulate the leakage phenomenon occurs in the experiments. As introduced in Section 4.1, the boundary condition for the contact angle plays an important role in simulating the *Moving Contact Line*, which is believed to influence the leakage at the outlet of the microfluidic channel. The research starts with studying the influence of the equilibrium contact angle boundary condition (by setting $\mu_f = 0 \text{ Pa}\cdot\text{s}$ in Equation 2.39) on the leakage phenomenon. The simulation model is the same as the one used to simulate the toluene/water system in the IMT microfluidic chip in Chapter 5. The physical properties of the fluids are adopted from Table 5.1. In the simulations, the Cn number is set to 0.06 while the mobility parameter (M) is set to $7.20 \times 10^{-11} \text{ m}^3/\text{kg}$. The choice of these two parameters was based on Section 5.3.2 where it has been shown that the simulation results of this combination of numerical parameters agreed with the experimental results of predicting the flow patterns in the microfluidic channel. To locate the interface in the centre of the main channel, the volumetric flow rate ratio (Φ_{aq}/Φ_{org}) of water and toluene is kept at 0.66 (Equation 5.1). The Ca number of toluene, which is varied by changing the volumetric flow rate, is plotted on the horizontal axis of Figure 6.3. The red square symbols represent segmented flow or transition flow and the black symbols represent parallel flow. Specifically, the black square symbols indicate that the interface is pinned on the wall of the outlets. The down-pointing triangles indicate that the leakage is from the aqueous phase to the organic phase and the up-pointing triangles indicate that the leakage is from the organic phase to the aqueous phase, which are the same as those of Figure 6.1.

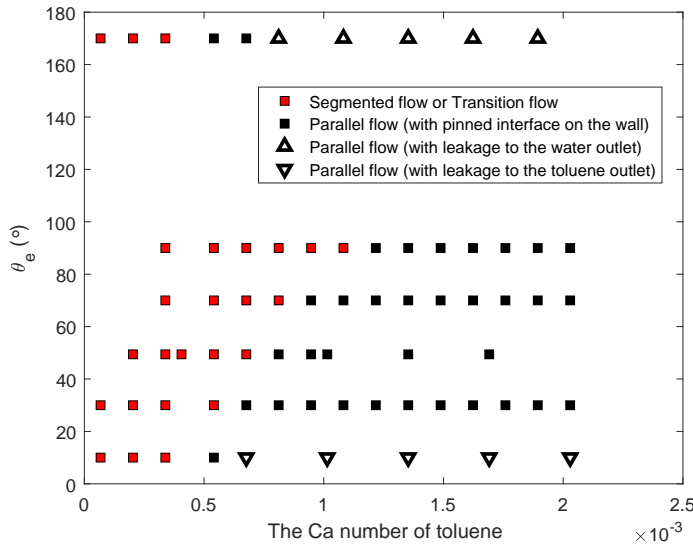
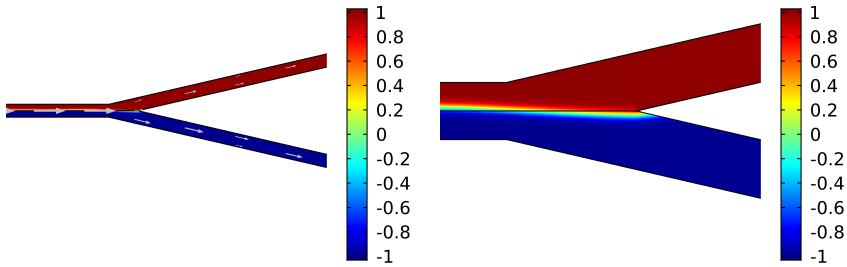
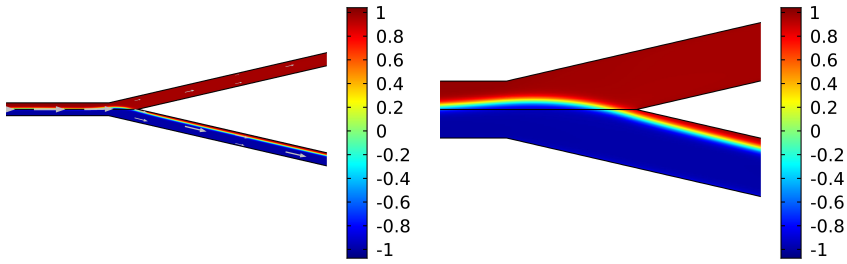


Figure 6.3: Influence of the chosen equilibrium contact angle (θ_e) on the leakage phenomenon in the simulations. $C_n = 0.06$. $M = 7.20 \times 10^{-11} \text{ m}^3/\text{s}/\text{kg}$. $\mu_f = 0 \text{ Pa}\cdot\text{s}$. For the parallel flow, the squares indicate that the interface is pinned on the wall of the microfluidic channel. The down-pointing triangles indicate that the leakage is from the aqueous phase to the organic phase. The up-pointing triangles indicate that the leakage is from the organic phase to the aqueous phase.

In Figure 6.3, in the case of $\theta_e = 49^\circ$ (the measured equilibrium contact angle between water and toluene, as shown in Table 5.1), it can be seen that the flow pattern changes from segmented flow / transition flow to parallel flow when the Ca number of toluene increases. Such results agree with the experimental findings in Chapter 5 that parallel flow is more likely to occur when the value of the Ca number is high. When parallel flow is established, the interface is pinned on the Y-joint part of the microfluidic channel, as demonstrated in Figure 6.4a and Figure 6.4b. Besides, the interface does not change with respect to time at the same simulation conditions. In the simulations, the pinned interface indicates that complete phase separation is achieved. These results, however, do not agree with the experimental results shown in Figure 6.1 where there is always leakage from water to toluene when the interface is located at the centre of the microfluidic channel.



(a) The interface is pinned on the wall of the microfluidic channel. $\theta_e = 49^\circ$
 (b) Zooming in the Y-joint part of the outlet of Figure 6.4a



(c) There is leakage from the aqueous phase to the organic phase. $\theta_e = 10^\circ$
 (d) Zooming in the Y-joint part of the outlet of Figure 6.4c

Figure 6.4: Schematic diagram of pinned interface and leakage at the outlet of the double Y-shaped microfluidic channel. The color legend indicates the value of the order parameter ϕ . $\phi = 1$ indicates the aqueous phase while $\phi = -1$ represents the organic phase and $-1 < \phi < 1$ represents the interface.

With the same simulation conditions, the equilibrium contact angles (θ_e) of 10° , 30° , 70° , 90° and 170° are also investigated and plotted on the vertical axis of Figure 6.3. It is found that the prescribed value of the equilibrium contact angle (θ_e) changes the Ca number where parallel flow starts to occur, as discussed in Section 5.3.4. Based on the results in Figure 6.3, however, the leakage only occurs when the prescribed equilibrium contact angle (θ_e) is set to 10° and 170° . The direction of leakage is correct for 10° and 170° : when the equilibrium contact angle (θ_e) is 10° , the leakage is from the aqueous phase to the organic phase, as illustrated in Figure 6.4c and Figure 6.4d. When the equilibrium contact angle (θ_e) is 170° , the leakage is from the organic phase to the aqueous phase. However, as shown in Figure 6.3 when θ_e is in the range between 30° to 90° , the leakage phenomenon does not occur in the simulations, which is in contrast to the experimental findings.

6.3.3. LEAKAGE PHENOMENA BY USING THE NON-EQUILIBRIUM CONTACT ANGLE BOUNDARY CONDITION

Obviously, with merely using the equilibrium contact angle boundary condition, the leakage in the simulations does not agree with that in the experiments when θ_e is in the range between 30° to 90° . Based on the study of the apparent contact angles (θ_{app}) of the slugs in Chapter 4, applying the non-equilibrium contact angle boundary condition ($\mu_f > 0 \text{ Pa} \cdot \text{s}$ in Equation 2.39) allows the apparent contact angle (θ_{app}) to deviate from the prescribed equilibrium contact angle (θ_e), which provides more physical results regarding the *Moving Contact Line*. Since leakage at the end of the chip is, among other things, determined by the *Moving Contact Line* between both phases, the influence of the non-equilibrium contact angle boundary condition on the leakage needs to be studied.

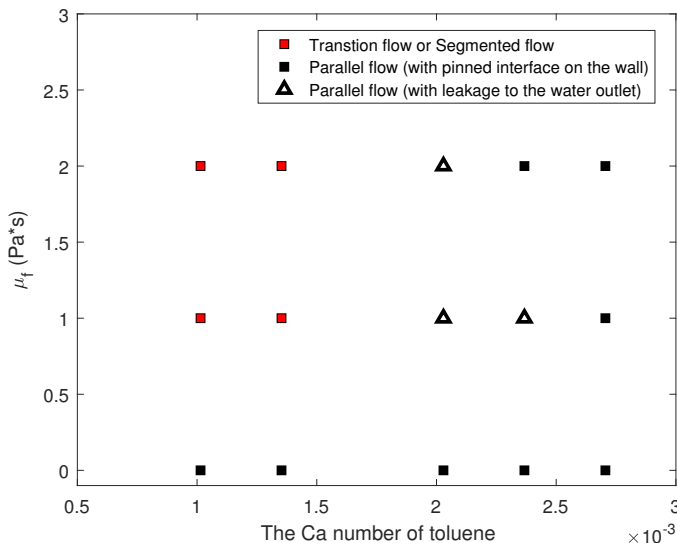


Figure 6.5: Influence of the Ca number and contact line friction parameter (μ_f) on the leakage phenomenon of the toluene/water system. $Cn = 0.06$. $M = 7.20 \times 10^{-11} \text{ m}^3/\text{s}$. $\theta_e = 49^\circ$. The black squares indicate that the interface is pinned on the wall of the microfluidic channel. The up-pointing triangles indicate that the leakage is from the organic phase to the aqueous phase.

In the simulations, the volumetric flow rate ratio of water to toluene (Φ_{aq}/Φ_{org}) is 0.66, which is derived based on Equation 5.1. The Cn number is set to 0.06 and the mobility parameter (M) is set to $7.20 \times 10^{-11} \text{ m}^3/\text{s}$, which are the same as those in Figure 6.3. The prescribed equilibrium contact angle (θ_e) is 49° , the same as the one in the experiments. By studying the apparent contact angles (θ_{app}) of the n-heptane slugs in Section 4.3.5, it has been found that when the contact line friction parameter (μ_f) is set to be between $1.0 \text{ Pa} \cdot \text{s}$ and $2.0 \text{ Pa} \cdot \text{s}$, the advancing contact angle (θ_A) and receding contact angle

(θ_R) in the simulations agrees with the experimental results. Figure 6.5 therefore shows the contact line friction parameter (μ_f) on the vertical axis in the range between 0 and $2.0 \text{ Pa} \cdot \text{s}$. The Ca number of toluene on the horizontal axis is changed by varying the volumetric flow rate.

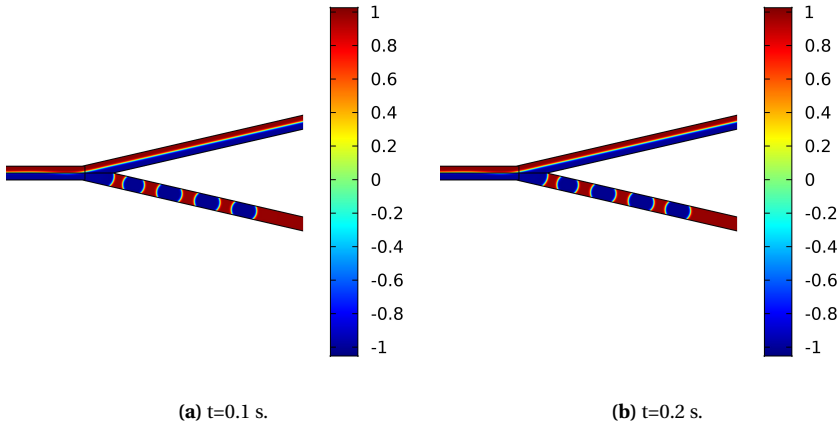
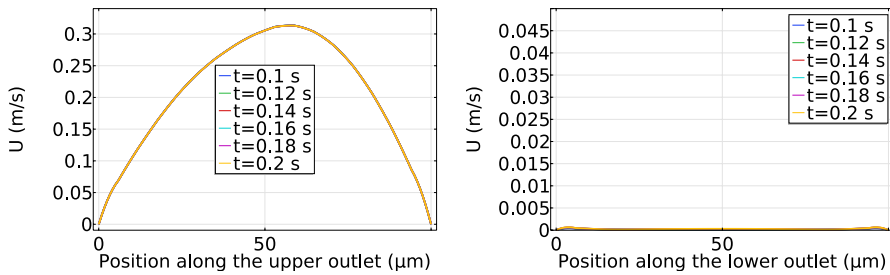


Figure 6.6: Schematic diagram of leakage from toluene to the water outlet. The color legend indicates the value of the order parameter ϕ . $\phi = 1$ indicates water while $\phi = -1$ represents toluene and $-1 < \phi < 1$ represents the interface. $\mu_f = 2.0 \text{ Pa} \cdot \text{s}$. $Ca = 2.03 \times 10^{-3}$. $Cn = 0.06$. $M = 7.20 \times 10^{-11} \text{ m}^3/\text{kg}$. $\theta_e = 49^\circ$.

According to the results in Figure 6.5, sometimes there is leakage from toluene to water, opposite to the expected direction of the leakage. This is caused by imposing the non-equilibrium contact angle boundary condition. Figure 6.6 illustrates the leakage from toluene to water, together with the presence of a few toluene slugs in the lower outlet. The position of the slugs does not change with time, as shown in Figure 6.6a and Figure 6.6b. Such results indicate that the leakage from toluene to water is due to the fact that the lower outlet is clogged by the toluene slugs. To further demonstrate this phenomenon, Figure 6.7a and Figure 6.7b illustrate the velocity magnitude profile along with the upper outlet and lower outlet of Figure 6.6, respectively. In the time interval from 0.1s to 0.2s in the simulations, the velocity magnitude at the lower outlet remains zero, which indicates that the lower outlet is clogged by the toluene slugs. Extending the simulation time to 1s, the result is the same. It has been reported that a microfluidic system can be clogged by gas bubbles or particles [14] [15]. But clogging of the microfluidic channel with organic fluid slugs, however, is not found in the literature or in the experiments in this research. It can therefore be concluded that, the clogging phenomenon is considered as an unphysical simulation result and must be caused by the non-equilibrium contact angle boundary condition.



(a) Velocity magnitude profile (all profiles are overlapped) at the upper outlet when there is leakage from toluene to water. $\mu_f = 2.0 \text{ Pa} \cdot \text{s}$.

(b) Velocity magnitude profile (all profiles are overlapped) at the lower outlet when there is leakage from toluene to water. $\mu_f = 2.0 \text{ Pa} \cdot \text{s}$.

Figure 6.7: Velocity magnitude profile along the outlet of the macrofluidic channel. $Ca = 2.03 \times 10^{-3}$. $Cn = 0.06$. $\theta_e = 49^\circ$.

6.3.4. INFLUENCE OF THE MOBILITY PARAMETER ON THE LEAKAGE

In Section 5.3.1 where the relationship between the mobility parameter (M) and flow patterns were investigated, the leakage phenomenon was sometimes observed when varying the mobility parameter (M). These results indicate that the mobility parameter (M) plays a role in the occurrence of leakage in the simulations. Thus, in this section, the influence of the mobility parameter (M) is investigated.

In the simulations, the Ca number of toluene is set to 1.01×10^{-3} , 1.35×10^{-3} and 2.03×10^{-3} by changing the volumetric flow rates, which is plotted on the vertical axis. To position the interface in the centre of the main channel, the volumetric flow rate ratio (Φ_{aq}/Φ_{org}) of water to toluene is kept at 0.66, which is calculated based on Equation 5.1. According to the experimental results in Figure 6.1, under such conditions, the parallel flow pattern with leakage to the toluene outlet is expected. The Cn number is 0.06, $\mu_f = 0 \text{ Pa} \cdot \text{s}$ and $\theta_e = 49^\circ$, which are the same as those of Section 6.3.2. Figure 6.8 demonstrates the simulation results as a function of the Pe number ($Pe = \frac{2\sqrt{2}ULc}{3M\sigma}$) on the horizontal axis. The Pe number is varied by changing the mobility parameter (M) and the volumetric flow rate. The symbols used to distinguish different flow patterns are the same as those in Figure 6.3. The black square symbols indicate that the interface is pinned on the wall of the microfluidic channel. The down-pointing triangles indicate that the leakage is from the aqueous phase to the organic phase.

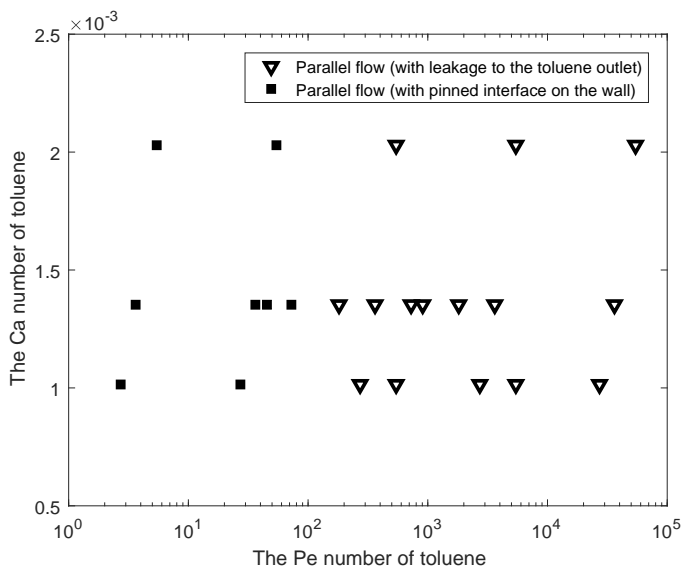


Figure 6.8: Influence of the mobility parameter (M) on the leakage phenomenon of the toluene/water system. $C_n = 0.06$. $\theta_e = 49^\circ$. $\mu_f = 0 \text{ Pa} \cdot \text{s}$. The black squares indicate that the interface is pinned on the wall of the microfluidic channel. The down-pointing triangles indicate that the leakage is from the aqueous phase to the organic phase.

When the Pe number of toluene, being a function of M here, is in the range between 1 to 100, the interface is pinned on the microfluidic channel wall. If we increase the mobility parameter (M), the leakage phenomenon occurs when Pe numbers of toluene is above 100. Figure 6.8 shows that the leakage at the outlet is influenced by the mobility parameter (M). In addition, Figure 6.8 also explains why the leakage phenomenon does not occur in Figure 6.3 in the case of $\theta_e = 49^\circ$. In Figure 6.3, the corresponding Pe number of toluene is in the range between 10.9 and 22.7, which belongs to the range ($1 < Pe < 100$) where the interface pins on the channel wall in Figure 6.8.

The mobility parameter (M) influences the occurrence of leakage because it determines the diffusive transport of the order parameter (ϕ) in the Phase Field method. As explained in Section 3.3.1, the whole system tends to minimize the free energy (E_{free}) by changing the distribution of the order parameter (ϕ). The mobility parameter (M) determines the global diffusive movement of the order parameter (ϕ) [16]. When the value of the mobility parameter (M) is high (low Pe number), the diffusive movement of the order parameter (ϕ) is fast and the system relaxes to the equilibrium state quickly. When the equilibrium state is reached, the leakage phenomenon does not occur. On the other hand, when the value of the mobility parameter (M) is low (high Pe number), the system relaxes slowly to the equilibrium state, leading to the possibility of the occurrence of leakage in the simulations. Thus, to simulate the occurrence of the leakage phenomenon, the value of the mobility parameter (M) needs to be set below a certain

threshold. However, based on Section 5.3.1, the mobility parameter (M) also influences the flow patterns in the microfluidic channel. Decreasing the value of M will therefore change the critical Ca number (*i.e.* the first time that the parallel flow occurs, as shown in Section 5.3.2). Therefore, predicting flow patterns and simulating the leakage phenomenon cannot be integrated with the same value of M . Section 7.3 will discuss a possible solution of this problem within the Phase Field method as further direction of this research.

6.4. CONCLUSIONS

When utilizing the parallel multiphase flow microfluidic solvent extraction for purification, without selectively modify the surface of the channel, leakage at the outlet of the microfluidic channel is a common occurrence, which results in failure of the microfluidic solvent extraction. This chapter investigates the leakage phenomenon in the microfluidic channel, focusing on the relationship between the leakage phenomenon with the volumetric flow rate ratio as well as the fluid-fluid-wall interaction.

In the experiments, adjusting the volumetric flow rate ratio (Φ_{aq}/Φ_{org}) of the fluids can change the leakage direction. However, it is found that leakage is unavoidable, even though the interface is located in the centre of the main channel. When the interface is located in the centre of the main channel, the fluid which preferably wets the microfluidic channel leaks to the other outlet.

In the Phase Field simulations, with the application of the equilibrium contact angle boundary condition, the leakage phenomenon occurs only for extremely low or large contact angles. Obviously, this finding does not agree with the experiments. The leakage phenomenon for common values of the equilibrium angles does not appear probably due to the fact that applying the equilibrium contact angle boundary condition is not adequate to capture the physics behind the leakage phenomenon by definition. With the non-equilibrium contact angle boundary condition, however, the organic slugs clogging the microfluidic channel is found in the simulations, which is unphysical as well. Further research reveals that decreasing the value of the mobility parameter (M) results in the occurrence of the leakage; however, since the mobility parameter (M) determines the flow patterns, it is not possible to use the same value of M to predict the occurrence of parallel flow and the leakage at the same time.

REFERENCES

- [1] Davide Ciceri, Jilska M. Perera, and Geoffrey W. Stevens. The use of microfluidic devices in solvent extraction. *Journal of Chemical Technology & Biotechnology*, 89(6):771–786, 2014.
- [2] N. Assmann, A. Ładosz, and P. Rudolf von Rohr. Continuous micro liquid-liquid extraction. *Chemical Engineering & Technology*, 36(6):921–936, 2013.
- [3] Petra Martini, Andrea Adamo, Neilesh Syna, Alessandra Boschi, Licia Uccelli, Nopphon Weeranoppanant, Jack Markham, and Giancarlo Pascali. Perspectives on the use of liquid extraction for radioisotope purification. *Molecules*, 24(2), 2019.
- [4] Tatsuo Maruyama, Hironari Matsushita, Jun-ichi Uchida, Fukiko Kubota, Noriho Kamiya, and Masahiro Goto. Liquid membrane operations in a microfluidic device for selective separation of metal ions. *Analytical Chemistry*, 76(15):4495–4500, 2004.
- [5] Robert J. Meagher, Yooli K. Light, and Anup K. Singh. Rapid, continuous purification of proteins in a microfluidic device using genetically-engineered partition tags. *Lab Chip*, 8:527–532, 2008.
- [6] Abraham Ulman. Formation and structure of self-assembled monolayers. *Chemical Reviews*, 96(4):1533–1554, 1996.
- [7] Nick R. Glass, Ricky Tjeung, Peggy Chan, Leslie Y. Yeo, and James R. Friend. Organosilane deposition for microfluidic applications. *Biomicrofluidics*, 5(3):036501, 2011.
- [8] Arata Aota, Akihide Hibara, Kyosuke Shinohara, Yasuhiko Sugii, Koji Okamoto, and Takehiko Kitamori. Flow velocity profile of micro counter-current flows. *Analytical Sciences*, 23(2):131–133, 2007.
- [9] Bin Zhao, Jeffrey S. Moore, and David J. Beebe. Surface-directed liquid flow inside microchannels. *Science*, 291(5506):1023–1026, 2001.
- [10] Akihide Hibara, Masaki Nonaka, Hideaki Hisamoto, Kenji Uchiyama, Yoshikuni Kikutani, Manabu Tokeshi, and Takehiko Kitamori. Stabilization of liquid interface and control of two-phase confluence and separation in glass microchips by utilizing octadecylsilane modification of microchannels. *Analytical Chemistry*, 74(7):1724–1728, 2002.
- [11] R. Wenmaekers. The use of microfluidics for the purification of medical radioisotopes. Master's thesis, Delft University of Technology, 2018.
- [12] Terence D. Blake. The physics of moving wetting lines. *Journal of Colloid and Interface Science*, 299(1):1 – 13, 2006.
- [13] Andrej Pohar, Mitja Lakner, and Igor Plazl. Parallel flow of immiscible liquids in a microreactor: modeling and experimental study. *Microfluidics and Nanofluidics*, 12(1):307–316, Jan 2012.

- [14] Henrik Bruus. *Theoretical microfluidics*. Oxford : Oxford Univ. Press, 2008., 2008.
- [15] Emilie Dressaire and Alban Sauret. Clogging of microfluidic systems. *Soft Matter*, 13:37–48, 2017.
- [16] Pengtao Yue, James J. Feng, Chun Liu, and Jie Shen. A diffuse-interface method for simulating two-phase flows of complex fluids. *Journal of Fluid Mechanics*, 515:293–317, 2004.

7

CONCLUSIONS AND RECOMMENDATIONS

When utilizing the parallel microfluidic liquid-liquid solvent extraction method to purify ^{99}Mo , two practical problems arise, *i.e.*, first, there are no clear criteria about how to establish a parallel flow pattern and second, leakage at the outlet of the microfluidic channel is difficult to avoid. Both of these problems lead to contamination of the extracted ^{99}Mo . This thesis deals with the complex multiphase flow phenomena inside a double Y-shaped microfluidic channel using the Phase Field method, focusing on predicting the occurrence of the parallel flow pattern and the leakage phenomenon. If the Phase Field method is able to simulate the above-mentioned problems, it can be used as a predictive tool to provide guidelines in designing the microfluidic chip.

The two above-mentioned problems are termed the *Interface Breakup Problem* and the *Moving Contact Line Problem*. This thesis firstly studies dry slug flow with the Phase Field method since both the *Interface Breakup Problem* and the *Moving Contact Line Problem* are involved in this type of flow. By monitoring the length, velocity and apparent contact angle of the slug, it is verified that these two problems are correctly modelled. Secondly, this research investigates the occurrence of parallel flow and the leakage phenomenon. The main results and conclusions of each chapter are provided in Section 7.1. Section 7.2 provides a brief practice guideline for choosing the numerical parameters and recommendations for future study are discussed in Section 7.3.

7.1. CONCLUSIONS

In Chapter 3, the *Interface Breakup Problem* has been investigated by studying the dry slug flow characteristics in the microfluidic channel. Besides this, the dry slug flow ($Ca < 1 \times 10^{-3}$ for both phases) ensures the existence of the *Moving Contact Line*, which is also one of the research topics of this thesis and has been studied in Chapter 4. Focusing on the *Interface Breakup Problem*, the simulation results vary with the choice of the capillary width (ϵ) and the mobility parameter (M). When the capillary width (ϵ) is changed, the mobility parameter (M) should be changed accordingly, to generate consistent simulation results. Until the start of this research, a consistent relationship between ϵ and M was not known in multiphase flows in microfluidics. This chapter aimed to reveal such a relationship between the capillary width (ϵ) and the mobility parameter (M). To this purpose, the slug length of dry slug flow of the n-heptane / water system in the double Y-shaped microfluidic channel has been studied. The main findings and conclusions of this chapter are:

1. The position of the initial interface plays a very important role in simulating dry slug flow in microfluidics with the Phase Field method. To produce a physically meaningful dry slug flow in agreement with the experiments, the initial interface should be prescribed at the Y-joint part of the microfluidic channel, to ensure the interfacial tension is expressed correctly, as described in Section 3.3.1.
2. The numerical parameters (ϵ and M) determine the slug length in dry slug flow. When the volumetric flow rates of the two phases are the same ($\Phi_{aq} = \Phi_{org}$), it is found that the slug length is linearly proportional to the Pe^{-1} number ($Pe =$

$\frac{2\sqrt{2}U_{aq}L\epsilon}{3M\sigma}$) and to the Cn number ($Cn = \frac{\epsilon}{L}$). To generate consistent slug length when the capillary width (ϵ) is varied, the mobility parameter (M) needs to be changed by following $CnPe^{-1} = \text{constant}$.

3. To ensure the Phase Field method can correctly capture the dynamics of the interface of the multiphase flow system, the slug length in the simulations is compared with that in the experiments at various volumetric flow rates. It is found that with one specific combination of the capillary width and the mobility parameter ($\epsilon = 6\mu\text{m}$ and $M = 3.60 \times 10^{-9}\text{m}^3\text{s/kg}$), the slug length in the simulations agree with that in the experiments.

In **Chapter 4**, the *Moving Contact Line* has been studied with the Phase Field method by investigating the apparent contact angles (θ_{app}) in dry slug flow. The Phase Field method uses a diffusive interface to enable the *Moving Contact Line* and the no-slip boundary condition at the solid walls of the microfluidic channel. However, it is found that the simulated leakage at the outlet of the microfluidic channel does not correspond to the experiments. This indicates that the physics of the *Moving Contact Line* is not modelled correctly. One of the reasons is that the equilibrium contact angle boundary condition does not sufficiently capture the flow phenomena at the outlet. It is therefore important to apply a boundary technique that can describe the apparent contact angles (θ_{app}) as a function of the interface velocity. For this purpose, the application of the non-equilibrium contact angle boundary condition first proposed by *Jacqmin* [1][2] is studied. It has been reported that this boundary condition provides more physical results in capturing the droplet spreading process [3] [4]. However, it is unclear if such a boundary condition is also applicable in multiphase flows in microfluidics. In dry slug flow of the n-heptane/water system in the microfluidic channel, the influence of the non-equilibrium contact angle boundary condition on the apparent contact angles (θ_{app}) and on the velocity of the n-heptane slugs is investigated. The main findings and conclusions of this chapter are:

1. With the equilibrium contact angle boundary condition ($\mu_f = 0\text{ Pa} \cdot \text{s}$), both the advancing contact angle (θ_A) and the receding contact angle (θ_R) of the slugs equal the prescribed equilibrium contact angle (θ_e), which indicates that the effect of the *Moving Contact Line* on the apparent contact angles (θ_{app}) is not shown. On the other hand, with the non-equilibrium contact angle boundary condition ($\mu_f > 0\text{ Pa} \cdot \text{s}$), the advancing contact angle (θ_A) is larger than the equilibrium contact angle (θ_e) and the receding contact angle (θ_R) is smaller than the equilibrium contact angle (θ_e), which agrees with the experimental observations.
2. The apparent contact angles (θ_{app}) of the slugs are determined by the Caf number ($Caf = \frac{\mu_f U_{org}}{\sigma}$) of the system. To produce the same apparent contact angle (θ_{app}), the three variables (U_{org} , σ and μ_f) can be varied as long as the Caf number is kept the same (keeping $\Phi_{aq} = \Phi_{org}$ in this process).
3. With the contact line friction parameter (μ_f) in the range between 1.0 and 2.0 $\text{Pa} \cdot \text{s}$, the apparent contact angles (θ_{app}) of the slugs in the simulations reasonably agree

with those in the experiments. In addition, the capillary width (ϵ) and the mobility parameter (M) do not bring significant influence on the apparent contact angles (θ_{app}).

4. When the equilibrium contact angle boundary condition being applied ($\mu_f = 0 \text{ Pa} \cdot \text{s}$), the velocity of the slugs does not show any dependency on the capillary width (ϵ) or the mobility parameter (M). Moreover, the velocity of the slugs in the simulations agree with that in the experiments. With the non-equilibrium contact angle boundary condition, however, the slug moves slower with the increase of the value of the capillary width (ϵ), the mobility parameter and the contact line friction parameter (μ_f).

In **Chapter 5**, the occurrence of parallel flow is studied with the Phase Field method and validated with experiments. Currently, there are no clear criteria for accurately predicting flow patterns in microfluidic channels. One of the reasons is that the understanding of the multiphase flow is incomplete and that there are lots of influencing factors to be taken into account. As mentioned in Section 1.4, the geometry and fabrication material of the microfluidic channel, physical properties of the working fluids as well as operating conditions determine flow patterns. Besides, predicting flow patterns with dimensional analysis in terms of fluid forces is not universally applicable [5]. This chapter aims to utilize the Phase Field method as a numerical tool to understand the occurrence of parallel flow. Chapter 3 has revealed that for the *Interface Breakup Problem*, the mobility parameter (M) and the capillary width (ϵ) influences simulation results. To ensure that flow patterns in the simulation agree with experiments, this study firstly focuses on choosing these two numerical parameters. Secondly, combining the Phase Field method with experiments based on the toluene/water system and the n-heptane/water system, this study reveals the dominating force that determines the flow patterns inside the microfluidic chip under investigation here. Thirdly, it has been reported that the contact angle plays an important role in determining the flow pattern, therefore this study also investigates the influence of the contact angle on the occurrence of the parallel flow. The main findings and conclusions of this chapter are:

1. In modelling the occurrence of the parallel flow, it finds that increasing the value of the mobility parameter (M) and the capillary width (ϵ) shift the critical Re number (the first time that the parallel flow occurs) to a higher value. However, the criterion ($CnPe^{-1} = \text{constant}$) found based on dry slug flow in Chapter 3 is not valid in modelling parallel flow. The Phase Field method can be utilized in this chapter for predicting flow patterns by finding the specific combination of the mobility parameter (M) and the Cn number, under which condition the simulation results agree with the experimental results.
2. Based on the experiments, when the interface is located in the centre of the microfluidic channel, the parallel flow pattern can be maintained when the Ca number of both phases is larger than 1×10^{-3} . By studying all three variables in the Ca number, the Phase Field simulations confirm that the Ca number that determines flow patterns in the studied microfluidic channel. Further research shows that the

We number plays a minor role in the occurrence of the parallel flow pattern in the studied microfluidic system.

3. Interaction between the fluids and the microfluidic channel wall influences the occurrence of parallel flow. Based on the experimental results and the Phase Field simulation of the toluene/water system and the tol+Aliquat/water system, the parallel flow pattern can occur at lower volumetric flow rates when one of the phases dominantly wets the wall surface (*i.e.*, θ_e is close to 0° or 180°).

In **Chapter 6**, leakage at the outlet of the microfluidic channel is investigated with experiments and the Phase Field method, aiming to provide guidelines for achieving complete phase separation. The leakage phenomenon at the outlet of the double Y-shaped microfluidic channel is a common occurrence in the parallel multiphase flow pattern, which will result in failure of the microfluidic solvent extraction. This chapter experimentally investigates the leakage phenomenon in the microfluidic channel, focusing on the relationship between the leakage phenomenon and the volumetric flow rate ratio as well as the fluid-fluid-wall interaction. Besides, this research studies the effect of the contact angle boundary condition on the leakage phenomenon using simulations and experiments. The main findings and conclusions of this chapter are:

1. In the experiments when parallel flow is established, the volumetric flow rate ratio (Φ_{aq}/Φ_{org}) of the fluids influences the position of the interface inside the microfluidic channel. This can even change the leakage direction. Unfortunately, leakage is unavoidable, even though the interface is located in the centre of the main channel. Under such circumstances, the fluid which preferably wets the microfluidic channel leaks to the other outlet.
2. Applying the equilibrium contact angle boundary condition in the Phase Field simulations, the leakage phenomenon occurs only when one of the phases dominantly wets the microfluidic channel (θ_e is close to 0° or 180°). Under such a situation, leakage in the simulation does not agree with that in experiments. With the non-equilibrium contact angle boundary condition, the organic slugs clogging the microfluidic channel is found in the simulations, which is considered as unphysical.
3. Further research reveals that decreasing the value of the mobility parameter (M) results in the occurrence of leakage; however, since the mobility parameter (M) determines flow patterns, it is not possible to use the same value of M to predict the occurrence of parallel flow and leakage at the same time.

7.2. PRACTICE GUIDELINES

This work mainly focuses on simulating multiphase flows inside a microfluidic channel with the Phase Field method. The following paragraph provides a brief and practical guideline for choosing the numerical parameters and flow conditions.

- 7
1. The capillary width (ϵ), (or the Cn number in dimensionless form), controls the thickness of the diffusive interface of the Phase Field method. The interfacial thickness in the simulation is usually much larger than that of a physical interface (a few nanometers [6]), since there should be enough node points within the diffusive interface to ensure convergent simulation results. If the Cn number is chosen too small, the computational effort is unaffordable. On the other hand, if the Cn number is chosen too large, it will lose details of the interface [7]. The choice of the Cn number influences simulation results related to the *Interface Breakup Problem*. In this study, as an example, the Cn number in the range of 0.03 to 0.1 has been investigated. One can decide the Cn number based on the computing resource, to keep the calculation time acceptable.
 2. The mobility parameter (M) is not an experimentally measurable physical parameter and is not known as a priori for a given system. The value of the mobility parameter (M) determines if the numerical calculation converges or not [1] [2]. For instance, in modelling dry slug flow in Chapter 3 when $Cn = 0.06$, the mobility parameter (M) should be in the range from $1.60 \times 10^{-14} \text{ m}^3\text{s/kg}$ to $1.60 \times 10^{-3} \text{ m}^3\text{s/kg}$, to ensure convergence of the simulation.
 3. Similar to the capillary width (ϵ), the choice of the mobility parameter (M) also affects simulation results. As a result, the mobility parameter (M) is usually determined by combining experiments with numerical simulations. As a typical example, it finds that with $Cn = 0.06$ and $M = 3.60 \times 10^{-9} \text{ m}^3\text{s/kg}$, the slug length in simulations fit the experimental results. When the Cn number is changed, the mobility parameter (M) needs to be varied accordingly, to generate consistent simulation results. However, the relationship between the Cn number and the mobility parameter (M) does not universally hold in different flow types and finding their relationship is still a challenge [2][8] [9][10]. Thus, when the Cn number is changed, one can find the new mobility parameter (M) by fitting simulations to experiments again or try to find the specific scaling law of the Cn number and the mobility parameter (M) for the studied flow type.
 4. With the non-equilibrium contact angle boundary condition ($\mu_f > 0 \text{ Pa} \cdot \text{s}$), when μ_f is in the range between 1.0 and $2.0 \text{ Pa} \cdot \text{s}$, the simulated apparent contact angle (θ_{app}) of the slugs agree with the experiments. However, using the non-equilibrium contact angle boundary condition, there is no improvement in simulating the leakage, compared with the equilibrium contact angle boundary condition.
 5. The position of the initial interface plays a very important role in the simulations with the Phase Field method. For example, in modelling slug flow in Section 3.3.1, when the initial interface is prescribed in the middle of the microfluidic channel, the flow pattern always becomes parallel flow. To produce a physically meaningful slug flow, the initial interface should be prescribed at the Y-joint part of the microfluidic channel, to ensure the interfacial tension is correctly calculated.

7.3. RECOMMENDATIONS

In the Phase Field method, the wall boundary condition is found to play a significant role in modelling multiphase flow phenomena [11]. Chapter 6 reveals that it is not possible to use the same value of M to predict the occurrence of parallel flow and the leakage at the same time. Thus, future study can investigate if other wall boundary conditions for the *Moving Contact Line* can model the leakage at the outlet of the microfluidic channel. For instance, *Qian et al.* have proposed a generalized Navier boundary condition to replace the no-slip boundary condition in the Phase Field model [12][13][14][15]. By introducing one more numerical parameter, this boundary condition includes slip at the wall. Thus, it will be interesting to study if the occurrence of parallel flow and the leakage can be simulated at the same time with such a boundary condition.

Future research could investigate the feasibility of utilizing an aqueous-aqueous two-phase system to purify ^{99}Mo . Such a system can be formed by dissolving certain polymers into the aqueous solution and this microfluidic system has already been reported to separate proteins, antibodies, DNA and cells [16]. Based on the study of Chapter 5, interfacial tension between the aqueous phase and the organic phase tends to destabilize the interface in the parallel microfluidic multiphase flow. Compared with the aqueous-organic system, the interfacial tension of the aqueous-aqueous two-phase system is much lower (1×10^{-4} to 1×10^{-1} mN/m) [16]. Therefore it is expected that parallel flow can be established in the aqueous-aqueous system at lower flow rates, which could increase the contact time of the two phases and the extraction efficiency. Furthermore, based on the results of Chapter 6, leakage is more likely to occur when one phase is dominantly wetting the microfluidic channel. The similar properties of the two aqueous phases would result in a similar affinity with the solid microfluidic channel [17], which may reduce leakage. Since the formation of the aqueous-aqueous two-phase system requires adding polymers into the aqueous solution, future research should investigate whether these polymers are durable under irradiation.

For avoiding leakage and achieving complete phase separation, future research could focus on using different materials to fabricate the outlets of the microfluidic channel, to make one hydrophobic and the other one hydrophilic. Furthermore, the geometry of the outlets can also be changed, to help improve the phase separation performance. To implement this technique, the difficulty comes from finding suitable materials which are compatible with the utilized organic solvent solution and with irradiation from radioactive nuclides. In addition, considering the small dimension of the microfluidic channel, connecting these two materials might also be a challenge. If the desired materials are found, then the flow pattern does not need to be limited to parallel flow. In this case, segmented flow can be utilized as well and the mass transfer performance in segmented flow is reported to be better than that in parallel flow [18].

REFERENCES

- [1] David Jacqmin. Calculation of two-phase Navier–Stokes flows using phase-field modeling. *Journal of Computational Physics*, 155(1):96 – 127, 1999.
- [2] David Jacqmin. Contact-line dynamics of a diffuse fluid interface. *J. Fluid Mech*, 402:57–88, 2000.
- [3] A. Carlson, M. Do-quang, and G. Amberg. Dissipation in rapid dynamic wetting. *Journal of Fluid Mechanics*, 682:213–240, 2011.
- [4] A. Carlson, G. Bellani, and G. Amberg. Contact line dissipation in short-time dynamic wetting. *Europhysics Letters*, 97(4):44004, feb 2012.
- [5] Jinyuan Qian, Xiaojuan Li, Zan Wu, Zhijiang Jin, and Bengt Sunden. A comprehensive review on liquid–liquid two-phase flow in microchannel: flow pattern and mass transfer. *Microfluidics and Nanofluidics*, 23:116, 2019.
- [6] Chun Yang and Dongqing Li. A method of determining the thickness of liquid–liquid interfaces. *Colloids and Surfaces A: Physicochemical and Engineering Aspects*, 113(1):51 – 59, 1996.
- [7] R. S. Qin and H. K. Bhadeshia. Phase field method. *Materials Science and Technology*, 26(7):803–811, 2010.
- [8] V.V. Khatavkar, P.D. Anderson, and H.E.H. Meijer. On scaling of diffuse-interface models. *Chemical Engineering Science*, 61(8):2364 – 2378, 2006.
- [9] F. Magaletti, F. Picano, M. Chinappi, L. Marino, and C. M. Casciola. The sharp-interface limit of the Cahn–Hilliard/Navier–Stokes model for binary fluids. *Journal of Fluid Mechanics*, 714:95–126, 2013.
- [10] Pengtao Yue, Chunfeng Zhou, and James J. Feng. Sharp-interface limit of the Cahn–Hilliard model for moving contact lines. *Journal of Fluid Mechanics*, 645:279–294, 2010.
- [11] Marwah Azzawi, Farouq S. Mjalli, Afzal Husain, and Muthanna Dahhan. A review on the hydrodynamics of the liquid liquid two phase flow in the microchannels. *Industrial Engineering Chemistry Research*, 60(14):5049–5075, 2021.
- [12] Tiezheng Qian, Xiao-Ping Wang, and Ping Sheng. Molecular scale contact line hydrodynamics of immiscible flows. *Phys. Rev. E*, 68:016306, Jul 2003.
- [13] Tiezheng Qian, Xiao-Ping Wang, and Ping Sheng. Power-law slip profile of the moving contact line in two-phase immiscible flows. *Phys. Rev. Lett.*, 93:094501, Aug 2004.
- [14] Tiezheng Qian, Xiao-Ping Wang, and Ping Sheng. Hydrodynamic slip boundary condition at chemically patterned surfaces: A continuum deduction from molecular dynamics. *Phys. Rev. E*, 72:022501, Aug 2005.

- [15] Tiezheng Qian, Xiaoping Wang, and Ping Sheng. A variational approach to moving contact line hydrodynamics. *Journal of Fluid Mechanics*, 564:333–360, 2006.
- [16] Steffen Hardt and Thomas Hahn. Microfluidics with aqueous two-phase systems. *Lab Chip*, 12:434–442, 2012.
- [17] Yun Suk Huh, Sang Jun Jeon, Eun Zoo Lee, Ho Seok Park, and Won Hi Hong. Microfluidic extraction using two phase laminar flow for chemical and biological applications. *Korean Journal of Chemical Engineering*, 28(3):633–642, Mar 2011.
- [18] N. Assmann, A. Ładosz, and P. Rudolf von Rohr. Continuous micro liquid-liquid extraction. *Chemical Engineering & Technology*, 36(6):921–936, 2013.

ACKNOWLEDGEMENTS

First of all, I would love to express my greatest appreciation to my promtors Dr. Martin Rohde and Prof. Jan-Leen Kloosterman for giving me the opportunity to pursue a Ph.D. at TUDelft. I highly appreciate the insightful guidance, fruitful discussion and constant encouragement throughout all my Ph.D. study. Besides, I would like to express sincere gratitude to Dr. Elisabeth Oehlke who has given me a lot of valuable scientific suggestions in the field of microfluidics. Many thanks also go to Dr. Ilza Dalmázio who has shared her knowledge and experience in conducting experiments. In addition, I would like to thank all my colleagues from the RPNM and ARI departments, who make the Ph.D. experience interesting and great.

I would like to express my gratitude to my friends in Delft and Eindhoven. I am very grateful to my parents who are always there to support and encourage me. Especially, I would like to thank my girlfriend Cui Ping for her companionship and patience during this intensive and challenging period.

CURRICULUM VITÆ

Zheng LIU

27-10-1989 Born in Yanji, Jilin Province, China.

EDUCATION

- 2008–2012 B.Sc. in Physics
Northeast Normal University
Changchun, China
- 2012-2015 M.Sc. in Particle Physics and Nuclear Physics
Northeast Normal University
Changchun, China
- 2015-2022 Ph.D. in Applied Physics
Delft University of Technology
Thesis: Purifying Radionuclides with Microfluidic
Technology for Medical Purpose
Promotor: Dr. ir. M. Rohde
Prof. dr. ir. J. L. Kloosterman

LIST OF PUBLICATIONS

1. **Liu, Z.**, K. S. Schaap, L. Ballemans, R. de Zanger, E. de Blois, M. Rohde and E. Oehlke, *Measurement of reaction kinetics of [177Lu]Lu-DOTA-TATE using a microfluidic system*, Dalton Transactions 46(42): 14669-14676 (2017).
2. **Liu, Z.**, G. Li and L. Liu, *Feasibility of sealed D-T neutron generator as neutron source for liver BNCT and its beam shaping assembly*, Applied Radiation and Isotopes 86: 1-6 (2014).
3. **Liu, Z.**, J.L. Kloosterman and M. Rohde, *Development and validation of a Phase Field model for dry slug flow inside a microfluidic channel, Part I: Slug length*, (in preparation).
4. **Liu, Z.**, J.L. Kloosterman and M. Rohde, *Development and validation of a Phase Field model for dry slug flow inside a microfluidic channel, Part II: Apparent contact angle*, (in preparation).
5. **Liu, Z.**, J.L. Kloosterman and M. Rohde, *Investigating flow patterns and leakage phenomenon inside a double Y-shaped microfluidic channel with Phase Field method*, (in preparation).